



**FACULTY OF PHYSICS  
AND APPLIED INFORMATICS**  
University of Lodz

University of Lodz  
Faculty of Physics and Applied Informatics  
Department of Astrophysics

# **Modelling of the non-thermal emission from inhomogeneous jets in active galactic nuclei**

**Piotr Banasiński**

Doctoral thesis performed  
in Department of Astrophysics  
under the supervision of  
prof. dr hab. Włodzimierz Bednarek  
and the auxiliary supervision of  
dr hab. Julian Sitarek

Łódź, 2018





**WYDZIAŁ FIZYKI  
i INFORMATYKI STOSOWANEJ**  
Uniwersytet Łódzki

Uniwersytet Łódzki  
Wydział Fizyki i Informatyki Stosowanej  
Katedra Astrofizyki

**Modelowanie promieniowania nietermicznego  
z niejednorodnych strug  
w aktywnych jądrach galaktyk**

**Piotr Banasiński**

Praca doktorska wykonana  
w Katedrze Astrofizyki  
pod kierunkiem promotora  
prof. dr hab. Włodzimierza Bednarka  
i promotora pomocniczego  
dr hab. Juliana Sitarka

Łódź, 2018



# Contents

<b>Abstract</b>	<b>1</b>
<b>Streszczenie</b>	<b>3</b>
<b>1 Active Galactic Nuclei</b>	<b>5</b>
1.1 Main facts from AGNs history . . . . .	9
1.2 Central engine and unification view of AGNs . . . . .	10
1.3 Jets from AGNs . . . . .	13
1.4 Emission from the AGN jets . . . . .	15
1.4.1 $\gamma$ -rays from jets in AGNs . . . . .	16
1.5 Motivation for modeling the non-thermal emission from AGN jets . . . . .	19
<b>2 Parsec-Scale Jets in AGNs</b>	<b>21</b>
2.1 Motion of plasma in relativistic jets . . . . .	21
2.2 Geometry of the parsec-scale jet . . . . .	24
2.3 Transfer of radiation in jets . . . . .	25
2.4 Radiation processes in leptonic jets . . . . .	26
2.4.1 Synchrotron radiation . . . . .	26
2.4.2 Compton scattering . . . . .	28
2.4.3 The $\gamma$ -ray absorption in $e^\pm$ pair production process . . . . .	31
2.5 Acceleration of particles in AGN jets . . . . .	33
2.5.1 Stochastic acceleration . . . . .	33
2.5.2 Diffusive shock acceleration . . . . .	34
2.5.3 Magnetic reconnection . . . . .	35
<b>3 Modeling of the Non-Thermal Emission from AGN Jets</b>	<b>37</b>
3.1 Estimation of the basic parameters of AGN jets . . . . .	37
3.2 Estimation of parameters from spectral properties of blazar jets . . . . .	39
3.3 Leptonic models of emission from AGN jets . . . . .	40
3.3.1 One-zone, homogeneous SSC models of AGN jets . . . . .	41
3.3.2 External Compton models of AGN jets . . . . .	42
3.3.3 Interaction of AGN jets with compact objects . . . . .	43
3.3.4 Multi-component models of AGN jets . . . . .	43

3.3.5	Inhomogeneous models of AGN jets . . . . .	44
3.4	Hadron models of AGN jets . . . . .	45
<b>4</b>	<b>The Stationary Non-Local Inhomogeneous Jet Model</b>	<b>47</b>
4.1	Theoretical description of the model . . . . .	48
4.2	The steady spectrum of electrons and local density of photons in the non-local jet model . . . . .	52
4.3	Spectra produced for different parameters of the jet . . . . .	56
4.3.1	The example of spectral energy distribution . . . . .	56
4.3.2	Geometry of the jet . . . . .	58
4.3.3	Magnetic field . . . . .	59
4.3.4	Electron acceleration . . . . .	61
4.3.5	Observation angle . . . . .	64
4.4	Application of non-local inhomogeneous jet model to Mrk 421 . . . . .	65
<b>5</b>	<b>Stationary Stratified Jet Model</b>	<b>69</b>
5.1	Theoretical description . . . . .	71
5.2	The equilibrium spectrum of electrons and local density of photons in stratified jet . . . . .	75
5.3	Spectra from the whole jet obtained in the spine-sheath model . . . . .	79
5.3.1	The example of spectral energy distribution obtained with the model . . . . .	79
5.3.2	Observation angle . . . . .	81
5.4	Interpretation of the blazar sequence for HBLs and FRI radio galaxies in spine-sheath model . . . . .	82
<b>6</b>	<b>Electromagnetic Cascades in Extended Inhomogeneous Jet</b>	<b>85</b>
6.1	Numerical implementation . . . . .	89
6.2	Intrinsic $\gamma$ -ray opacity for different parameters of the jet . . . . .	90
6.3	Spectra from the cascades for different parameters of the primary VHE photons . . . . .	92
6.3.1	Injection of the monoenergetic VHE $\gamma$ -rays . . . . .	92
6.3.2	Injection of VHE $\gamma$ -rays with the power-law distribution . . . . .	94
6.4	Application of the $e^\pm$ cascade-inside-jet model to blazars . . . . .	95
<b>7</b>	<b>Summary and Conclusions</b>	<b>99</b>

# Abstract

Some active galactic nuclei (AGNs) are strong sources of non-thermal radiation. It is expected that this radiation is produced in collimated outflows of plasma moving with relativistic speeds, the so-called jets. The non-thermal radiation from AGN jets extends over the entire electromagnetic spectrum, i.e. from the radio band to the very high energy  $\gamma$ -rays. This radiation is strongly variable in every energy range. The reproduction of these properties of radiation with theoretical models allows us to understand processes and conditions occurring in AGN jets.

The AGN jets have been the subject of extensive research for several decades. However, some fundamental questions still remain unanswered. The study of the AGN jets can give the answers to such basic questions as: How are the non-thermal particles accelerated inside the AGN jets? Where are the high energy  $\gamma$ -rays produced? What is the type of particles responsible for the non-thermal radiation?

Most commonly, the non-thermal radiation from AGN jets is modeled with one-zone homogeneous lepton model. In such a model, the emission region is approximated by a spherical blob. This blob moves along the jet with relativistic speed. Such model assumes that the conditions inside the blob are constant and homogeneous. The evident advantage of this model is the fact that it is determined by only a few free parameters. However, the observed spectral details and the complex temporal behaviors require more sophisticated models.

For example, the one-zone synchrotron self-Compton model is not able to explain the persistent emission from AGN jets. Some AGNs are observed in a low activity state lasting for months. This persistent emission is observed also in the very high energy  $\gamma$ -ray range. In such a long period of time, the parameters in the moving emission region should change significantly. In this context, I propose the stationary and inhomogeneous jet model. The parameters in the model change with the distance from the jet base. In contrast to the one-zone model, I approximate the emission region with a parsec-scale cone which better describes the shape of AGN jets measured with the radio telescopes. Due to the elongated shape of the jet, I take into account the non-locally produced photons when calculating the inverse Compton process. The equilibrium state of particles in the jet is obtained by the dedicated generation method. My approach provides a unique tool for modeling of the jets in the persistent, low-activity emission state.

The results of the commonly used emission models of AGN jets are inconsistent with the unification model of AGNs. The unification model assumes that the radio galaxies are counterparts of blazars observed at large angles. Whereas, the modeling of radio galaxies requires different parameters than the modeling of blazar type of AGNs. I show that the spectra of both, radio galaxies and blazars, considered in this thesis can be obtained in terms of the unified model. For this purpose, I develop the two-component jet model, in which fast-moving plasma, close to the jet axis, is surrounded by slower plasma. In contrast to previous models of this type, I take into account the strong interrelation between different jet components in the calculations of the equilibrium spectrum of relativistic electrons.

In the third model, I investigate the consequences of the production of  $\gamma$ -rays in the vicinity of a super-massive black hole in blazars. Some models, supported by the observations of the extremely fast flares, assume that the very high  $\gamma$ -rays are produced relatively close to the black hole. In the case of blazars, the jet propagates towards the observer. Hence, these  $\gamma$ -rays have to pass the jet radiation field before they escape to the observer. These  $\gamma$ -rays can be strongly absorbed initiating the inverse Compton  $e^\pm$  pair cascades. I explore this idea in terms of the observed excess in the hard X-rays in nearby blazar Mrk 421.

# Streszczenie

Część aktywnych galaktyk we Wszechświecie jest silnymi źródłami promieniowania nietermicznego. Promieniowanie to jest produkowane w skolimowanych strugach plazmy poruszających się z relatywistycznymi prędkościami (ang. *jets*). Promieniowanie nietermiczne pochodzące z relatywistycznych strug w aktywnych galaktykach rozciąga się od zakresu radiowego aż do najwyższych obserwowanych energii promieniowania gamma. W każdym z tych zakresów, promieniowanie to jest silnie zmienne. Próba odtworzenia właściwości tego promieniowania, przy użyciu modeli teoretycznych, pozwala zrozumieć zarówno procesy jakie zachodzą w relatywistycznych strugach, jak i warunki w nich panujące.

Już od dziesiątek lat, relatywistyczne strugi w aktywnych galaktykach są przedmiotem intensywnych badań. Pomimo to, niektóre fundamentalne pytania wciąż pozostają bez odpowiedzi. Dalsze badania nad relatywistycznymi strugami mogą dać odpowiedzi na takie pytania jak: w jaki sposób są przyspieszane cząstki nietermiczne wewnątrz strug? gdzie dochodzi do produkcji wysokoenergetycznego promieniowania gamma? jakie cząstki są odpowiedzialne za powstawanie promieniowania nietermicznego?

Najczęściej promieniowanie nietermiczne jest modelowane przez jednorodne modele leptonowe, ograniczające się do jednego miejsca emisji. Ten typ modeli zakłada, że promieniowanie jest produkowane w sferycznym obszarze, który porusza się wzdłuż strugi z relatywistyczną prędkością. Zazwyczaj przyjmuje się, że warunki panujące w miejscu emisji są jednorodne i stałe w czasie. Te uproszczenia powodują, że model jest zależny tylko od kilku parametrów, co jest niewątpliwą zaletą tego typu modeli. Jednakże, dokładne wymodelowanie obserwowanych widm pochodzących z relatywistycznych strug i oddanie ich zmian zachodzących z czasem wymaga użycia bardziej skomplikowanych modeli.

Przykładem może być problem jaki opisane wyżej modele mają z wytłumaczeniem niezmienną emisji pochodzącej z relatywistycznych strug w aktywnych galaktykach. Niektóre aktywne galaktyki są obserwowane w stanie niskiej aktywności, który trwa miesiącami. Co więcej, ta niezmienna emisja jest obserwowana również w najwyższych energiach. W tak długim okresie czasu, parametry opisujące obszar emisji powinny się znacząco zmienić. W związku z tymi obserwacjami, proponuję inny model emisji z relatywistycznych strug, w którym warunki w strudze zmieniają się wraz z odległością od podstawy strugi, lecz nie zmieniają się z czasem. W przeciwieństwie do prostych

jednorodnych modeli wspomnianych wyżej, przedstawiony w pracy model zakłada, że obszar emisji ma kształt stożka o długości rzędu parseków. Takie założenie lepiej zgadza się z obserwacjami dokonanymi w zakresie radiowym. Ze względu na wydłużony kształt obszaru emisji, w trakcie uwzględniania odwrotnego efektu Comptona konieczne było wzięcie pod uwagę promieniowania produkowanego w odległych miejscach strugi. Stan równowagi w relatywistycznej strudze jest otrzymywany poprzez zastosowanie metody iteracyjnej. Czyni to opracowany przeze mnie model unikalnym narzędziem do modelowania relatywistycznych strug w trakcie ich niezmiennej emisji.

Używane powszechnie modele relatywistycznych strug w aktywnych galaktykach dają wyniki trudne do pogodzenia z modelem unifikacyjnym aktywnych galaktyk. Model ten zakłada, między innymi, że galaktyki radiowe są blazarami obserwowanymi pod dużym kątem do osi strugi. Jednakże, modele galaktyk radiowych wskazują na zupełnie inne parametry niż modele blazarów. W tej pracy pokazuję, że w ramach jednego modelu można uzyskać widma obu tych typów aktywnych galaktyk. W tym celu opracowałem dwuskładnikowy model relatywistycznej strugi, w którym plazma szybko poruszająca się blisko osi strugi jest otoczona przez plazmę poruszającą się znacznie wolniej. W przeciwieństwie do poprzednich modeli tego typu, w trakcie obliczeń widma elektronów biorę pod uwagę silną współzależność pomiędzy tymi dwoma składnikami strugi.

W trzecim z przedstawionych modeli badam konsekwencje produkcji promieniowania gamma w bliskim otoczeniu czarnej dziury wewnątrz blazarów. Niektóre modele, inspirowane niezwykle szybkimi flarami obserwowanymi w aktywnych galaktykach, zakładają, że wysokoenergetyczne promieniowanie gamma jest produkowane relatywnie blisko czarnej dziury. W przypadku blazarów, obserwator jest położony wzdłuż kierunku wyznaczonego przez relatywistyczną strugę. W takim przypadku, wysokoenergetyczne promieniowanie gamma, zanim dotrze do obserwatora, propaguje się w polu promieniowania strugi. Wtedy promieniowanie gamma może być absorbowane inicjując kaskady elektromagnetyczne. W tej pracy analizuję taki scenariusz w kontekście nadwyżki wysokoenergetycznego promieniowania X obserwowanego z pobliskiego obiektu Mrk 421.

# Chapter 1

## Active Galactic Nuclei

Galaxies are cosmic structures consisting of gravitationally bound stars, interstellar dust, gas and dark matter. Radiation observed in galaxies is composed of radiation produced by the specific components: stars, gas, and dust forming the galaxy. The spectra emitted by stars and dust, in the first approximation, can be described with the black body radiation. The black body radiation is emitted by matter with temperature  $T$  which is in thermodynamic equilibrium (Rybicki and Lightman, 1986).

The nature of radiation from a typical galaxy is thermal. The black body radiation is emitted in a narrow energy range around the value equal to  $\epsilon_{max} = 2.82 kT$  (Ghisellini, 2013), where  $k$  is the Boltzmann constant. The temperature of stars encountered in the Universe lays in the range from  $\sim 3000$  K to  $\sim 50000$  K (Longair, 2011). Then, the radiation from the stars in a typical galaxy form a relatively narrow component from the infrared (IR) to the ultraviolet (UV). The exact shape of this component depends on the dominating type of stars in a galaxy. The dust in galaxies absorbs and re-emits the radiation from stars. It is responsible for the second component in the spectrum of a galaxy placed at the mid- and the far-infrared. Therefore, spectra from galaxies are dominated by radiation in the range from IR to UV.

Less common objects, such as compact binary systems, pulsars, pulsar wind nebulae, supernovae and supernova remnants, can be found in galaxies. Such objects produce the non-thermal radiation in the whole range of the electromagnetic spectrum, i.e. from radio (Condon, 1992), through X-rays (Fabbiano, 1989) to  $\gamma$ -rays. However, this radiation is negligible in comparison to the thermal radiation emitted by a typical galaxy.

A galaxy, as a whole system, evolves relatively slow. Because of that, the radiation from a typical galaxy changes only over the cosmological timescales. When we exclude the transient events, like supernovae explosions and gamma-ray bursts, we can assume that the radiation from galaxies is approximately constant in time.

Several percents of galaxies, observed in the Universe, does not match the description of a normal galaxy. In contrast to common galaxies, they are characterized by a few extraordinary properties. The bolometric luminosities of these galaxies change in very

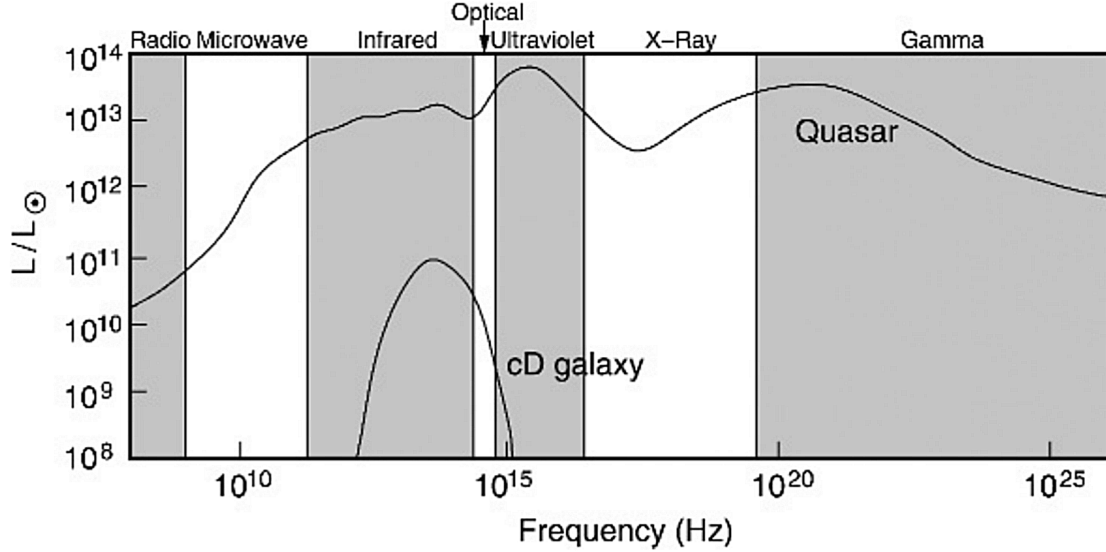


Figure 1.1: The spectral energy distributions of a normal (elliptical) galaxy and a quasar (3C273). (From Schneider, 2006).

short periods and their radiation is emitted in the whole electromagnetic spectrum, i.e. from radio to  $\gamma$ -rays. Moreover, the exceptionally strong emission lines occur in the optical part of the electromagnetic spectrum. What is more, most of the radiation is produced in the central part of the galaxy. Due to these exceptional properties, these objects have been named *active galactic nuclei* (AGNs).

The spectra of the majority of AGNs show the broad emission lines in the optical and the UV ranges emitted by highly ionized atoms. Assuming that emission lines are emitted by the clouds of gas moving with different velocities with respect to an observer, the broadening of emission lines is a natural consequence of the Doppler effect. An emission line emitted by a cloud moving towards the observer is shifted to higher energy (smaller wavelength) and an emission line from a cloud moving away from the observer is detected as redshifted (shifted to smaller energy). The total emission from many clouds with random velocities is observed as broad emission line. In terms of the Doppler effect, the full width at half maximum (FWHM) of an emission line can be expressed in km/s. The lines observed in AGNs are characterized by  $\text{FWHM} \sim 1000$  km/s. It indicates that the plasma moving with large velocities has to exist in AGNs. The lines in AGNs are divided into two groups: the broad emission lines, with  $\text{FWHM} \approx 10^3 - 1.5 \times 10^4$  km/s and the narrow emission lines, with  $\text{FWHM} \approx 200 - 2000$  km/s (Sulentic et al., 2000).

AGNs are strongly variable on every time scales – from years to minutes (Ulrich et al., 1997). The luminosity of AGNs can change by a factor of two during the period shorter than one day (Wagner and Witzel, 1995). It indicates that the radiation should be produced in an extremely small region, with the radius  $R < 10^{16}$  cm. Furthermore,

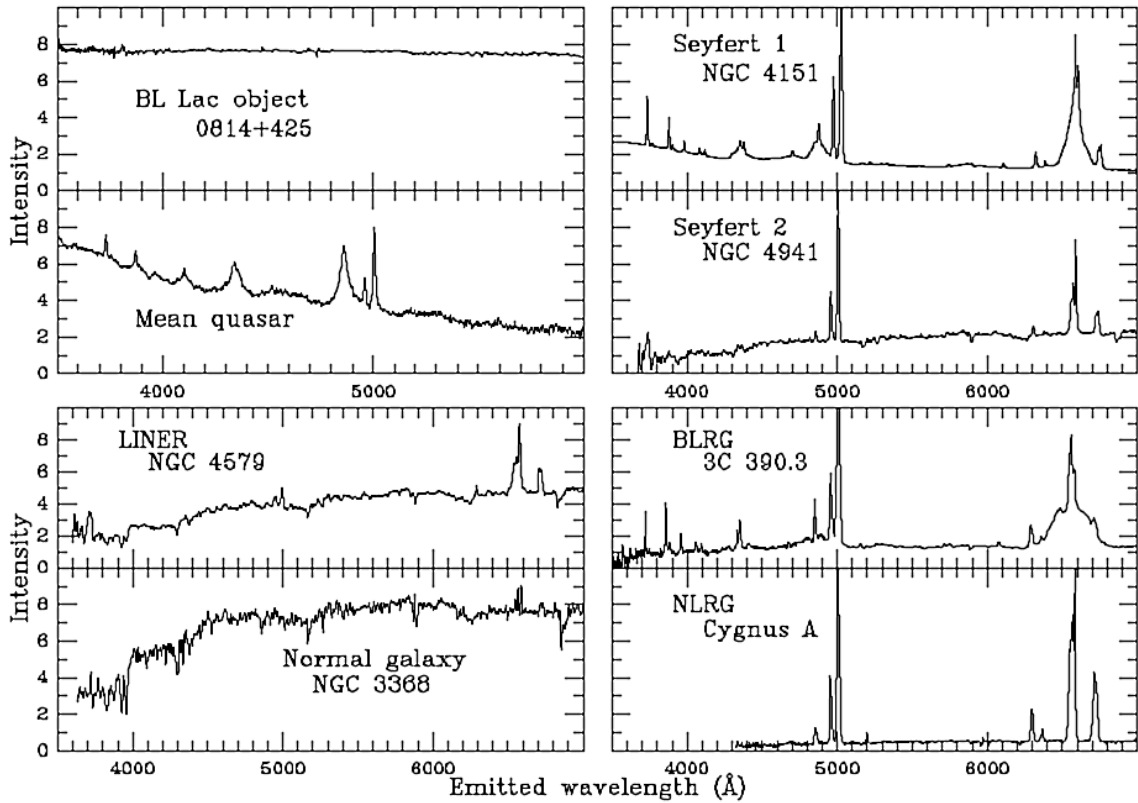


Figure 1.2: The optical spectra of different galaxies. (Figure from: [astronomy.ua.edu/keel/](http://astronomy.ua.edu/keel/). Data for NGC 4579 and 4941 comes from Keel (1983), for Cygnus A from Owen et al. (1990), for 0814+425 and 3C390.3 from Lawrence et al. (1996), for 'Mean quasar' from Francis et al. (1991), for NGC 3368 Kennicutt (1992)).

the variability is unpredictable. The sources are variable in every energy range. Generally, the variability time scales are shorter in higher energy range. In the case of the most variable AGNs, called blazars, the variability time-scales in X-rays and  $\gamma$ -rays can be shorter than one hour.

All AGNs are strong emitters of X-rays. However, only some of them emit strongly in the radio and the  $\gamma$ -ray ranges producing non-thermal continuum radiation. Based on the ratio between the radio and the optical flux, AGNs are divided into two types: the radio-loud and the radio-quiet AGNs (Kellermann et al., 1989). In many cases, the radiation is highly polarized. The bolometric luminosity of AGNs can be thousand times higher than the bolometric luminosity of the stars and dust in the host galaxy. It is clearly visible in Fig. 1.1, where the luminosity of the normal galaxy is compared with the luminosity of the AGN.

Nevertheless, not all AGNs are characterized by every listed above features. Because of the observed properties of AGNs, the active galaxies are divided into a few, more or less precise, types (Tadhunter, 2008).

- Seyfert galaxies – They are the spiral galaxies with relatively low luminosities.

They are typically weak sources in radio range. Only some of them are detected in  $\gamma$ -rays. They are divided into two groups, the Seyfert galaxies of Type 1 and Type 2. In the spectra of the first group, both, the broad and the narrow emission lines are observed. In case of Type 2, only the narrow lines are observed (compare Seyfert 1 and Seyfert 2 spectra in Fig. 1.2).

- Radio galaxies – They are giant elliptical galaxies and also very strong radio emitters. This type of AGNs is divided into two classes – Fanaroff-Riley Type I (FR I) and Fanaroff-Riley Type II (FR II) (Fanaroff and Riley, 1974). In the first class, radio maps show the single, bright radio source located at the center of galaxies. The radio maps of FR II objects shows two bright spots, called lobes, located almost symmetrically around the less bright (in radio range) center of a galaxy. Due to the appearance of the broad and narrow emission lines, radio galaxies are divided into the broad-lines radio galaxies (BLRG) and narrow-lines radio galaxies (NLRG; compare: BLRG and NLRG in Fig. 1.2).
- Quasars – The name of this type of AGNs comes from the name "quasi-stellar objects" since these objects are observed as point sources by optical telescopes. They are extremely luminous AGNs. In the spectra, broad and narrow emission lines are observed (see: spectrum of "Mean quasar" in Fig. 1.2). Quasars are usually radio quiet objects. However, some of them are strong radio emitters. The radio loudness of quasars is associated with detectable  $\gamma$ -ray emission.
- BL Lac objects – The name of this type of AGNs comes from the BL Lac galaxy - the prototype of this type. BL Lac objects are radio loud. Their spectra do not show the emission lines (see: "BL Lac object" in Fig. 1.2). Because of that, it is difficult to determine their distance. BL Lacs are strong  $\gamma$ -ray emitters, up to the multi-TeV energies. They are extremely variable, even on a time scale of several minutes.
- LINERs – Low-ionization nuclear emission-line regions. This type of AGN is characterized by emission lines of low ionized atoms. LINERs form a group of low luminous AGNs.

Today, the above division has mainly a historical importance. With the development of observational techniques and the growing number of discovered sources, the intermediate types of AGNs have been discovered. Currently, we are confident that a large number of the AGN types is a result of the orientation effects and the presence of a radio jet.

## 1.1 Main facts from AGNs history

The history of AGNs begins in the first decade of 20th century. In 1908, Edward Fath measured the untypical spectrum of nebula NGC 1068 (Fath, 1909). In the spectrum of this nebula, Fath noticed the existence of strong emission lines. Further discoveries have shown that it was the first measurement of the spectrum of a Seyfert galaxy. In 1917, this discovery was confirmed by Slipher from Lowell Observatory. At about the same time, in 1918 Curtis, using optical telescope, observed a bright line with the length equal to 11 seconds of arc from the nucleus of the object Virgo A in the Virgo cluster (Boettcher et al., 2012). It was the first observation of an astrophysical jet. 25 years later, in 1943, Seyfert observed the optical spectra of other objects with strong emission lines. He has found that the width of the broad emission lines corresponds to the velocity equal to 8500 km/s. However, a real breakthrough has come with the development of radio astronomy.

In the middle of 20th century, the radio astronomy was advanced enough to identify the optical objects with the radio point sources. In this way, such galaxies like Virgo A and Centaurus A were identified as strong radio sources (Bolton et al., 1949). Another radio source, which was paired with an optical object, was Cygnus A (Baade and Minkowski, 1954). The emission lines of highly ionized atoms, with width  $\sim 400$  km/s, was found in the optical spectrum of this object. Additionally, the large distance to the Cygnus A indicated large radio luminosity of the source. Further measurements showed that the optical object is located between two strong radio sources.

The growing number of paired radio and optical sources showed that some of them are distributed isotropically over the sky. This fact suggests their extragalactic origin. Most of them were identified as galaxies, due to the nebulosity of the optical images. However, a few of them were point-like optical objects. The spectra of these peculiar objects showed broad emission lines. The dominant belief was that these point-like objects are unusual stars (Shields, 1999). In 1963, Schmidt measured the redshift of one of the point-like objects assuming the cosmological redshift of the broad lines in the spectrum of 3C 273 (Schmidt, 1963). The measured redshift was  $z = 0.16$  and corresponding distance is  $\sim 750$  Mpc. Such a large distance means that the luminosity of 3C 273 was 100 times greater than the luminosity of the Milky Way (Peterson, 1997). Another object of this type, 3C 48, was characterized by even larger redshift,  $z = 0.37$  (Greenstein and Matthews, 1963). These objects began to be called quasi-stellar radio sources or quasars.

At that time, the physical interpretation of AGN phenomenon began to emerge. In 1959, Woltjer (1959) came to the conclusion that the properties of Seyfert galaxies were persistent (with a low limit of their lifetime of the order of  $10^8$  years), the nuclei were spatially small ( $< 100$  pc) and extremely massive ( $> 10^8$  solar masses). Study of quasars led Greenstein and Schmidt (1964) to similar conclusions.

With the next years, the large number of new discoveries expanded our knowledge

about AGNs. The pioneering X-ray experiments showed the coincidence between positions of some AGNs and X-ray sources. Continuous improvement of the resolution of radio techniques allowed to study the morphology of jets. In 1971, the superluminal motion of radio structures in jets was discovered in quasars (Shields, 1999). In 1978, Swanenburg et al. (1978) detected the  $\gamma$ -ray radiation from 3C 273 showing that a significant part of the radiation is emitted in  $\gamma$ -rays.

All these observational breakthroughs, supported by theoretical studies, led us to the current understanding of the AGNs phenomenon.

## 1.2 Central engine and unification view of AGNs

In accordance with the present knowledge about AGNs, the central region of every AGN have a quite similar structure. A Super-massive black hole (SMBH) is located at the center of a galaxy. The masses of SMBHs are in range from  $M_{BH} = 10^6 M_{\odot}$  to  $M_{BH} = 10^{10} M_{\odot}$ , where  $M_{\odot}$  is the mass of the Sun. For example, the mass of the black hole in the nearby radio galaxy M87 is estimated on  $M_{BH} = 6.4(\pm 0.5) \times 10^9 M_{\odot}$ . More about the estimation of SMBHs masses can be found in Chapter 3.

A SMBH is ringed by an accretion disk. The accretion disk is formed by the gas, with the angular momentum, gravitating to a SMBH. The matter in the accretion disk spirals into a SMBH due to the loss of the angular momentum. During this accretion process, a part of the gravitational energy is transferred into the thermal energy. The hot gas cools down radiating the thermal energy. The temperature of the inner parts of the accretion disk in AGNs is estimated on  $\sim 10^5$  K. Hence, accretion disks in AGNs emit most of the radiation in the optical and the UV ranges of the electromagnetic spectrum.

The accretion process provides an efficient way to convert the gravitational potential energy into the other form, e.g. thermal radiation. The ratio between the rest mass energy of the accreted matter and energy converted into radiation is given by the coefficient  $\eta$ , i.e.

$$\eta = \frac{L_{disk}}{\dot{M}c^2}, \quad (1.1)$$

where  $L_{disk}$  is the accretion disk luminosity,  $\dot{M}$  is the mass accretion rate and  $c$  is the speed of light. The accretion efficiency of the matter into the black hole is of the order of  $\eta \approx 0.1$  (Frank et al., 2002). The maximum value of the accretion efficiency depends on the spin of the black hole. It ranges from  $\eta = 0.06$ , for the nonrotating black hole, up to  $\eta = 0.4$ , for a black hole with the maximum possible angular momentum. For the comparison, the efficiency of the conversion of hydrogen to helium in nuclear reactions within stars is  $\eta = 0.007$ .

The luminosity of the accretion disk is often expressed in the Eddington luminosity units,  $L_{Edd}$ . The Eddington luminosity determines the maximum luminosity of the

spherical accretion process. In such a case,  $L_{Edd}$  corresponds to the balance between the radiation pressure and the gravity. In the case of the accretion disk, the disk luminosity can be even larger than  $L_{Edd}$ . Then, depending on the luminosity, accretion disks can be divided into two groups: sub-Eddington, when the luminosity of the disk is smaller than  $L_{Edd}$ , and super-Eddington accretion disks when the disk luminosity is  $> L_{Edd}$ .

The standard model of the accretion disk, typically applied to AGNs, has been proposed by Shakura and Sunyaev (1973). It belongs to the type of the sub-Eddington accretion disks. This model describes a stationary accretion disk in which the viscosity is characterized by the constant parameter  $\alpha$ . The Shakura-Sunyaev disk is geometrically thin, i.e. the vertical thickness of the disk is much smaller compared to the radial size. Nevertheless, the disk is optically thick, i.e. a photon cannot pass through the disk without absorption. The characteristic temperature of the gas depends on the radius of the disk as  $T \propto r_d^{-3/4}$ . The radiation emitted by the Shakura-Sunyaev disk is the superposition of the black body radiation emitted by rings of the accretion disk at its different radii.

The other type of an accretion applied to AGNs is the Advection Dominated Accretion Flow (ADAF), see Narayan and McClintock (2008). This model is characterized by a small opacity (optically thin disk) and an inefficient production of radiation. This sub-Eddington accretion disk is expected to exist in a low luminosity AGNs, such as M87. In the super-Eddington regime, there are mainly considered two models: the slim accretion disk and thick accretion disk. More details about accretion disks can be found in Abramowicz and Fragile (2013).

The accretion disk and the black hole in the central part of AGNs are surrounded by an obscuring dusty torus which is located at the accretion disk plane. The distance between a SMBH and a torus is typically several parsecs. A torus is optically thick. It absorbs radiation emitted in the vicinity of a SMBH. This radiation is re-emitted in the form of the infrared radiation.

Closer to a SMBH ( $< 1$  pc), small clouds of matter are present. They move with relatively high velocities, of the order of several 1000 km/s. The matter in the clouds is ionized by radiation from the disk and re-emitted as the broad lines. The place where the broad lines are produced is called the Broad Line Region (BLR). The clouds at larger distances emit narrow emission lines. The characteristic velocity of them is lower than in the BLR, i.e. of the order of  $\sim 300$  km/s.

In some AGNs, prominent jets are present. Jets are the collimated outflows of plasma moving perpendicular to the accretion disk. The plasma in jets moves with relativistic velocities. Jets are responsible for the radio loudness of AGNs. In many cases, the radiation from the jet dominates over the radiation from the other components of the galaxy.

Based on the above picture of the AGN central engine, the unification model of

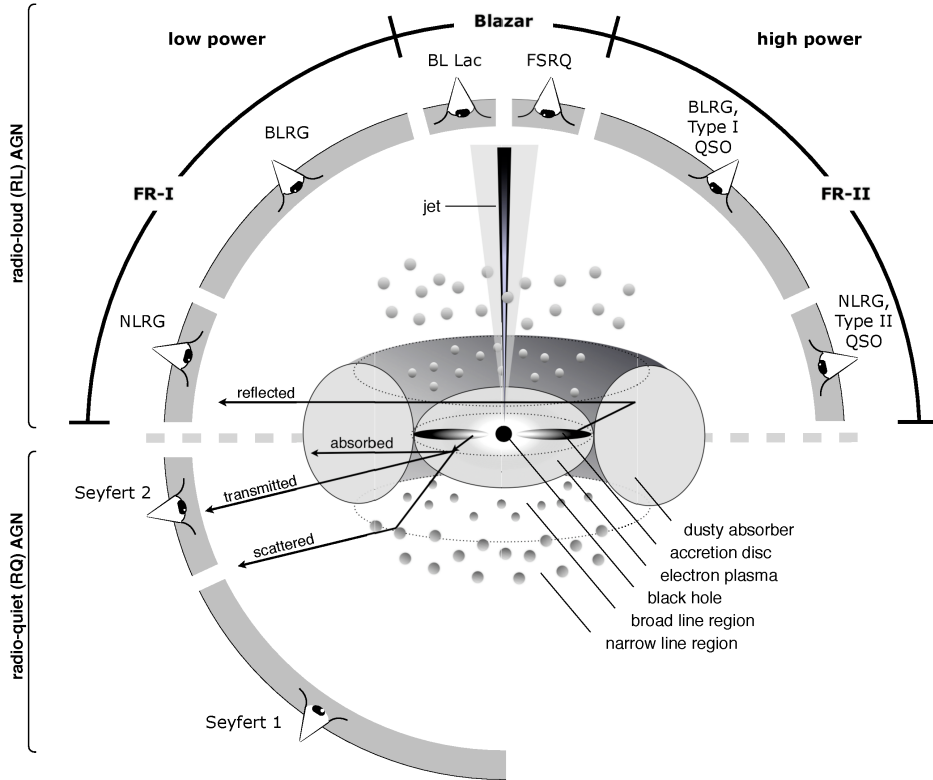


Figure 1.3: The picture of the central engine of AGNs with all characteristic components present at the vicinity of the SMBH. The different types of observed AGNs depends on the observation angles (from Beckmann and Shrader (2012)).

AGNs has been developed (see Fig. 1.3; Antonucci, 1993; Urry and Padovani, 1995). The central engine is not spherically symmetric. Then, the AGN shows different features depending on the mutual position of the observer and the plane of the accretion disk. When the AGN is observed at large angle to the AGN jet, the broad lines are hidden behind the dusty torus. Because of that, observed spectra show only the narrow lines. When the angle between the line of sight and the AGN axis is smaller, the broad lines become visible in the spectrum. This mechanism explains the existence of AGNs with the broad lines in the spectrum (like Seyfert 1 and BLRG) and without them (Seyfert 2 and NLRG).

The radio loudness depends on the jet presence. The angle between the jet axis and the line of sight (the observation angle) determines the observed type of the AGN (Urry and Padovani, 1995). AGNs observed at a small observation angle belong to the class of BL Lac objects and radio-loud Quasars, called together blazars. Radio galaxies are characterized by large observation angles. Due to the relativistic motion of the plasma in jets, emitted radiation is strongly enhanced by the Doppler boosting in the case of jets observed at small angles to the jet axis (see: Chapter 2). In such a case, the radiation from the jet can dominate over the radiation from other galaxy components.

Except for the radio loudness and the emission line properties, AGNs can be divided

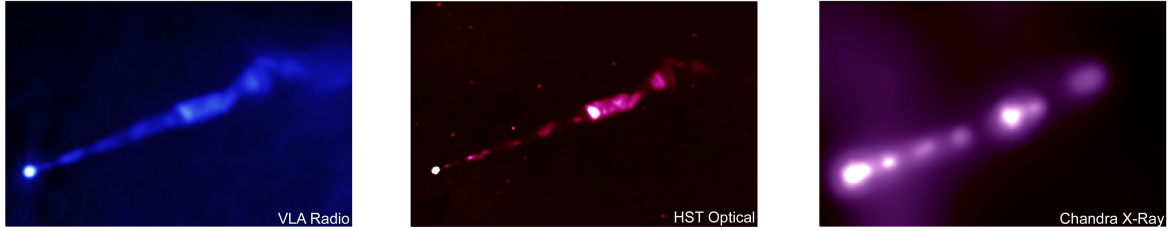


Figure 1.4: The kiloparsec jet of radio galaxy M87 observed in three different energy ranges: in radio range with the Very Large Array (left picture), in optical range with the Hubble Space Telescope (central) and in X-rays with the Chandra X-ray Observatory (right). Picture from: <http://apod.nasa.gov/apod/ap011101.html> (Authors: X-ray – H. Marshall (MIT), et al., CXC, NASA; Radio – F. Zhou, F. Owen (NRAO), J. Biretta (STScI); Optical – E. Perlman (UMBC), et al., STScI, NASA).

depending on the accretion rate. The AGNs with larger accretion rates and similar masses of the SMBH are more luminous. For example, the observed luminosities of the Seyfert galaxies are relatively small, despite large accretion rates. This effect is caused by a relatively small mass of SMBH. The main components of the AGN central engine and the unification scheme of AGNs are summarized in Fig. 1.3.

### 1.3 Jets from AGNs

Jets are collimated outflows of plasma moving with relativistic velocities. Astrophysical jets are present in many objects like gamma-ray bursts (Kumar and Zhang, 2015), microquasars (Mirabel and Rodríguez, 1999), and protostars and young stars (Bachiller, 1996). Jets are observed also in some types of AGNs. The presence of jets in AGNs is associated with the radio loudness and a strong  $\gamma$ -ray emission.

Jets in AGNs are vast objects. The linear size of a jet in an AGN may significantly exceed the diameter of a host galaxy. The linear size of the largest jet observed in an AGN is of the order of mega-parsecs (Machalski et al., 2008). Because of a very large size of jets, they can be spatially resolved by radio telescopes and, for the nearest objects, by optical and X-ray telescopes. The example of the jet observed in the different ranges of the electromagnetic spectrum is shown in Fig. 1.4. Note the very small width of the jet with respect to its length.

From the other side, jets are launched on much smaller, sub-parsec, scale. The typical size of the jet close to the SMBH is of the order of the Schwarzschild radius, i.e.

$$R_{Sch} = \frac{2GM_{BH}}{c^2} = 2.95 \times 10^5 \frac{M_{BH}}{M_{\odot}} \text{cm}, \quad (1.2)$$

where  $M_{BH}$  is the SMBH mass and  $G$  is the gravitational constant. The example of the jet on various scales, from kilo-parsecs to parsec-scale, is shown in Fig. 1.5. The jet at such a small scale cannot be directly observed due to the limited resolution of

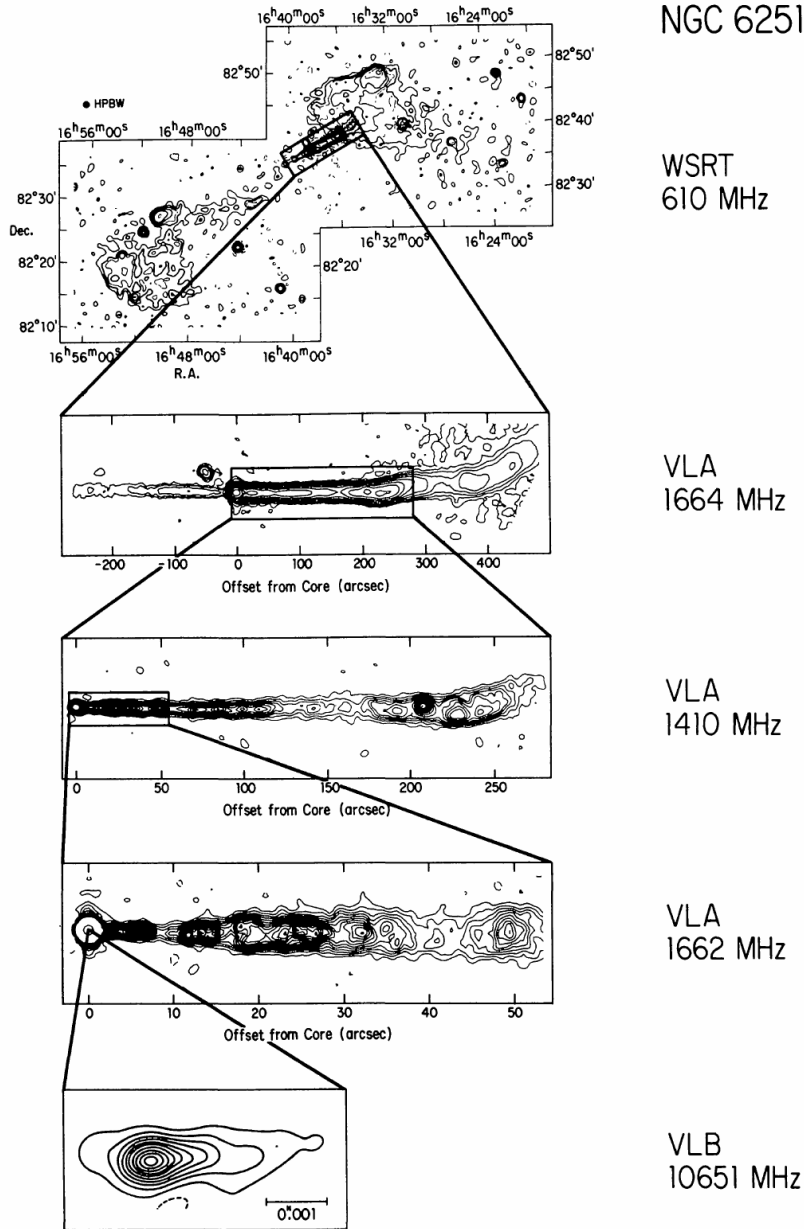


Figure 1.5: The radio structure of the jet in NGC 6251 from Mpc scale to pc scale. The relation between the projected size and the position angle for this source is: 1 arcsec  $\sim$  400 pc (Perley et al., 1984). Figure from Bridle and Perley (1984). Data are taken from Cohen and Readhead (1979), Willis et al. (1982) and Perley et al. (1984))

modern telescopes and the absorption of radiation. Hence, the role of theoretical and numerical models is very important in the understanding of the launching process of AGN jets.

Current models of jet launching assume the crucial role of the magnetic field in the formation, collimation, and acceleration of AGN jets. As the source of energy for the jet is usually considered the rotational energy of the spinning SMBH and the gravitational

energy of the matter in an accretion disk. The process of energy extraction from a rotating black hole has been firstly proposed by Penrose (1969). In the case of AGNs, the related mechanism allows releasing the spinning energy of the SMBH (Blandford and Znajek, 1977). In this process (called Blandford-Znajek mechanism), the SMBH is immersed in the poloidal magnetic field. The rotational energy of the SMBH is extracted by the magnetic field. The predictions of the Blandford-Znajek mechanism has been confirmed by numerical simulations (e.g Komissarov, 2001).

The second possibility of powering of AGN jet is the extraction of energy from an accretion disk. Such a process has been presented by Blandford and Payne (1982). In this model, the matter from the disk is expelled by the centrifugally driven outflow. Afterward, the outflow is collimated by the toroidal component of the magnetic field. In such a mechanism, the outflowing plasma consists of ions and electrons. In the case of Blandford-Znajek mechanism, it is believed that plasma mainly consists of electron-positron pairs. It is possible that in AGNs both processes play an important role. Such a two-component jet has been considered, for example, by Sol et al. (1989). It should be noted, that also other possibilities of the jet formation has been proposed. For instance, Lovelace (1976) and Blandford (1976) have proposed the electric-dynamo model.

The plasma inside the parsec-scale jets in AGNs is accelerated to the relativistic velocities and strongly collimated. The apparent velocities of plasma in blazar jets are of the order of  $\beta_{app} \sim 10c$ , where  $c$  is the speed of light. The velocity can reach in some cases even  $50c$  (Lister et al., 2009). The observation of the superluminal motion of the specific components in jets indicates that the Lorentz factor of the plasma is  $\Gamma_j \geq \beta_{app}$  (more details about superluminal motion can be found in Chapter 2). Because of the large Lorentz factors of jets, the relativistic effects must be included when jet properties are considered. For example, the radiation emitted by the AGN jets is boosted as a result of the Doppler beaming, especially for observers located at a small angle to the jet axis. This effect makes blazars, the excellent tool for the investigation of the physics of AGN jets. In blazars, the radiation from the jets is much more luminous in comparison to the radiation produced by their host galaxies or accretion disks.

## 1.4 Emission from the AGN jets

Radiation from jets in AGNs ranges from radio to very high energy (VHE)  $\gamma$ -rays. The convenient way to present its spectral energy distribution (SED) is to use the logarithmic plot of  $\nu F_\nu$  against  $\nu$  (where  $\nu$  is the frequency and  $F_\nu$  is observed flux [ $\text{erg cm}^{-2} \text{s}^{-1} \text{Hz}^{-1}$ ]). Such a plot shows what power is radiated in every decade of energy.

Typically, the SEDs of the inner jets from AGNs show two humps on the  $\nu F_\nu$  plot. The first, low-energy hump extends from radio to optical, UV or even X-ray range. The second hump is located in X-ray and  $\gamma$ -ray ranges. These humps are clearly visible in SEDs of two different objects, radio galaxy M87 and blazar Mrk 501 (see: Fig. 1.6).

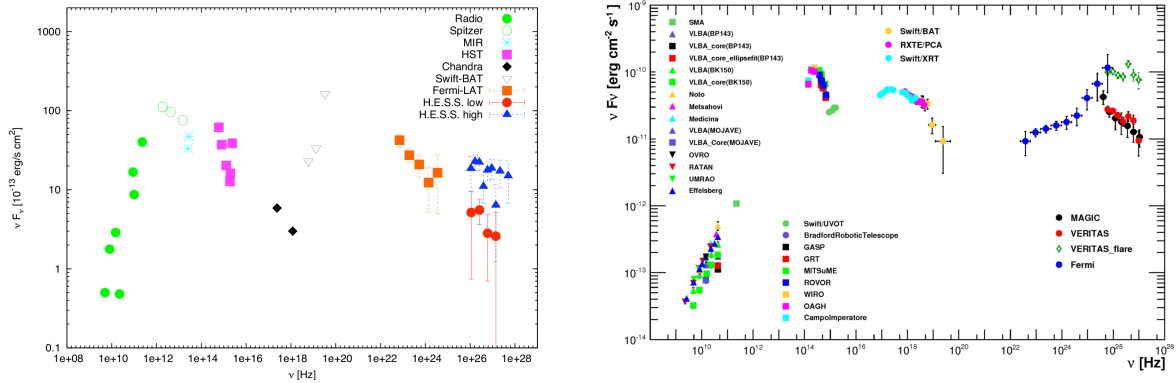


Figure 1.6: The examples of the spectral energy distributions (SEDs) of the two AGNs: radio galaxy M87 (left plot, from Rieger and Aharonian (2012)) and BL Lac object, Mrk 501 (right plot, from Abdo et al. (2011a)). Note, how the data points form two humps in every SED.

The double-humped shape of SEDs can be characterized by the peak frequency of the humps ( $\nu_s$  for the peak of first hump and  $\nu_c$  for the peak of the high energy hump) and the luminosity of the humps ( $L_s$  for the luminosity of low energy hump and  $L_c$  for luminosity of the high energy hump).

The best objects for the studies of emission properties from AGN jets are blazars. The radiation from the blazar jets is enhanced due to the relativistic boosting. Hence, it is easier to separate the radiation of the jet from the radiation of the accretion disk, the dusty torus or the host galaxy. Blazars consist of FSRQs and BL Lac objects. The latter, are divided into three groups depending on the frequency of the first peak,  $\nu_s$ :

- low-frequency peaked BL Lacs (LBLs), for  $\nu_s < 10^{14}$  Hz;
- intermediate-frequency peaked BL Lacs (IBLs), for  $10^{14}$  Hz  $< \nu_s < 10^{15}$  Hz;
- high-frequency peaked BL Lacs (HBLs), for  $\nu_s > 10^{15}$  Hz.

The statistical study of blazars shows that these objects form a sequence of features depending on their bolometric luminosities (Fossati et al., 1998). With increasing luminosity of a blazar, the low energy peak,  $\nu_s$ , and the high energy peak,  $\nu_c$ , are being shifted to the lower frequencies. The ratio between the luminosity of both peaks,  $L_s/L_c$ , decreases with the increasing bolometric luminosity of the blazar. Therefore, the specific type of blazars is arranged in the following sequence: HBLs – IBLs – LBLs – FSRQs according to increasing luminosity. This *blazar sequence* is shown in Fig. 1.7.

### 1.4.1 $\gamma$ -rays from jets in AGNs

In 1978, the first AGN, quasar 3C 273, has been detected in  $\gamma$ -rays (Swanenburg et al., 1978). The detection of other  $\gamma$ -ray sources took more than a decade (Hartman et al., 1992). The breakthrough came with the launch of the Compton Gamma Ray Observatory (CGRO) with the Energetic Gamma Ray Experiment Telescope (EGRET). The

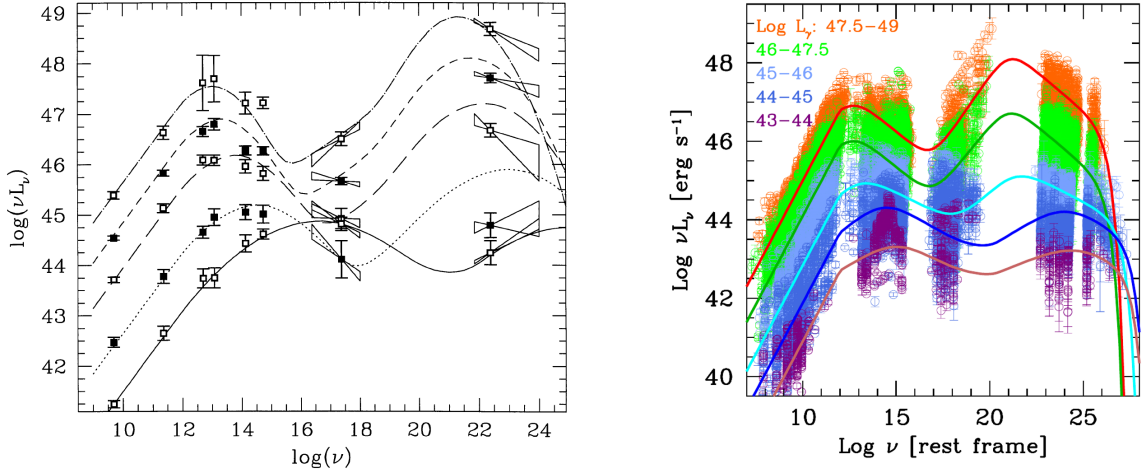


Figure 1.7: The blazar sequence in the original version (left plot; from Fossati et al., 1998) and the current version (right plot; from Ghisellini, 2016). The frequency of peaks decrease with increasing bolometric luminosity of blazars. Simultaneously, the ratio between low energy and high energy humps decreases.

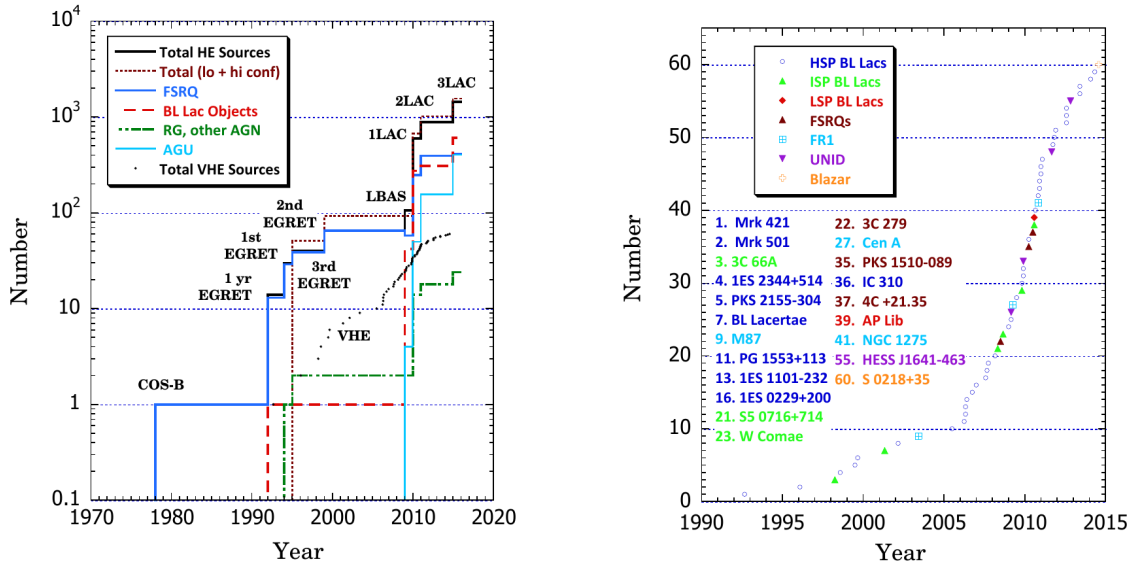


Figure 1.8: The number of detected  $\gamma$ -ray sources over the years. Left: the number of sources detected in GeV range. Right: the number of sources detected in TeV range (from Dermer and Giebels, 2016).

mission of the CGRO has shown that the  $\gamma$ -ray emission from AGNs is common. Today, the total number of known  $\gamma$ -ray AGNs exceeds 1500 in the GeV range (Ackermann et al., 2015). We also know almost 70 AGNs which emit  $\gamma$ -rays in the TeV energies (Prandini, 2017). The growing number of  $\gamma$ -ray sources is shown in Fig. 1.8.

The detection of  $\gamma$ -rays from AGN jets indicates the existence of extreme processes and conditions inside jets. The energy of particles emitting the  $\gamma$ -rays must be of the order of the energy of detected photons. Furthermore, the  $\gamma$ -ray emission from the AGNs is characterized by violent variability. Frequently, time variability of  $\gamma$ -rays from

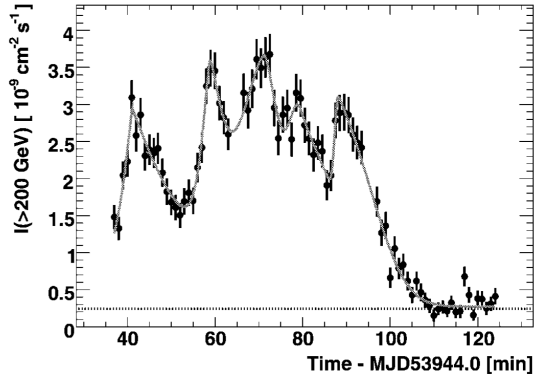


Figure 1.9: The extremely fast flare of BL Lac object PKS 2155-304 observed in 2006 (from Aharonian et al. (2007)).

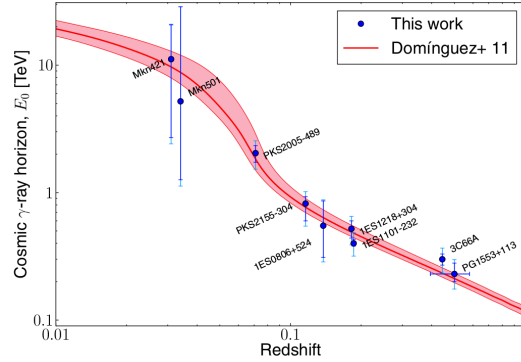


Figure 1.10: The  $\gamma$ -ray horizon caused by the absorption on the EBL. The red line defines the distance where the optical depth for  $\gamma$ -rays with specific energy is  $\tau_{\gamma\gamma} = 1$  (from Domínguez et al. (2013))

blazars is as short as a few hours (e.g. Saito et al., 2013; Hayashida et al., 2015), or even a few minutes (Aharonian et al., 2007; Albert et al., 2007; Aleksić et al., 2014b). The example of the extremely fast variability observed in the case of the BL Lac object, PKS 2155–304, is shown in Fig. 1.9.

The variability time scale,  $t_{var}$ , limits the dimension of emission region in a jet. According to causality argument and relativistic effects, the radius of the emission region can be approximated as  $R > t_{var}cD$ , where  $D$  is the Doppler factor. However, the small radius of the emission region means that the photon density has to be large. In such an environment, the absorption of HE  $\gamma$ -rays in the  $e^\pm$  pair creation process,  $\gamma + \gamma \rightarrow e^+ + e^-$ , is very efficient. Then, the observation of extremely fast flares requires large Doppler factors (see Begelman et al., 2008).

VHE  $\gamma$ -rays from extragalactic sources can be also absorbed in the extragalactic background light (EBL). The EBL is the integrated light emitted by galaxies during the whole history of the Universe. Hence, the EBL contains information about the evolution of the Universe (see the review about EBL in Dwek and Krennrich, 2013). The probability of the interaction between the EBL photon and the  $\gamma$ -rays is considerable due to the vast distance between the Earth and the AGNs. Then, the observed spectrum from the distant AGN is partially absorbed. The probability of absorption in general increases with increasing energy of the  $\gamma$ -ray photon. Because of that, the most energetic radiation from AGNs are observed only from the closer objects (see: Fig. 1.10). From the other side, knowing the intrinsic spectrum of AGNs at different distances, it is possible to constrain the EBL (Abramowski et al., 2013). Additionally, the absorption of  $\gamma$ -rays on the EBL can be used to limit the strength of the intergalactic magnetic field (Neronov and Vovk, 2010). The  $e^\pm$  pairs, created in the absorption process of  $\gamma$ -rays on the EBL, develop electromagnetic cascades. The extension and the level of GeV  $\gamma$ -ray emission produced in such cascades from distant TeV blazars

allows us to put the constraints on the intergalactic magnetic field.

## 1.5 Motivation for modeling the non-thermal emission from AGN jets

Almost all information which we know about AGN jets comes from the electromagnetic radiation, i.e. from its temporal, spectral and polarization measurements. Then, the indispensable tools to study physics of jets in AGNs are emission models. The reconstruction of the emitted spectrum and the temporal behavior of the radiation from jets with theoretical models allows to determine the possible conditions occurring in the emission region. A proper model of a jet in AGN may bring us closer to finding the answers to following questions:

- Which particles contribute to the radiation emitted by jets – electrons (and positrons), protons or maybe both?
- How the emitting particles are accelerated?
- What is the jet composition of the emission region?
- How the central engines of AGNs are built?
- Where is the emission region in the jet located?
- Is there only one emission region or a few?

The answers to these questions expand our knowledge about the physics of jets. The properties in the emission region should be related to the conditions in the central engine of an AGN. They are the consequences of their launching process, acceleration, collimation and dissipation mechanisms occurring in jets.

Today, the most popular interpretation of the multiwavelength spectra of blazars is the one-zone homogeneous leptonic model (more about emission models can be found in Chapter 3). This model, in spite of its simplicity, reproduces substantial features of the multiwavelength spectra of blazars. However, the constantly increasing sensitivity of telescopes and detectors reveal new details of the radiation emitted by jets from AGNs, such as the relationship between variability in different energy bands and the detailed spectral-features of the multiwavelength SED. The observed properties are difficult to explain with the simplest one-zone models. Therefore, the more complex models are needed to explain the observed properties.

For example, confirmation or rejection of hadronic models has the consequences for cosmic ray physics. The jets in AGNs are suspected to be the places of the acceleration of cosmic rays to the ultra-high energies. Blazars, as a VHE  $\gamma$ -ray emitters, can be also used as probes of the intergalactic space. VHE  $\gamma$ -rays are absorbed on the EBL

in  $e^\pm$  pair creation process. These pairs can initiate electromagnetic cascades in the intergalactic magnetic field. Knowing intrinsic VHE spectrum emitted by blazars, it is possible to constrain the EBL and the strength of the IGMF.

All of this shows the importance of the modeling of the emission from AGN jets. This thesis is devoted to emission models of non-thermal radiation from the jets. The aim of my thesis is to develop advanced emission models describing the high energy processes occurring in AGN jets. The thesis is organized as follows. I start with the characterization of the jet physics. In Chapter 2, I describe the most important radiation processes considered in my thesis and summarize the relativistic effects occurring in the AGN jets. Chapter 3 is devoted to the modeling of the jet emission. I present basic constraints of the parameters inside the emission region and shortly overview of the models of the jet emission proposed so far. In Chapter 4, I describe the inhomogeneous and non-local synchrotron self-Compton (SSC) model for the stationary emission from the parsec-scale jet. Based on this model, I present the stratified jet model in Chapter 5. In this model, the jet consists of the two parallel and inhomogeneous layers – a spine and a sheath. The electromagnetic cascades propagating in the inhomogeneous jet are studied in Chapter 6. The thesis is concluded and summarized in Chapter 7.

# Chapter 2

## Parsec-Scale Jets in AGNs

### 2.1 Motion of plasma in relativistic jets

The plasma in AGN jets moves with the relativistic speed. One of the most convincing proofs for that is the superluminal motion observed in AGN jets. The apparent speed of bright components (radio knots) in AGN jets is very often higher than the speed of light,  $c$ . The superluminal motion is a geometrical effect caused by the motion of a source moving with the relativistic speed at a small angle to the line of sight.

To find the explanation of the superluminal motion of radio knots in AGN jets, let's

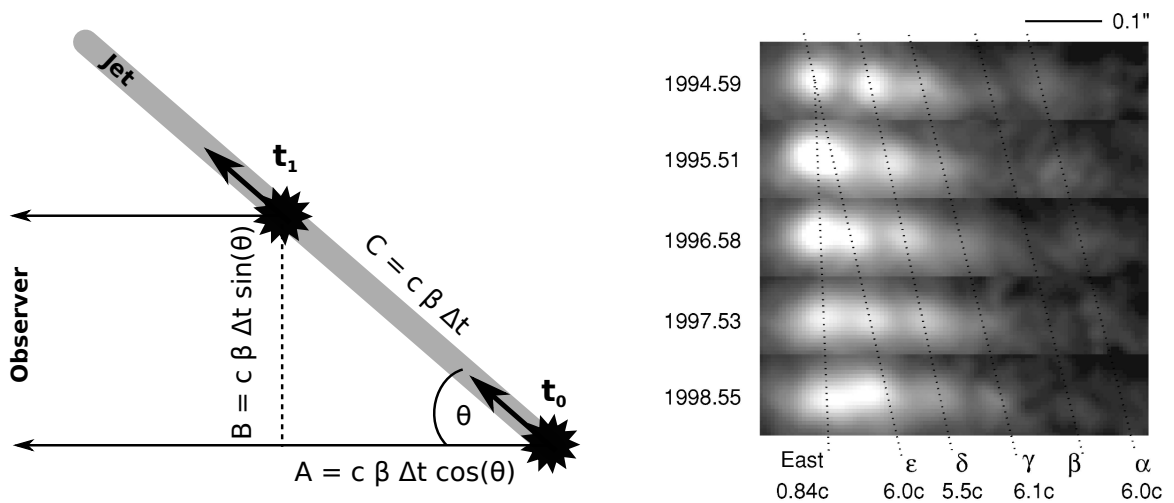


Figure 2.1: Left: The source (black star) moves along the jet (grey thick line) with the velocity  $c\beta$ . The apparent speed of the source depends on  $\beta$  and the angle between the jet and the line of sight,  $\theta$ . The apparent speed can be found measuring the observation time of two photons emitted at time  $t_0$  and  $t_1$  and position of the source across the sky at the moment of photons detection. Right: The sequence of images of the jet in the radio galaxy M87. Pictures are taken by the Hubble Space Telescope between 1994 and 1998. The dotted lines show the position of radio knots over the time. The apparent speed of the knots is  $\sim 6c$  (from Biretta et al. (1999)).

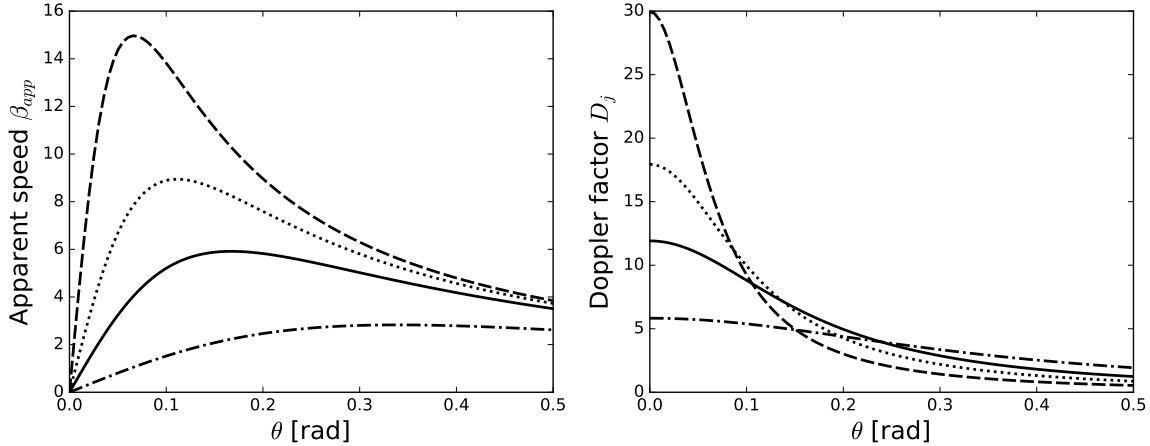


Figure 2.2: Right: The relation between the observation angle  $\theta$  and the apparent speed for specific values of the bulk Lorentz factor. Left: The relation between the observation angle  $\theta$  and the Doppler factor for specific values of the bulk Lorentz factor. The value of the Lorentz factor is:  $\Gamma = 3$  (dot-dashed line),  $\Gamma = 6$  (solid),  $\Gamma = 9$  (dotted) and  $\Gamma = 15$  (dashed line).

consider a distant source moving with the velocity  $\beta$  (in units of the speed of light,  $c$ ) at an angle  $\theta$  to the line of sight (see Fig. 2.1). Let us assume that the source emits two photons at the time  $t_0$  and  $t_1$ . During the time interval  $\Delta t = t_1 - t_0$ , the source travels the path  $C = c\beta\Delta t$ . In this same time, the photon emitted at  $t_0$  travels the path  $c\Delta t$ . The observer detects second photon after the time  $\Delta t_{obs} = c\Delta t - C \cos(\theta)$ . The position of the source changes by  $C \sin(\theta)$  after the time  $\Delta t_{obs}$ . Hence, the relation between the real speed of the emitting region,  $\beta$ , and the apparent speed  $\beta_{app}$  is given by

$$\beta_{app} = \frac{C \sin(\theta)}{\Delta t_{obs}} = \frac{\beta \sin \theta}{1 - \beta \cos \theta}. \quad (2.1)$$

For  $\beta \approx 1$  and  $\theta_{obs} \approx 1/\Gamma$  (where  $\Gamma = (1 - \beta^2)^{-1/2}$ ), the apparent speed is  $\beta_{app} \simeq (\Gamma^2 - 1)^{1/2}$ . The value of  $\beta_{app}$  for the different  $\Gamma$  and  $\theta$  is shown in Fig. 2.2.

The typical observed apparent speed of radio knots in AGN jets is  $\sim 10$  (Lister et al., 2009). It usually does not overcome 50. The correlation between the intrinsic power of the jet and the apparent speed is observed (e.g. Cohen et al., 2007). In the most powerful jets, the high apparent speed occurs more often. This indicates that weak jets are only mildly relativistic (Lister et al., 2013).

The other method to estimate the speed of the plasma in jets is the comparison of the observed brightness temperature of the jet,  $T_{obs}$ , with the brightness intrinsic temperature,  $T_{int}$ , which can be found assuming the equipartition between the relativistic electrons and the magnetic field (Readhead, 1994) or by avoiding “the Compton catastrophe” (Kellermann and Pauliny-Toth, 1969). The relation between observed and intrinsic brightness temperature is proportional to the Doppler factor  $D_j = [\Gamma(1 - \beta \cos \theta_{obs})]^{-1}$ . The relation between  $D_j$ ,  $\theta_{obs}$  and  $\Gamma$  is shown in Fig. 2.2.

Quantity in observer's rest frame	Relation to the source frame
time, $t$	$t' = tD_j$
photon energy, $\epsilon$	$\epsilon' = \epsilon/D_j$
cosine of the angle, $\cos \theta$	$\cos \theta' = (\cos \theta - \beta)/(1 - \beta \cos \theta)$
specific intensity, $I(\epsilon)$	$I'(\epsilon') = I(\epsilon)/D_j^3$
specific emissivity, $j(\epsilon)$	$j'(\epsilon') = j(\epsilon)/D_j^2$
absorption coefficient, $\alpha(\epsilon)$	$\alpha'(\epsilon') = \alpha(\epsilon)D_j$

Table 2.1: The most important relativistic transformations used in this work. The primed quantities are measured in frame co-moving with the source and unprimed in the observer's rest frame. In the observer's rest frame, the source moves with the velocity  $c\beta$  at the angle  $\theta_{obs}$ .  $D_j = 1/[\Gamma(1 - \beta \cos \theta_{obs})]$  is the Doppler factor.

Using both methods, Jorstad et al. (2017) measures of the Lorentz factor,  $\Gamma$ , and the Doppler factor,  $D_j$ , in 37 different AGN jets. The average  $\Gamma$  and  $D_j$  for FSRQ objects are  $11.6 \pm 3.1$  and  $13.1 \pm 6.3$ , respectively. In case of BL Lacs, the values are smaller,  $7.4 \pm 2.1$  and  $10.6 \pm 2.9$ , respectively. The above constraints clearly show that the plasma inside AGN jets moves with the relativistic speed.

However, it is obvious that the plasma at the beginning of a jet must move with a small speed,  $\Gamma \sim 1$ . The best object to study the motion in an AGN jet is the nearby radio galaxy M87. In this galaxy, the gradual acceleration, from sub-relativistic to relativistic speeds, is observed from  $\sim 10^2 R_{Sch}$  up to  $10^5 R_{Sch}$  (Asada et al., 2014; Mertens et al., 2016), where  $R_{Sch} = 2GM_{BH}/c^2$  is the Schwarzschild radius ( $G$  is the gravitational constant and  $M_{BH}$  is the mass of the black hole). These observations agree with the estimation of the bulk plasma acceleration for another nearby galaxy, Cen A (Krichbaum et al., 1998), and with the numerical simulations of the jet acceleration (e.g. Vlahakis and Königl, 2004).

Because of the relativistic speed of the plasma in AGN jets, the effects of special relativity must be taken into account when the physical quantities are transformed from the co-moving frame of the jet to observer's frame. The relations between quantities in different frames are given by the Lorentz transformations. The consequences of the Lorentz transformations, among others, are the length contraction in the direction of motion,  $\Delta x' = \Delta x/\Gamma$ , and the time dilation,  $\Delta t' = \Gamma \Delta t$ . The unprimed quantities are measured in the rest frame and primed quantities are measured in the frame moving with the velocity equal to  $c\beta$ .

Another consequence of relativistic motion is the Doppler effect. The Doppler effect describes the relationship between the photon frequency emitted by a moving source and measured by an observer. This relation is given by  $\nu = \nu'/[\Gamma(1 - \beta \cos \theta)] = \nu' D_j$ , where  $\theta$  is the angle between the velocity of a source and the line of sight and  $c\beta$  is the velocity of the source. The similar relation can be obtained for other physical quantities. For example, the apparent length of a moving bar, measured with photons

arriving at the same time, is  $l = D_j l'$ , where  $l'$  is the length of the bar in the comoving frame (Ghisellini, 2013). In the Table 2.1, I gather the most important relativistic transformations used in this work.

## 2.2 Geometry of the parsec-scale jet

Due to the large distances to the AGNs, the parsec-scale jets can be spatially resolved only with the very-long-baseline interferometry (VLBI). Then, the information about the geometry of jets in the smallest distance scales comes from the radio observations. Very often the shape of the parsec-scale jet is approximated as a cone with the half opening angle of a jet,  $\phi$ . The conical shape of a jet is consistent with the jet geometry in larger (kilo-parsec) scale. Due to the relativistic motion in jets, the opening angle of the jet should be inversely proportional to the Lorentz factor of a jet,  $\phi \simeq \rho/\Gamma_j$ , where  $\rho$  is the transverse expansion coefficient. The statistical studies of the jet opening angles with the MOJAVE program (long-term program to study radio structure and evolution of extragalactic jets) give the estimate for  $\rho = 0.26$  (Pushkarev et al., 2009) and  $\rho = 0.2$  (Clausen-Brown et al., 2013). However, the jet shape can be different from the conical one. Algaba et al. (2017) found that the average shape of the parsec-scale jet is quasi-parabolic, with the relation between the radius of a jet,  $R_j$ , and the distance from the SMBH,  $z$ , given by  $R_j \propto z^{0.85}$ .

One of the most important objects for the parsec-scale radio observations is FR I radio galaxy M 87. The relation between the distance from the SMBH,  $z$ , and the radius of the jet,  $R_j$ , for the parsec-scale jet of this source, is described by the power law,  $R_j \propto z^k$ , with  $k$  equal 0.59 (Asada and Nakamura, 2012), 0.56 (Hada et al., 2013) or 0.6 (Mertens et al., 2016). However, beyond  $z \approx 5 \times 10^5 R_{Sch} \approx 300$  pc, the geometry of the jet changes to conical one,  $R_j \propto z^1$ . The minimum transverse width of the jet in M 87, observed with VLBA (Mertens et al., 2016), is of the order of tens Schwarzschild radii. The similar shape of the parsec-scale jet has been observed for FR II radio galaxy Cygnus A (Boccardi et al., 2016b). The profile of the innermost jet is described by  $R_j \propto z^{0.55}$ . But in this case, the minimum transverse width is  $\sim (227 \pm 98) R_{Sch}$  (Boccardi et al., 2016a).

In both cases, in M 87 and Cyg A, the transverse structure of the jet is observed. The limb brightening and kinematics of the jets suggest the existence of the spine-sheath structure, where the fast, inner layer is immersed in the slower, outer layer. The limb brightening was also observed in other sources (e.g. Piner et al., 2009; Nagai et al., 2014).

## 2.3 Transfer of radiation in jets

One of the most fundamental quantities of radiative transfer is the specific radiative intensity,  $I(\nu)$ . In CGS units system, the unit of the specific intensity is  $\text{erg s}^{-1} \text{cm}^{-2} \text{sr}^{-1} \text{Hz}^{-1}$ .  $I(\epsilon)dtdAd\Omega d\nu$  describes how much energy passes the unit surface,  $dA$ , in the unit time,  $dt$ , from the unit solid angle,  $d\Omega$ , and with the frequency of photons between  $\nu$  and  $\nu + d\nu$ . For convenience, in this work, I will describe the intensity (and other quantities associated with photons) in ranges of photon energy rather than frequency, i.e.  $\epsilon = h\nu$ , where  $h$  is the Planck constant.

For the beam of radiation passing through a medium, the intensity changes with distance. Emission and absorption processes modify the beam. Photons may also be scattered in a medium but the scattering effects are not considered in this work. The emission is characterized by the emission coefficient (or emissivity)  $j$ . It is defined as the energy emitted per the unit time, per the unit solid angle, per the unit volume, per the unit energy of radiation,

$$j = \frac{dE}{dV dt d\Omega d\epsilon}. \quad (2.2)$$

When a medium at the propagation distance,  $s$ , emits radiation with emissivity,  $j(s)$ , then the intensity increases after the distance  $S$  in following way:

$$I = I_0 + \int_0^S j(s) ds, \quad (2.3)$$

where  $I_0$  is the initial intensity.

The absorption process of the radiation is characterized by the absorption coefficient  $\alpha(s)$  [ $\text{cm}^{-1}$ ]. It describes the intensity decrement with the distance. The intensity absorbed in the medium after the path  $S$  is given by

$$I = I_0 \times \exp(-\tau(S)), \quad (2.4)$$

where

$$\tau(S) = \int_0^S \alpha(s) ds \quad (2.5)$$

is the optical depth. For the optical depth  $\tau = 1$ , the initial intensity is reduced by the factor equal to  $e$ . It defines the threshold between the optically thick and the optically thin medium. When the optical depth is higher than unity, we consider the medium as optically thick. It means that the absorption effects are significant. In the opposite case, when  $\tau < 1$ , the medium is optically thin or transparent.

The general form of the solution of the radiative transfer equation is

$$I(S) = I_0 \exp\left(-\int_0^S \alpha ds\right) + \int_0^S j(s) \times \exp\left(-\int_s^S \alpha(s') ds'\right) ds. \quad (2.6)$$

However, note that this solution does not include the scattering effects, which strongly complicate the equation. Fortunately, in the case of the radiation from AGN jets, the scattering effects can be omitted.

## 2.4 Radiation processes in leptonic jets

In my work, I assume that the radiation in the AGN jets is produced mainly by leptons ( $e^\pm$  pairs). Furthermore, it is believed that the density of the plasma in AGN jets is relatively small,  $n \sim 10^2 \text{ cm}^{-3}$  at 1 pc (O’Sullivan and Gabuzda, 2009). In such an environment, four radiation and absorption processes are especially important: (i) the synchrotron emission, (ii) the synchrotron self-absorption, (iii) the inverse Compton scattering and (iv) the  $e^\pm$  pair production in  $\gamma\gamma$  absorption.

### 2.4.1 Synchrotron radiation

Charged particles, moving with relativistic velocities in magnetic fields, produce synchrotron radiation. As a result, they lose energy. The synchrotron energy loss rate for the electron with the energy  $E_e = \gamma m_e c^2$  (where  $m_e$  is the electron rest mass and  $\gamma$  is the Lorentz factor of the electron) is given by

$$\frac{d\gamma}{dt} = -\frac{2\sigma_T}{m_e c} U_B \gamma^2 \beta^2 \sin^2(\alpha), \quad (2.7)$$

where  $\beta = \sqrt{1 - 1/\gamma^2}$  is the electron speed in units of  $c$ ,  $U_B = B^2/8\pi$  is the energy density of the magnetic field,  $\sigma_T$  is the Thomson cross section, and  $\alpha$  is the pitch angle, i.e. the angle between the magnetic field lines and the velocity of the electron (Rybicki and Lightman, 1986). The average loss rate for isotropic pitch angles (in the case of many isotropic electrons and/or random magnetic field lines) takes the form:

$$-\frac{d\gamma}{dt} = \frac{4\sigma_T}{3m_e c} U_B (\gamma^2 - 1). \quad (2.8)$$

The total synchrotron power per photon energy emitted by a single electron is

$$P_{\epsilon,\alpha}(\gamma, \epsilon, \alpha) = \frac{\sqrt{3}e^3}{m_e c^2 h} B \sin(\alpha) \times F\left(\frac{\epsilon}{\epsilon_\alpha}\right), \quad (2.9)$$

where  $e$  is the elementary charge,  $h$  is the Planck constant and

$$\epsilon_\alpha = \frac{3ehB}{4\pi m_e c} \gamma^2 \sin(\alpha), \quad F(x) = x \int_x^\infty K_{5/3}(y) dy. \quad (2.10)$$

$K_{5/3}$  is the modified Bessel function of the second kind of order  $5/3$ . Function  $F(x)$  defines the characteristic shape of the total synchrotron power. It peaks at  $x \approx 0.29$ . The function has two asymptotic forms for very small and very large values of  $x$ , i.e.

$$F(x) \propto \begin{cases} x^{1/3} & , \quad x \ll 1; \\ x^{1/2} \exp(-x) & , \quad x \gg 1. \end{cases} \quad (2.11)$$

In a rough approximation, the whole synchrotron energy is emitted in a narrow energy range around

$$\epsilon_0 \approx \frac{ehB\gamma^2}{4\pi m_e c} \approx 22.2 B_G E_{TeV}^2 \text{ keV}, \quad (2.12)$$

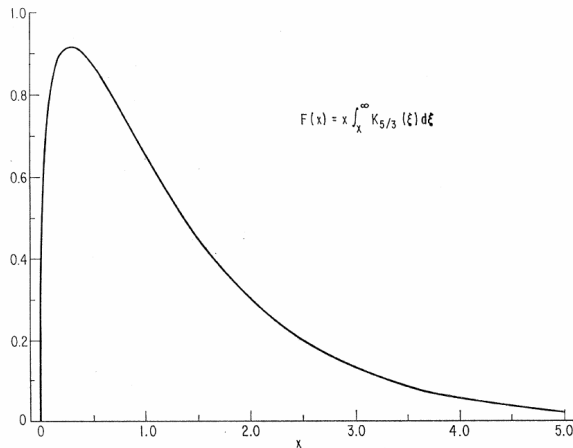


Figure 2.3: The function  $F(x)$ , which characterizes the synchrotron spectrum (from Blumenthal and Gould (1970)).

where  $B = 1B_G$  G and  $E_e = 1E_{TeV}$  TeV. This approximation is acceptable due to the relatively sharp shape of  $F(x)$  (see Fig. 2.3).

For numerical applications, when the magnetic field is randomly oriented, it is convenient to use the approximate form of the  $F(x)$  function,

$$F(x) \approx \frac{1.808x^{1/3}}{\sqrt{1 + 3.4x^{2/3}}} \frac{1 + 2.21x^{2/3} + 0.347x^{4/3}}{1 + 1.353x^{2/3} + 0.217x^{4/3}} \exp(-x). \quad (2.13)$$

This function, with accuracy better than 0.2%, has been obtained by Aharonian et al. (2010).

When the synchrotron radiation is emitted by electrons with the power-law distribution,  $N(\gamma) = K\gamma^{-s}$  between  $\gamma_{min}$  and  $\gamma_{max}$ , then the synchrotron emissivity,  $j_{syn}$ , can be calculated with

$$j_{syn}(\epsilon, \alpha) = \frac{1}{4\pi} \int_{\gamma_{max}}^{\gamma_{min}} N(\gamma) P_{\epsilon\alpha}(\gamma, \epsilon, \alpha) d\gamma. \quad (2.14)$$

The above synchrotron emissivity can be approximated by the power-law function with with the spectral index  $p = (s - 1)/2$  between  $\epsilon_{min}$  and  $\epsilon_{max}$  (given by Eq. 2.12 for  $\gamma_{min}$  and  $\gamma_{max}$ , respectively). Hence, knowing the shape of the synchrotron spectrum of any astrophysical object, one can find the spectral index of the distribution of electrons.

The synchrotron photons may be absorbed by non-thermal electrons. This process is called *the synchrotron self-absorption* (SSA). It can distort the synchrotron spectrum. In non-thermal synchrotron sources, the border between the optically thick and the thin part of a spectrum is given by the self-absorption frequency,  $\nu_{SSA}$  (Rybicki and Lightman, 1986). The optically thick part of the spectrum is given by the power-law function with spectral index equal to  $p = -5/2$ . SSA is described by an absorption coefficient, which is defined as (Ghisellini and Svensson, 1991)

$$\alpha_{SSA}(\epsilon) = \frac{h^3}{8\pi m_e \epsilon^2} \int \frac{N(\gamma)}{\gamma^2} \frac{d}{d\gamma} [\gamma^2 P_\epsilon(\epsilon)] d\gamma, \quad (2.15)$$

where  $P_\epsilon$  is the synchrotron power from Eq. 2.9 averaged over the pitch angle.

## 2.4.2 Compton scattering

Scattering of photons of energy  $\epsilon$  on electrons considered in the electron reference frame is called Compton scattering. This interaction is described by the Klein-Nishina cross section

$$\frac{d\sigma}{d\Omega} = \frac{r_0^2 \epsilon_1^2}{2 \epsilon^2} \left( \frac{\epsilon}{\epsilon_1} + \frac{\epsilon_1}{\epsilon} + \sin^2 \theta \right), \quad (2.16)$$

where  $r_0$  is the classical electron radius,  $\theta$  is the scattering angle, and

$$\epsilon_1 = \frac{\epsilon}{1 + (\epsilon_1/m_e c^2)(1 - \cos \theta)}, \quad (2.17)$$

is the energy of the photon after scattering. Formula 2.16 is obtained using the quantum electrodynamics. For the classical physics, where the photon energy is low ( $\epsilon \ll m_e c^2$ ) the Klein-Nishina formula simplifies to the Thomson formula. The cross section for the scattering in the Thomson regime is given by

$$\frac{d\sigma_T}{d\Omega} = \frac{1}{2} r_0^2 (1 + \cos^2 \theta). \quad (2.18)$$

After the integration over all scattering angles, the cross section is equal to  $\sigma_T = 8\pi r_0^2/3$ , which is called the Thomson cross section. On the other hand, when the photon energy is much larger than the rest energy of electron,  $\epsilon \gg m_e c^2$ , the Compton cross-section approaches

$$\sigma_C(\epsilon) \simeq \frac{3}{8} \frac{\sigma_T}{\epsilon} [\ln(2\epsilon) + 0.5]. \quad (2.19)$$

The above two approximations, Eq. 2.18 and Eq. 2.19, divide the Compton scattering process into two regimes:

- The Thomson regime, when the photon energy (in electron rest frame) is much smaller than the rest energy of an electron. The angle averaged Compton cross-section is equal to  $\sigma_T$ .
- The Klein-Nishina regime, when  $\epsilon/m_e c^2 \gg 1$ . The Compton cross section decreases with the energy of the initial photon.

When the scattering occurs between an electron with the large kinetic energy and a relatively low energetic photon in the observational reference frame, the energy of scattered photon may increase at the expense of the electron energy. Such a variant of the electron-photon scattering is called *the inverse Compton* (IC) process, in contrast to the Compton scattering where the electron at rest is usually assumed. The Compton up-scatter process is a very important production process of  $\gamma$ -rays in astrophysics.

Because of the anisotropy of the Compton cross-section formula, the detailed equation for the photon spectrum produced in the inverse Compton process has quite complex form. However, a few important (for astrophysical applications) approximations

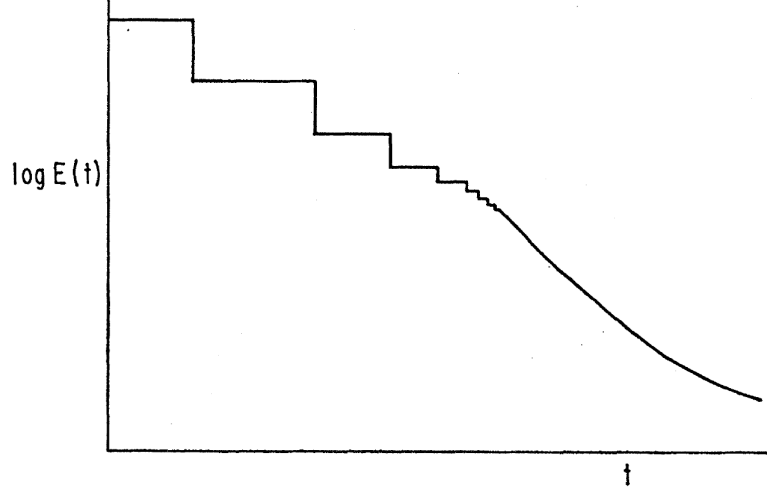


Figure 2.4: The evolution of energy of a relativistic electron as a function of time for the Compton scattering process in the Klein-Nishina regime (from Blumenthal and Gould (1970)).

can be found. In the case of isotropic ambient photons, with the number density  $n_{ph}$ , and the isotropic relativistic electrons, the spectrum of scattered photons is

$$\frac{dN_{\gamma,\epsilon}}{dt d\epsilon d\epsilon_s} = \frac{3\sigma_T}{4\epsilon\gamma} n_{ph}(\epsilon) \times G(q, \Gamma), \quad (2.20)$$

where

$$G(q, \Gamma) = 2q \ln q + (1 + 2q)(1 - q) + \frac{\Gamma^2 q^2 (1 - q)}{2(1 + \Gamma q)}, \quad (2.21)$$

$\Gamma = 4\epsilon\gamma/m_e c^2$ ,  $q = \epsilon_s/[\Gamma(\gamma m_e c^2 - \epsilon_s)]$  and  $\epsilon_s$  is the energy of the scattered photon (Blumenthal and Gould, 1970).

The second very important case is the scattering of directed photons on isotropic relativistic electrons (Aharonian and Atoyan, 1981). In such a case, the spectrum also depends on the scattering angle,  $\theta$ , and it is given by

$$\frac{dN_{\gamma,\epsilon,\theta}}{dt d\hat{\epsilon} d\hat{\epsilon}_s d\Omega} = \frac{3c\sigma_T}{16\pi\hat{\epsilon}\gamma^2} n_{ph,\theta}(\hat{\epsilon}) G_\theta(w, b_\theta), \quad (2.22)$$

where  $\hat{\epsilon} = \epsilon/m_e c^2$ ,  $\hat{\epsilon}_s = \epsilon_s/m_e c^2$ ,

$$G_\theta(w, b_\theta) = 1 + \frac{w^2}{2(1-w)} - \frac{2w}{b_\theta(1-w)} + \frac{2w^2}{b_\theta(1-w)^2}, \quad (2.23)$$

and  $b_\theta = 2(1 - \cos \theta)\epsilon\gamma$ ,  $w = \hat{\epsilon}_s/\gamma$ .

In the inverse Compton process, the energy of a relativistic electron is transferred to the scattered photons. In the Thomson regime, the energy of the electron, which propagates in radiation field with energy density  $u_{rad}$ , decreases according to

$$-\frac{d\gamma}{dt} = \frac{4\sigma_T\gamma^2 u_{rad}}{3m_e c}. \quad (2.24)$$

An electron scattering photons in the Thomson regime loses energy in small portions. Then, the above process can be considered as continuous. The opposite situation occurs in the Klein-Nishina regime where the electron loses energy in discrete amounts, comparable to the initial energy of an electron. This effect, combined with the smaller cross-section in the Klein-Nishina regime, leads to the evolution of the electron energy presented schematically in Fig. 2.4.

Deep in the Klein-Nishina regime, an electron, propagating in the field of ambient photons, loses energy in the random way. The average number of photons with energy between  $\epsilon_1$  and  $\epsilon_1 + d\epsilon_1$  emitted by the electron with energy  $E_e$  in the short time  $\Delta t$  can be calculated applying the formula for the photon spectrum (Eq. 2.20). This spectrum of produced  $\gamma$ -rays in Compton scattering is

$$\frac{dN_\gamma}{d\epsilon_1} = \Delta t \int_{\epsilon_{min}}^{\infty} \frac{dN_{\gamma,\epsilon}}{dt d\epsilon d\epsilon_1} d\epsilon, \quad (2.25)$$

where  $\epsilon_1$  is the scattered photon energy and  $\epsilon_{min} = m_e^2 c^4 / [4(E_e - \epsilon_1)]$  (Blumenthal and Gould, 1970).

In the case of the Klein-Nishina regime, the average energy loss rate is (Schlickeiser, 2009)

$$\frac{d\gamma}{dt} = -\frac{12\sigma_T}{m_e c} \gamma^2 \int_0^\infty d\epsilon n_{ph}(\epsilon) \int_0^1 dq \frac{qG(q, \Gamma)}{(1 + \Gamma q)^3}, \quad (2.26)$$

where  $G(q, \Gamma)$  is given by Eq. 2.23. In this case, the energy loss-rate increases logarithmically with increasing Lorentz factor of electrons,  $\gamma$ .

In the parsec-scale jets, electrons lose energy primarily on two processes: the synchrotron and the IC. In the Thomson regime, the form of the IC energy loss rate has a similar form to the synchrotron loss rate, i.e.  $\dot{\gamma} \propto \gamma^2 u$ , where  $u$  is the energy density of the magnetic field,  $u_B$ , in the case of the synchrotron process and it is the energy density of radiation,  $u_{rad}$ , in the case of the IC scattering. Then, the ratio of the IC and the synchrotron energy losses are proportional to the ratio of the energy densities of the magnetic field and the radiation, i.e.  $\dot{\gamma}_{IC}/\dot{\gamma}_{syn} \propto u_{rad}/u_B$ . However, in the Klein-Nishina regime, the form of the IC loss rate changes. The ratio between the energy losses can be expressed by the function  $F_{KN}$ , which depends on the electron energy and the spectrum of photons (Moderski et al., 2005),

$$\frac{\dot{\gamma}_{IC}}{\dot{\gamma}_{syn}} = \frac{u_{rad}}{u_B} F_{KN}. \quad (2.27)$$

The form of  $F_{KN}$  is shown in Fig. 2.5 for three different spectra of photons, where  $b = 4\epsilon_{max}\gamma/m_e c^2$  and  $\epsilon_{max}$  is the maximum energy of photons. It is clear that the synchrotron energy loss-rate dominates over the IC loss-rate for electrons with very large Lorentz factors when  $u_B \simeq u_{rad}$ .

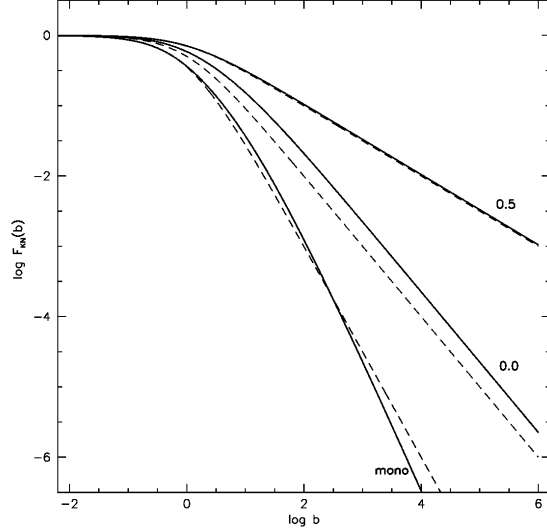


Figure 2.5: The ratio between the IC and the synchrotron energy loss-rates for  $u_{rad} = u_B$ , where  $b = 4\epsilon_{max}\gamma/m_e c^2$  (solid lines). The calculation obtained for three different energy distributions of photons: monoenergetic (mono), power law with index  $p = 0$  and power law with index  $p = -0.5$ . (from Moderski et al. (2005), the dashed lines show the analytical approximations).

### 2.4.3 The $\gamma$ -ray absorption in $e^\pm$ pair producton process

Two photons can interact with each other producing an electron-positron pair when their energy is sufficient. This process is possible when the energy of photons is larger than

$$\epsilon_1 \epsilon_2 > \frac{2(m_e c^2)^2}{1 - \cos \phi}, \quad (2.28)$$

where  $\phi$  is the angle between the direction of photons.

When the HE  $\gamma$ -ray photon propagates in the low energy photon field with the differential photon density at the angle  $\phi$ ,  $n_{ph,\phi}(\epsilon_2)$ , their absorption coefficient is given by (Gould and Schröder, 1967)

$$\alpha_{\gamma\gamma}(\epsilon_1) = \frac{1}{2} \int \int n_{ph,\phi}(\epsilon_2) \sigma_{\gamma\gamma}(\epsilon_1, \epsilon_2, \phi) (1 - \cos \phi) \sin \phi \, d\epsilon_2 d\phi, \quad (2.29)$$

where the total cross section for  $\gamma + \gamma \rightarrow e^+ + e^-$  process is

$$\sigma_{\gamma\gamma}(\epsilon_1, \epsilon_2, \phi) = \frac{\pi r_0^2}{2} (1 - \beta_{\gamma\gamma}^2) \left[ (3 - \beta_{\gamma\gamma}^4) \ln \frac{1 + \beta_{\gamma\gamma}}{1 - \beta_{\gamma\gamma}} - 2\beta_{\gamma\gamma}(2 - \beta_{\gamma\gamma}^2) \right], \quad (2.30)$$

and  $\beta_{\gamma\gamma} = (1 - 4m_e^2 c^4/s)^{1/2}$ ,  $s = 2\epsilon_1 \epsilon_2 (1 - \cos \phi)$ .

In the case of the isotropic radiation field the absorption coefficient takes a simpler form (e.g. Bednarek and Protheroe, 1999a):

$$\alpha_{\gamma\gamma}(\epsilon_1) = \frac{1}{8\epsilon_1^2} \int_{\epsilon_{min}}^{\epsilon_{max}} \frac{n_{ph}(\epsilon_2)}{\epsilon_2^2} \int_{s_{min}}^{s_{max}} s \sigma_{\gamma\gamma}(s) \, ds d\epsilon_2, \quad (2.31)$$

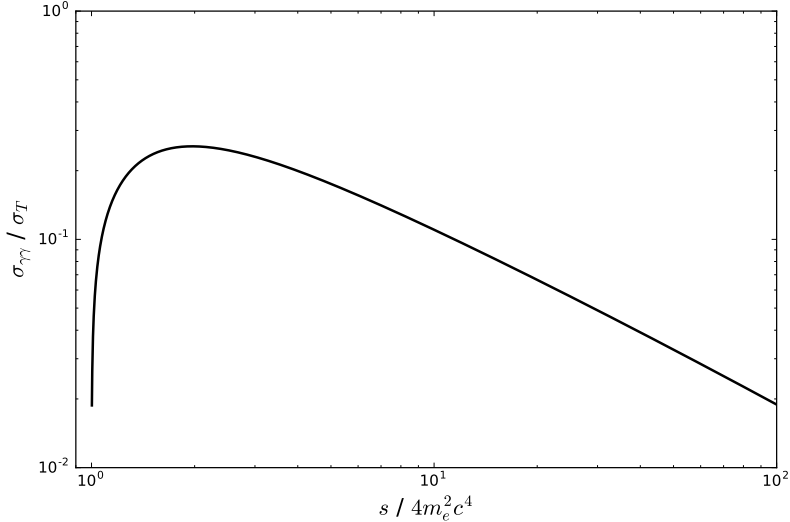


Figure 2.6: The total cross section for  $\gamma\gamma \rightarrow e^+ + e^-$  process, where  $s = 2\epsilon_1\epsilon_2(1 - \cos\phi)$ .

where  $n_{ph}(\epsilon_2)$  is the isotropic differential photon density,  $s_{min} = 4m_e^2c^4$  and  $s_{max} = 4\epsilon_1\epsilon_2$ .

The shape of the total cross section for the  $\gamma\gamma \rightarrow e^+e^-$  absorption is very sharp, with the peak at  $s \sim 2$ . Hence, the  $\gamma$ -ray photon with energy  $\epsilon_1$  interact mostly with photons with energy  $\epsilon_2 \simeq 4m_e^2c^4/[\epsilon_1(1 - \cos\phi)]$ . Due to the sharp shape of the total cross section, the rough estimation of  $\sigma_{\gamma\gamma}$  can be obtained with  $\delta$  approximation (Boettcher et al., 2012),

$$\sigma_{\gamma\gamma} \approx \frac{\sigma_T\epsilon_1}{3m_e c^2} \delta\left(\frac{\epsilon_1}{m_e c^2} - \frac{2m_e c^2}{\epsilon_2}\right), \quad (2.32)$$

where  $\delta$  is the Dirac delta function.

The energy of the electron-positron pair, which is created in the  $\gamma\gamma \rightarrow e^+ + e^-$  process, can be calculated with the following procedure (see Boettcher and Schlickeiser, 1997). The photon energy in the center-of-momentum frame is

$$\epsilon' = \sqrt{\frac{\hat{\epsilon}_1\hat{\epsilon}_2(1 - \cos\phi)}{2}}, \quad (2.33)$$

where  $\hat{\epsilon}_1$  and  $\hat{\epsilon}_2$  are the energies of colliding photons in units of  $m_e c^2$ , in laboratory frame. The lorentz factors of an electron and a positron in the center-of-momentum frame are  $\gamma'_\pm = \epsilon'$ . The center-of-momentum frame moves in the laboratory frame with the Lorentz factor equal to

$$\gamma_c = \frac{\hat{\epsilon}_1 + \hat{\epsilon}_2}{2\epsilon'}. \quad (2.34)$$

Hence, the energy of the electron (or the positron) in laboratory frame, created in collision of two photons, is

$$\gamma_\pm = \gamma'_\pm \gamma_c (1 \pm \beta_\pm \beta_c u), \quad (2.35)$$

where  $u$  is the cosine of the angle between the velocity of the electron (the positron) and the velocity of laboratory frame in center-of-momentum frame,  $\beta_\pm = \sqrt{1 - (1/\gamma'_\pm)^2}$

and  $\beta_c = \sqrt{1 - (1/\gamma_c)^2}$ .

## 2.5 Acceleration of particles in AGN jets

The observation of the non-thermal radiation from blazar jets indicates the existence of high energy particles in the emission region. The  $\gamma$ -rays from some AGN jets extend up to  $\sim 10$  TeV. This implies the presence of electrons with the Lorentz factors  $\gamma \gg 10^6$ . What is more, the high energy radiation is variable in very short timescales. The observed time variability of some flares is shorter than 10 min (e.g. Aharonian et al., 2007). All of this indicates that the efficient acceleration processes have to occur in the AGN jets. In general, three mechanisms are considered in terms of the particle acceleration in AGN jets: (i) stochastic acceleration by magnetic turbulence, (ii) diffusive shock acceleration and (iii) acceleration in magnetic reconnection.

### 2.5.1 Stochastic acceleration

The particle acceleration, as a result of collisions of a particle with randomly moving scattering centers, has been proposed by Fermi (1949). Originally, the mechanism has been applied to the acceleration of cosmic rays on the moving irregularities of the interstellar magnetic field. The energy of particles changes with every collision. The energy increases in the head-on collisions and decreases as a result of the tail-on collisions. Because the probability of head-on collisions is higher than the probability of tail-on collisions, the average energy of particles increases. The average energy gain in every collision,  $\Delta E$ , is proportional to the square of the characteristic velocity of the irregularities,  $V$ , i.e.

$$\left\langle \frac{\Delta E}{E} \right\rangle \propto \left( \frac{V}{c} \right)^2. \quad (2.36)$$

Because of the proportionality to the square of the velocity  $V$ , this mechanism is called *the second-order Fermi acceleration*. The model predicts a power-law form of the spectral distribution of the cosmic rays. This prediction agrees with the observations of the cosmic rays in the broad energy range.

In general, the particle distribution function in the second-order Fermi acceleration process can be described as a diffusion in the particle momentum space. The evolution of particles in the quasi-linear approximation is given by the Fokker-Planck equation (Schlickeiser, 2002). For the ultrarelativistic case, i.e.  $pc \simeq E$ , the Fokker-Planck equation takes the form

$$\frac{\partial n(E, t)}{\partial t} = \frac{\partial}{\partial E} \left[ D(E) \frac{\partial n(E, t)}{\partial E} \right] - \frac{\partial}{\partial E} \left[ \left( \frac{2D(E)}{E} + \dot{E}_{cool} \right) n(E, t) \right] - \frac{n(E, t)}{t_{esc}(E)} + Q(E, t), \quad (2.37)$$

where  $n(E, t)$  is the differential particle number density,  $D(E)$  is the diffusion coefficient,  $\dot{E}_{cool}$  is the energy loss rate,  $t_{esc}(E)$  is the characteristic escape time of particles and

$Q(E, t)$  describes injection rate of particles.

The steady-state particle spectra in the second-order Fermi acceleration take different shape depending on the forms of  $D(E)$ ,  $\dot{E}_{cool}$ ,  $t_{esc}$  and  $Q(E, t)$ . When particles do not escape from the acceleration region, their spectral distribution is approximately given by the modified relativistic Maxwellian function, i.e.  $n(E) \propto E^2 \exp[(-1/a) \times (-E/E_{eq})^a]$ , where  $E_{eq}$  is the equilibrium energy and the value of  $a$  depends on the type of magnetic turbulences and the cooling processes (Stawarz and Petrosian, 2008). Otherwise, the particles take the form of the relativistic Maxwellian modified by the power law function (Katarzyński et al., 2006; Stawarz and Petrosian, 2008). The second-order Fermi acceleration process was successfully applied as the acceleration mechanism of particles in AGN jets (Tramacere et al., 2011; Asano et al., 2014).

### 2.5.2 Diffusive shock acceleration

The acceleration on magnetic irregularities is possible also on the strong shock wave. This mechanism has been discovered independently by Axford et al. (1977); Krymskii (1977); Bell (1978); Blandford and Ostriker (1978). Such a process is much more efficient than stochastic acceleration process. In contrast to the stochastic acceleration, the average energy gain is linearly proportional to the characteristic velocity of the scattering centers, i.e.  $\Delta E/E \propto V/c$ . Because of that, the process is called *the first-order Fermi acceleration*.

The first-order Fermi acceleration occurs on the supersonic shocks, i.e.  $U \gg c_s$ , where  $U$  and  $c_s$  are the velocity of the shock propagation and the sound speed, respectively. The parameters of the plasma before and behind the shock can be found by solving the system of the conservation equations. In the case of the fully ionized gas, the velocity of the plasma behind the shock is  $V = (3/4)U$  (Longair, 2011). Then, in the reference frame of the plasma on one side, the magnetic irregularities on the other side always flow in direction of the shock. It means that particles always collide head-on with the irregularities on the other side of the shock. The particle spectrum in the first-order Fermi acceleration forms a power law. The spectral index depends on the compression ratio of the shock. For strong shocks, the spectral index is  $s \simeq 2$ .

The detailed physics of the diffusive shock acceleration is much more complicated than the simplified picture of the diffusive shock acceleration presented above. The more realistic model of first order-Fermi acceleration has to include the composition of the plasma, the modification of the shock properties by high energy particles, the role of the magnetic field and the relativistic effects (if  $U \sim c$ ).

The acceleration at relativistic shocks is especially important for physics of AGN jets due to the relativistic motion of outflows. The acceleration at relativistic shock has been firstly considered by Kirk and Schneider (1987). They found that the spectral index of accelerated particles is slightly larger than 2. This result has been confirmed in further works (e.g. Bednarz and Ostrowski, 1998).

The origin of the shocks in the parsec-scale AGN jets is a separate issue. One of the possibilities is the existence of the reconfinement shock in a jet (Sanders, 1983). The energy dissipation by the reconfinement shocks was studied for example by Nalewajko and Sikora (2009). The other, most popular, possibility assumes that the jet consists of a large number of shells moving with different, relativistic velocities (Rees, 1978). Inside the jet, shells collide each other due to their various velocities. The shocks are developed as a result of collisions of these shells. The shocked matter accelerates particles in the first-order Fermi acceleration. It should be noted that the radiation produced in the internal shock model comes from an extended part of a jet. It is a result of the interaction between many shells (Spada et al., 2001). Malzac (2013) finds that the dissipation profile along a jet in the internal shock model is inversely proportional to the distance from the jet base.

The mechanism similar to the diffusive shock acceleration may also occur in the jet with the radial gradient of the velocity. The particles are scattered by the magnetic inhomogeneities moving with different characteristic velocities which depend on the radial distance from the jet axis. Such a situation can appear between the jet and its surroundings or in case of the radially stratified jet (like in case of spine-sheath structure of the jet, where the fast spine is immersed in the slower outer layer). This acceleration mechanism has been studied by Stawarz and Ostrowski (2002) and Rieger and Duffy (2004).

### 2.5.3 Magnetic reconnection

Due to the high conductivity of plasma, the persistent electric fields does not occur in AGN jets. However, the electric field can be induced as a result of changing magnetic field. The process in which the energy of the magnetic field is converted into the other form of energy (including the kinetic energy of the relativistic particles) is called *the magnetic reconnection*. In contrast to the Fermi acceleration, the magnetic reconnection is efficient acceleration process in the highly magnetized environment, i.e. when the magnetization of plasma,  $\sigma$ , (defined as the ratio between the energy of the magnetic field and the enthalpy) is large.

In AGNs, a large part of the jet power ( $\sim 10\%$ ) is radiated. It indicates that the relativistic particles carry a large amount of the jet power. From the other side, the launching mechanism of jets, such as the Blandford-Znajek process (Blandford and Znajek, 1977), predicts that jets are dominated by the Poynting flux close to the black hole. Then, the magnetic reconnection gives the answer how the energy of magnetic field is dissipated. In the magnetic reconnection, even 50% of a jet energy can be converted to energy of non-thermal particles (Sironi et al., 2015).

The simulations of the magnetic reconnection show that the particle energy distribution forms the power law with the exponential cut-off. Their spectral index,  $s$ , depends on the magnetization of the plasma. For  $\sigma \gg 1$ , the spectral index asymptot-

ically reaches to  $s \simeq 1$  (Guo et al., 2014).

Due to the above features, the magnetic reconnection is used to model acceleration process in AGN jets. For example, Giannios et al. (2009) assume that the extremely short variability of blazars is caused by the mini-jets produced in the magnetic reconnection events (see also Nalewajko et al., 2011). The acceleration of particles in the magnetic reconnection process may occur also in the magnetic field of the accretion disk and the disk corona producing extremely short  $\gamma$ -ray flares (e.g. Bednarek, 1997).

# Chapter 3

## Modeling of the Non-Thermal Emission from AGN Jets

The observed non-thermal radiation from AGN jets gives a unique insight into the jet physics. The general properties of jets can be constrained using the physical arguments. The parameters of the emission region can be also found considering the spectral and the temporal behaviors of the jet radiation. However, more accurate estimations of the processes and of the parameters occurring in the jet require the application of more sophisticated methods such as the emission models of the jet.

In this Chapter, I present the methods for estimation of the basic parameters of the jet (or more accurately, the emission region). Later, I describe briefly the proposed up to now emission models of the AGN jets. I divide the described models depending on the type of emitting particles.

### 3.1 Estimation of the basic parameters of AGN jets

A very important parameter for the physics of AGN jets is the mass of the super-massive black hole (SMBH) powering the jet. The mass of the black hole can be determined using a number of methods. In the case of BL Lacs, the most important methods are inferring the black hole mass from the correlation with the galaxy bulge mass (Kormendy and Richstone, 1995) and from the correlation with the stellar velocity dispersion of the stars in a parent galaxy (Gebhardt et al., 2000; Ferrarese and Merritt, 2000). Application of the second method gives masses of black holes in BL Lacs typically in range  $10^8 - 10^9 M_{\odot}$ , where  $M_{\odot} = 1.99 \times 10^{33}$  g is the mass of the Sun. This result agrees with the masses of black holes in radio galaxies obtained with both methods (Bettoni et al., 2003). In the case of flat-spectrum radio quasars (FSRQ), the broad emission lines and the radiation emitted by an accretion disk can be used to estimate the black hole mass. For example, it can be done with the reverberation mapping technique (Peterson, 1993). The mass is estimated from the virial relationship between

the radius of the BLR,  $R_{BLR}$ , the velocity dispersion of the broad line,  $\Delta V$ , and the mass of the central object,  $M_{BH}$ , i.e.

$$M_{BH} \sim \frac{R_{BLR}\Delta V^2}{G}, \quad (3.1)$$

where  $G$  is the gravitational constant. More about different methods of black hole mass estimations can be found in Ferrarese and Ford (2005).

The black hole masses in AGNs are typically in the range from  $10^6 M_\odot$  to  $10^{10} M_\odot$ . The mass of SMBH determines the size of the central engine and the inner jet. The characteristic spatial-scale for the specific black hole is the Schwarzschild radius, i.e. the radius of the event horizon of a non-spinning black hole,

$$R_{Sch} = \frac{2GM_{BH}}{c^2} = 2.95 \times 10^5 \frac{M_{BH}}{M_\odot} = 2.95 \times 10^{13} M_8 \text{ cm}, \quad (3.2)$$

where  $M_{BH} = 10^8 M_8 M_\odot$ . The convenient way to express distances in AGNs is to scale them with  $R_{Sch}$ .

It is expected that the minimum radius of the emission region in AGN jets should be of the order of the Schwarzschild radius. The radius of the emission region,  $R_{em}$  can be also estimated with the causality argument. The observed variability time scale of the radiation from an AGN jet,  $t_{var}$ , limits the size of emission region in following way:

$$R_{em} < ct_{var}D_j, \quad (3.3)$$

where  $D_j$  is the Doppler factor of the emission region.

The jet power,  $P_{jet}$ , is limited by the Eddington luminosity. For this luminosity, the gravity of the central object with the mass  $M_{BH}$  balances the radiation pressure acting on a fully ionized hydrogen. The Eddington luminosity is given by

$$L_{Edd} = \frac{4\pi GM_{BH}m_p c}{\sigma_T} \simeq 1.3 \times 10^{46} M_8 \text{ erg/s}, \quad (3.4)$$

where  $m_p$  is the proton mass. The expected jet power in AGNs for emission over a long time scale has to be below this value, i.e.  $P_{jet} = \xi_{jet} L_{Edd}$ , where  $\xi_{jet} < 1$ . Because the jet power is transported from the vicinity of a black hole up to the distance of kiloparsecs, then this power cannot be carried by relativistic  $e^\pm$  pairs which lose energy relatively fast in the jet environment. The role of cold  $e^\pm$  pairs seems also to be insignificant (Sikora et al., 2005). Hence, the jet power consists mainly of the Poynting flux,  $P_B$ , and power of protons (cold or relativistic),  $P_p$ , i.e.

$$P_{jet} \simeq P_B + P_p = (1 + \sigma_M) \times P_p = \frac{1 + \sigma_M}{\sigma_M} P_B, \quad (3.5)$$

where  $\sigma_M = P_B/P_p$  is the magnetization parameter (Sikora et al., 2013). The magnetization may change with time and the distance from the jet base. However, at this point, I assume that the ratio between the Poynting flux and the kinetic energy is constant.

The Poynting flux is then  $P_B = \xi_{jet}\sigma_M L_{Edd}/(1 + \sigma_M)$ . On the other hand, the Poynting flux in the jet is related to the energy density of the magnetic field in the jet frame,  $u'_B = B^2/8\pi$ , and the jet cross section,  $\pi R_j^2$ ,

$$P_B = \Gamma_j^2 \pi R_j^2 c \beta_j B^2 / 8\pi, \quad (3.6)$$

where  $\Gamma_j$  is the bulk Lorentz factor of the jet,  $c\beta_j$  is the plasma velocity in the jet and  $B$  is the magnetic field strength.

Moreover, I assume that the jet has a conical shape with the half-opening angle  $\phi = \rho/\Gamma_j$ . The perpendicular dimension of the jet at the distance  $z$  from the black hole is given by

$$R_j(z) \simeq \frac{\rho}{\Gamma_j} z = 2.95 \times 10^{13} \times \frac{\rho M_8 z_{Sch}}{\Gamma_j} \text{ cm}, \quad (3.7)$$

where  $z_{Sch}$  is the distance from the black hole in the units of the Schwarzschild radius. The parameter  $\rho$ , describing the transverse expansion of the jet, has been estimated on 0.2–0.3 based on the radio observations of the parsec-scale jets (see Section 2.2).

The value of the magnetic field at some distance,  $z$ , can be found comparing Eq. 3.5 and Eq. 3.6, i.e.

$$B \simeq 6.3 \times 10^4 \times \left( \frac{\xi_{jet}\sigma_M}{1 + \sigma_M} \right)^{1/2} \times M_8^{-1/2} \times \rho^{-1} \times z_{Sch}^{-1} \text{ G}. \quad (3.8)$$

Assuming that  $\sigma_M \sim 1$ , such a result roughly agrees with the value of the magnetic field strengths in the jets found by O’Sullivan and Gabuzda (2009) using core-shift effects in AGN jets.

## 3.2 Estimation of parameters from spectral properties of blazar jets

The broad-band spectra of blazars can be used to estimate the physical parameters of the emission region. In general, the broad-band spectral energy distributions (SEDs) consist of two humps, where the first hump is produced by relativistic electrons in the synchrotron process. The second hump is produced in the IC process, in terms of the most popular leptonic scenario. The number of the free parameters can be limited from spectral properties of these humps. The constraints of the parameters can be found by assuming that (i) the radiation is produced by a small part of the jet (blob), (ii) the conditions in the blob are homogeneous, (iii) leptons and photons are isotropic and (iv) the synchrotron self-Compton (SSC) process is dominant process for production of  $\gamma$ -rays.

In the SSC process (in Thomson regime), the ratio between the luminosities of both humps (the synchrotron,  $L_{syn}$ , and the IC,  $L_{SSC}$ ) is proportional to the energy densities

of the magnetic field ( $u'_B = B^2/8\pi$ ) and the synchrotron radiation ( $u'_{rad}$ ) in the frame co-moving with the blob, i.e.

$$\frac{L_{syn}}{L_{SSC}} = \frac{u'_{rad}}{u'_B} = \frac{L_{syn}}{4\pi R_{em}^2 c D_j^4 u'_B}, \quad (3.9)$$

where  $u_{rad} = L_{syn}/4\pi R_{em}^2 c D_j^4$ . From Eq. 3.9 and Eq. 3.3, one can find relation between the Doppler factor and the strength of the magnetic field,

$$BD_j^3 = \frac{\sqrt{2}L_{syn}}{c^{3/2}t_{var}L_{SSC}^{1/2}}. \quad (3.10)$$

The relation between  $B$  and  $D_j$  can be also determined by the comparison of the location of the peaks in the  $\nu$ -versus- $\nu F_\nu$  plot. In the SSC model, the synchrotron and the IC peaks are produced by electrons with these same energies,  $E_{br} = \gamma_{br}m_e c^2$ , where  $\gamma_{br}$  is the Lorentz factor of particles producing mainly the radiation of the peaks. The characteristic energy of the synchrotron photons in blob frame,  $\epsilon'_{syn} = h\nu_{syn}$ , is given by Eq. 2.12. The characteristic energy of the  $\gamma$ -ray photons, produced in the IC scattering, is  $\epsilon'_{SSC} = (4/3) \times \gamma_{br}^2 \epsilon'_{syn}$  (e.g. Blumenthal and Gould, 1970). The relation between  $B$  and  $D_j$  can be found by the comparison of these two formulas,

$$BD_j = \frac{16\pi m_e c}{3eh} \frac{\epsilon_{syn}^2}{\epsilon_{SSC}}, \quad (3.11)$$

where  $\epsilon_{syn} = D_j \epsilon'_{syn}$  and  $\epsilon_{SSC} = D_j \epsilon'_{SSC}$ .

The value of  $B$  and  $D_j$  can be found by solving the system of Eq. 3.10 and Eq. 3.11. However, in reality, there are a number of problems with such a method. The luminosities of the humps and the locations of peaks in the blazar spectra change over time. Blazars are characterized by significant variability thus several instruments have to observe the source in the same time. Furthermore, only a part of the energy range of the electromagnetic spectrum is observed by the modern telescopes. Then, the precise determination of energy in which the peaks appear in the spectrum is not always possible.

### 3.3 Leptonic models of emission from AGN jets

The most common emission model for AGN jets assumes that the radiation from the internal jet in AGNs is produced by relativistic leptons (electrons and positrons). The leptonic origin of the jet radiation is supported by very inefficient hadronic processes (Sikora, 2011). Many different leptonic models have been developed. They assume different acceleration processes and different degree of simplification of the jet physics. Here, I divide the leptonic models in terms of the features of emission region. I distinguish:

- The SSC one-zone models, where radiation is produced in a single region. The emission region is characterized by constant and homogeneous parameters. The IC radiation is produced in SSC process.
- The external Compton models, where also one emission region occurs but the scattered radiation comes from the external sources (e.g. an accretion disk, BLR, dusty torus).
- The multi-component models, where radiation is produced in two or more emission regions. The emission regions can interact with each other or be independent. Typically, every emission region is characterized by different but constant parameters.
- The models of the collision of the jet with compact objects. In such models, the emission region is the place of interaction between the jet (or a dense blob) with compact objects, such as star or a cloud.
- The inhomogeneous models, where the parameters of the emission region change with distance in a smooth way.

### 3.3.1 One-zone, homogeneous SSC models of AGN jets

The SSC, one-zone model form the simplest case of the emission models. Many variants of this model are developed depending on the adopted assumptions. Typically, this model bases on the following assumptions:

- the majority of radiation comes from the compact emission region with spherical shape (in the frame co-moving with emission region), called *a blob*;
- the parameters in the blob are homogeneous and persistent;
- the blob is filled by relativistic electrons which are distributed isotropically (in the blob frame);
- the magnetic field in the blob,  $B$ , is randomly oriented;
- $\gamma$ -rays are produced in the SSC process on the isotropically distributed synchrotron photons;
- the blob size is estimated from the variability time-scale of the observed emission (according to Eq. 3.3).

Due to a small number of the free parameters, the one-zone model is commonly used to fit the jet emission from blazars (see e.g. Abdo et al., 2011a,b). This model is also used to model the emission from radio galaxies (e.g. Abdo et al., 2009a,b; Banasiński and Bednarek, 2014). The number of the free parameters can be limited by

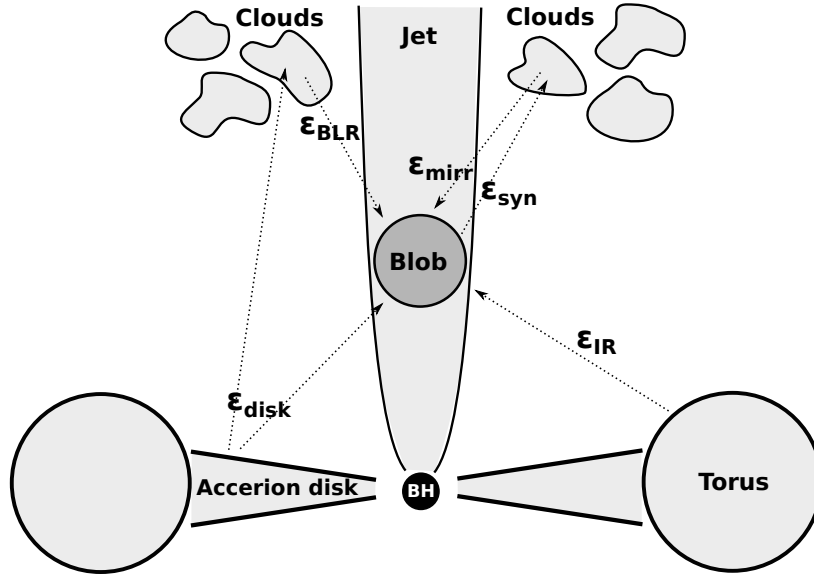


Figure 3.1: Schematic diagram (not to scale) illustrating the production of IC  $\gamma$ -rays in the AGN jet in terms of the different external Compton models: (i) Comptonization of photons from the accretion disk ( $\epsilon_{disk}$ ), (ii) Comptonization of photons from the dusty torus ( $\epsilon_{IR}$ ), (iii) Comptonization of photons from the broad line region ( $\epsilon_{BLR}$ ) and (iv) Comptonization of the synchrotron photons from the blob ( $\epsilon_{syn}$ ) reprocessed by the clouds in the BLR ( $\epsilon_{mirr}$ ).

the observed spectral properties (see Chapter 3.2), the condition of  $\gamma$ -ray transparency of the emission region and the comparison of different time scales (e.g. Maraschi et al., 1992; Bednarek and Protheroe, 1997b; Tavecchio et al., 1998; Bednarek and Protheroe, 1999a).

### 3.3.2 External Compton models of AGN jets

The parsec-scale jet in AGNs is surrounded by the external sources of low energy photons, in particular an accretion disk, a broad-line region (BLR) and a dusty torus. Such photons can make a significant contribution to the total density of radiation in the parsec-scale jet. Furthermore, the external radiation, seen by the emission region (blob), is significantly modified due to the relativistic effects. Because of that, the possible scattering of the external photons is considered as the process responsible for the  $\gamma$ -ray emission in some blazars. It is believed that the Comptonization of the external photons produces the majority of radiation in flat-spectrum radio quasars (FSRQ). In these objects, the accretion disk is especially luminous and the broad lines are strong.

Many models are created depending on the main source of the external photons. The model in which  $\gamma$ -rays are produced by scattering of the accretion disk radiation has been proposed by Dermer and Schlickeiser (1993). The Comptonization of photons from the broad emission line region has been investigated in Sikora et al. (1994). Also, the dusty torus has been considered as the source of the photon field for relativistic

electrons in blazars (Błażejowski et al., 2000).

Another model in which the  $\gamma$ -rays are produced by scattering of external photons is called the mirror Compton model (Ghisellini and Madau, 1996; Bednarek, 1998). In such a model, the relativistic electrons in the blob produce the synchrotron radiation. This radiation is reprocessed back to the blob by the clouds from the broad line region. Then, the reprocessed radiation is Comptonized by the electrons from the blob.

### 3.3.3 Interaction of AGN jets with compact objects

The central engine in AGNs is surrounded by clouds, stars, and globular clusters. These objects, from time to time, enter into an AGN jet. During such an event, the relativistic plasma interacts with the compact object. If the collision between the star and the plasma in a jet happens close to the jet base, the envelope of the star may be blown out. However, in such scenario, the radiation processes of hadrons are much more efficient (e.g. Barkov et al., 2010).

At a greater distance from the jet base, the jet pressure can be balanced by the pressure of the stellar wind. As a result, the shocks appear around the compact object. On these shocks, electrons can be accelerated to high energies. These electrons produce  $\gamma$ -rays in the Compton scattering of stellar photons. Such a scenario has been investigated by Bednarek and Protheroe (1997a); Araudo et al. (2013); Bednarek and Banasiński (2015); Wykes et al. (2015).

When the jet pressure is small enough, clouds can penetrate the jet avoiding destruction. This leads to the formation of the shocks between the jet plasma and clouds where particles can be efficiently accelerated. Such an interaction between the cloud and the jet plasma in terms of the leptonic processes has been studied by Araudo et al. (2010).

The interaction of a relativistic blob with the radiation from a star passing a jet has been also studied in Banasiński et al. (2016). In this case, the relativistic electrons already present in the jet scatter radiation from the massive star immersed in the jet volume. In such a case, the short  $\gamma$ -ray flares can be produced, without the counterpart in the synchrotron radiation (so-called orphan flares).

### 3.3.4 Multi-component models of AGN jets

Many problems are encountered when the emission from blazars is described in terms of the one-zone models. Firstly, the one-zone models predict a strict correlation between all energy ranges. However, some flares occur only in a part of the electromagnetic spectrum. One of the most surprising such events are the “orphan” flares in the  $\gamma$ -ray range (e.g. Krawczynski et al., 2004). Secondly, the Doppler factor of the emission region, determined by fitting spectra with one-zone models, is of the order of 15. While the radio observations suggest much smaller Doppler factor (e.g. Piner and Edwards,

2018). Because of that, more complex models have to be developed.

The simplest multi-component model is the scenario in which the radiation from the blazar is produced by two compact blobs. When the blobs are independent, the model comes down to two one-zone models, in which the total emission is the sum of the emission radiated by specific blobs. This approach has been used in Tavecchio et al. (2011); Barres de Almeida et al. (2014); Shukla et al. (2015).

Another version of the two-component model has been also developed by Katarzyński et al. (2001). In this model, the high energy part of the spectrum is produced by a compact blob. The low energy part is emitted by the inhomogeneous conical jet. Such a model, commonly called as *the blob in jet* model, has been also used to describe the spectra of the low synchrotron peaked blazar, AP Librae (Hervet et al., 2015).

The multi-component model of the jet emission has been also proposed by Giannios et al. (2009). They propose the scenario, in which small jets are created in the magnetic reconnection process within an AGN jet. This *jets in a jet* model provide the emission region moving with bulk Lorentz factor order of 100 in the observer's frame (see also Bednarek et al., 1996).

The observations of the limb-brightening in AGN jets suggest the stratified structure of jets. Based on these observations and the relatively slow motion of the jets observed in TeV blazars, Ghisellini et al. (2005) propose *the spine-sheath* model of the emission from AGN jets. In such a model, the radiation is produced in two regions, where each region is characterized by the different parameters, especially by the different bulk Lorentz factors. The important aspect of this model is an interrelation between the regions. The radiation from the first emission region is amplified by relativistic effects in the frame of the second emission region. The spine-sheath model has been also applied to the FSRQs (Sikora et al., 2016).

### 3.3.5 Inhomogeneous models of AGN jets

The parameters in the emission region in a jet can change over time and location. When the parameters change relatively smoothly, then the model is inhomogeneous. Some of the models mentioned above can be included to the group of inhomogeneous models, like the blob-in-a-jet model, where the parameters of the jet component change over the distance from the jet base. Blandford and Königl (1979) have shown that the flux of the radio emission from the conical inhomogeneous jet is flat, provided that the magnetic field decreases linearly with distance from the jet base and the electron energy density is in the equipartition with the magnetic field energy density.

Some of the inhomogeneous models focus on the thin shells propagating along the jet (Asano et al., 2014). In other inhomogeneous models, the emission comes from a relatively large part of the jet (Ghisellini et al., 1985; Boutelier et al., 2008; Potter and Cotter, 2012). However, in every case, the number of the free parameters of the models is much larger than in the case of one-zone, homogeneous model, which is the

disadvantage of these models.

### 3.4 Hadron models of AGN jets

It is clear that AGN jets consist not only of electrons and positrons, but also heavier particles like protons and ions. Then, it is possible that a part of the radiation is emitted by hadrons. The hadronic models of AGN jets base on this assumption.

Hadronic models are motivated by the existence of the ultra-high energy (UHE) cosmic rays, with energy above  $10^{19}$  eV. Jets in AGNs are considered as a site of the UHE cosmic ray acceleration. Hadrons with such high energies can interact with photons, a magnetic field or protons inside a jet. As a result, very high energy  $\gamma$ -rays are emitted.

One of the approaches to the  $\gamma$ -ray production in AGN jets is *the proton initiated cascade* (PIC) model (Mannheim et al., 1991). Energetic hadrons interact with the low energy synchrotron photons inside the jet and produce secondary particles in the Bethe-Heitler pair production process and the photomeson production process (Mannheim and Biermann, 1992; Mannheim, 1993). Mücke and Protheroe (2001) propose the synchrotron proton blazar model, which takes into account both, the synchrotron process of charged particles and the interaction of protons with photons produced in the jet.

In a similar way to the leptonic models, the protons can interact with photons produced in different places. For example, protons can collide with photons from the accretion disk (Protheroe, 1997; Bednarek and Protheroe, 1999b) or with photons from the broad-line region (Atoyan and Dermer, 2003). At last, according to mirror Compton models, the photons from the jet can be reprocessed by clouds in BLR and reflected into the jet creating the target for hadrons (Böttcher, 2005).

The high energy photons can be produced by UHE protons in the synchrotron process. Such a model requires protons with energy  $\sim 10^{19}$  eV and the magnetic fields with relatively large strength,  $B \sim 100$  G. Such a model has been considered, for example, by Aharonian (2000).

Relativistic protons can also interact with the matter in AGN. Then, the required energy of protons is much smaller. Such a model has been proposed by Bednarek (1993). In this model, the relativistic protons collide with matter from the funnel of an accretion disk. Relativistic protons can also interact with the matter of the clouds entering the jet (Dar and Laor, 1997; Beall and Bednarek, 1999). Another scenario has been proposed by Barkov et al. (2010). They considered a scenario, in which a red giant pass the AGN jet close to the jet base (see also Bosch-Ramon et al., 2012; Barkov et al., 2012). In this model, the envelope of the red giant is blown by the jet. The protons are accelerated on magnetic perturbations and interact with the matter from the star. The collision of the star with the jet occurs close to the jet base, where the magnetic field is relatively strong. Because of that, it is possible that the HE radiation can be

also produced in the synchrotron process of protons.

# Chapter 4

## The Stationary Non-Local Inhomogeneous Jet Model

The flaring emission is usually interpreted in terms of the homogeneous synchrotron self-Compton (SSC) model. This model assumes that a compact emission region (blob), with the fixed parameters, moves along the jet with a large Lorentz factor. Such a simple homogeneous model can naturally explain the short time scale flares. However, the long-time scale, persistent emission cannot originate in the single, fast-moving blob. It is expected that the blob expands with the distance along the jet and the basic parameters responsible for radiation processes should change significantly. For the jet pointed at the observer, the distance traveled by the blob can be estimated with  $\Delta z = 2\Gamma_j^2 c \Delta t$ , where  $\Delta t$  is the observed time scale,  $\Gamma_j$  is the Lorentz factor of the blob and  $c$  is the speed of light. For the typical Lorentz factor of blazars ( $\Gamma_j \sim 10$ ) and the time scale of the order of a month ( $\Delta t = 2.6 \times 10^6$  s), the distance scale traveled by the emission region is larger than 5 pc. Therefore, parameters of the compact blob should change significantly.

For example, the constant emission with the time scale greater than a month was observed from two best investigated up to now objects, Mrk 421 (Abdo et al., 2011b; Aleksić et al., 2015a) and Mrk 501 (Abdo et al., 2011a; Aleksić et al., 2015b). During the recent multiwavelength campaigns, both objects are observed in the low activity state. For the most of time, they emit low level, persistent emission. These objects have been also observed with the High Altitude Water Cherenkov (HAWC) observatory, which affirms the presence of the persistent VHE  $\gamma$ -ray emission from both sources (Albert et al., 2017). With the development of the observation techniques, it is expected that more objects will be detected in a quiescent and persistent state. As a result, the models describing the low level and constant emission will be required.

In this Chapter, I examine the scenario in which the majority of radiation is produced in the extended (parsec-scale) part of a jet. To describe this emission I develop the model of the inhomogeneous and stationary jet. In such a model, the basic parameters of the jet, like the magnetic field strength and the spectrum of electrons, will

change significantly along the jet. The radiation will come from the whole considered part of the jet. Due to the elongated shape of the jet, the radiation produced by the jet will be significantly anisotropic (also in the co-moving frame of the jet). Therefore, the IC scattering of non-local photons has to be taken into account in the calculation of the produced  $\gamma$ -ray radiation.

In order to simulate the emission from the stationary and inhomogeneous jet, I develop the numerical emission model. The shape of the jet is simplified to a truncated cone. I assume that the plasma inside the jet moves with a constant velocity which corresponds to the constant bulk Lorentz factor of the jet,  $\Gamma_j$ . The basic parameters of the jet are normalized at the jet base. They change with the distance from the jet base,  $z$ . I presume that the radiation is produced by the relativistic leptons (electrons and positrons). The contribution to the radiation from other particles (such as relativistic protons) is neglected. The leptons are accelerated in a large part of the jet. Their distribution evolves along the jet. The evolution of electrons is described by the kinetic equation (e.g. Kardashev, 1962). In the model, I take into account the synchrotron emission, the inverse Compton scattering (in the Thomson and the Klein-Nishina regimes), the synchrotron self-absorption and the absorption on the extragalactic background light (EBL). Moreover, the model takes into account the anisotropy of the radiation produced in the jet due to its conical geometry. The radiation in a specific region in the jet depends on the radiation produced self-consistently in the whole volume of the jet.

The model is examined for a wide range of parameters. I show how the multi-wavelength spectra depend on the parameters describing the geometry of the jet, the magnetic field and the electron acceleration process. In the last section, I interpret the spectra of the nearby BL Lac object, Mrk 421 in terms of the considered model.

## 4.1 Theoretical description of the model

I consider a part of the jet with the base located at  $z_0 = 0$ . Note that the distance between the jet base and the super massive black hole (SMBH) is not determined. The calculations are performed to the maximum distance  $z_{max}$  along the jet (see: Fig. 4.1). It is assumed that the acceleration of leptons occurs between distances  $z_0$  and  $z_{end} = 0.1 \times z_{max}$ . The radius of the jet at the base is  $R_0$ . The jet has a conical shape, which is characterized by the half-opening angle (the angle between the jet axis and the jet edge),  $\phi$ . Hence, the radius of the jet at the specific distance,  $z$ , for the small opening angle is

$$R_{obs}(z) = R_0 + z \tan \phi \simeq R_0 + z\phi. \quad (4.1)$$

A more convenient way is to consider the processes occurring in the jet in the plasma rest frame. In this frame, the distribution of electrons is isotropic. It is assumed that the motion of the plasma in the jet is characterized by the constant Lorentz factor  $\Gamma_j$ .

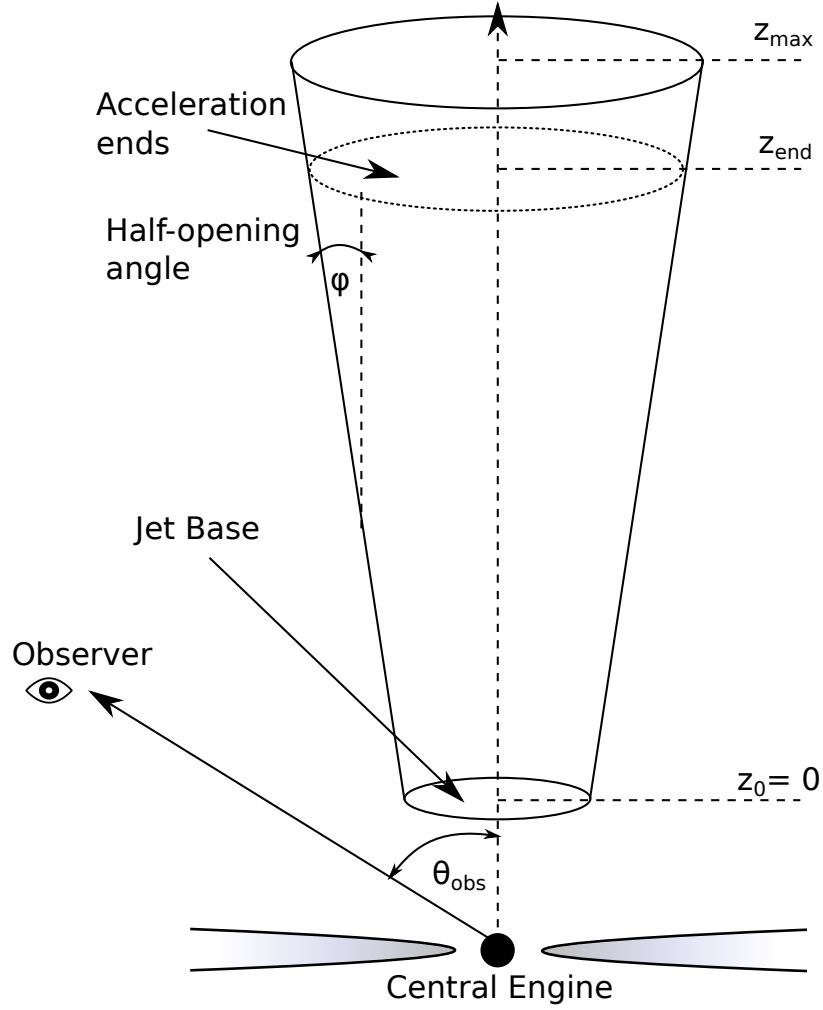


Figure 4.1: Schematic picture of the jet in the observer rest frame (not to scale). The jet base, with the radius  $R_0$ , is located at the distance  $z_0$ . The acceleration begins at the jet base and continues up to  $z_{end}$ . The jet is considered up to  $z_{max} = 10z_{end}$ . The half-opening angle of the jet is  $\phi$  and the observation angle is  $\theta_{obs}$ . The distance between the jet base and the black hole (central engine) is not specified in the model. All quantities characterizing the jet are normalized to the jet base.

Then, the cross-section of the jet in the plasma rest frame is described by

$$R(t') = R_0 + \phi \Gamma_j \beta_j c t' = R_0 + \rho \beta_j c t' \quad (4.2)$$

where  $\rho$  is the coefficient of the transverse expansion,  $\beta_j$  is the speed of the plasma in the jet in units of the speed of light,  $c$ , and  $t' = z/\beta_j c \Gamma_j$  is the time in the plasma rest frame. Note that in the plasma rest frame the distance to the jet base changes with time according to  $z' = \beta_j c t'$ .

I determine the strength of the magnetic field in the plasma rest frame as

$$B(t') = B_0 \left( \frac{R_0}{R(t')} \right)^b, \quad (4.3)$$

where  $B_0$  is the magnetic field strength at the jet base and  $b$  is the index which describes the magnetic field profile. For  $b = 1$ , the magnetic field is dominated by the toroidal component. When the parallel component of the magnetic field dominates, then  $b = 2$ , i.e.  $B \propto (R_0/R(t'))^2$ .

The relativistic electrons are injected in the jet continuously from the distance  $z_0$  up to  $z_{end}$ . Injection is described by a function  $Q'_{inj} \equiv dN/dz'dt'd\gamma$ , where the energy of the electron in the plasma rest frame is  $E'_e = \gamma m_e c^2$  and  $m_e$  is the electron mass <sup>1</sup>. I assume that  $Q_{inj}(\gamma, t')$  has a power law form with an exponential cutoff,

$$Q_{inj}(\gamma, t') = Q(t') \gamma^{-s} e^{-\gamma/\gamma_{max}(t')}, \quad (4.4)$$

where  $\gamma_{max}(t')$  is the maximum Lorentz factor of electrons and

$$Q(t') = Q_0 \times \left( \frac{R_0}{R(t')} \right)^q, \quad (4.5)$$

is injection profile. If electrons are injected continuously within the jet with similar power in every part of the jet, then  $q = 0$ . If the power in electrons injected to the jet is proportional to the energy density of the toroidal magnetic field, then  $q = 2$ .  $Q_0$  is obtained from the normalization of the total power injected in the relativistic electrons  $L'_{inj}$ , i.e.

$$L'_{inj} = m_e c^2 \int \int Q_{inj}(\gamma, t') \gamma dz' d\gamma. \quad (4.6)$$

$L'_{inj}$  is the free parameter of the model.

The maximum Lorentz factor of the injected electrons,  $\gamma_{max}$ , is obtained from the comparison of their acceleration time scale,  $t_{acc}$ , with their total cooling time scale,  $t_{cool}$ , i.e.

$$t_{acc}(\gamma) = t_{cool}(\gamma), \quad (4.7)$$

where the acceleration time scale is parameterized by the acceleration coefficient  $\eta$ , i.e.  $t_{acc} = R_L/\eta c$  and  $R_L$  is Larmor radius of electrons. The total cooling time scale is given by the energy loss rate,  $\tau_{cool} = -\gamma/(d\gamma_{tot}/dt')$ , where

$$\frac{d\gamma_{tot}}{dt'} = \frac{d\gamma_{syn}}{dt'} + \frac{d\gamma_{ad}}{dt'} + \frac{d\gamma_{IC}}{dt'}. \quad (4.8)$$

$d\gamma_{syn}/dt'$ ,  $d\gamma_{ad}/dt'$ ,  $d\gamma_{IC}/dt'$  are the synchrotron, the adiabatic and the inverse Compton (IC) energy loss rates, respectively. The IC cooling rate is calculated not only in the Thomson regime but also in the Klein-Nishina regime. In the expanding jet, the adiabatic energy loss rate should be taken into account (see Appendix A in Zdziarski et al., 2014). In the case of the jet with the shape of the truncated cone given by Eq. 4.2, the adiabatic cooling rate is

$$\frac{d\gamma_{ad}}{dt'} = \frac{2}{3}(\gamma - 1) \frac{\rho \beta_j c}{R_0 + \rho \beta_j c t'}. \quad (4.9)$$

---

<sup>1</sup>I use primes to denote quantities in the plasma rest frame. However, electrons are considered always in the plasma rest frame. Then, for the sake of formulas clarity, the Lorentz factor of electrons in the plasma rest frame,  $\gamma$ , appears without the prime sign.

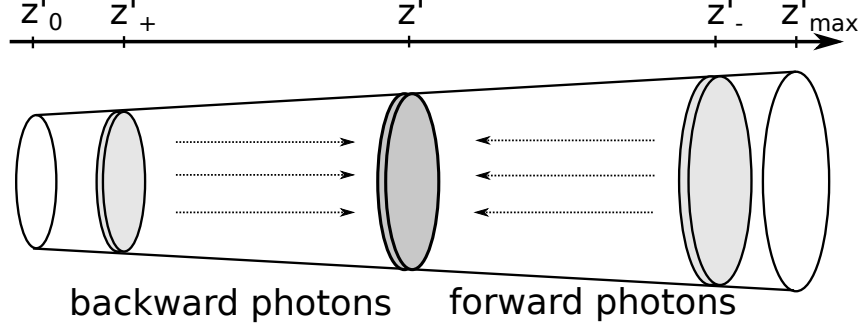


Figure 4.2: Schematic view of photons propagating in the jet, observed from the slab located at  $z'$ . The photon field at the distance  $z'$  consists of backward photons, from the regions placed at the distance  $z'_+$  (between  $z'_0$  up to  $z'$ ), and forward photons, from regions at the distance  $z'_-$  (between  $z'$  up to  $z'_{max}$ ).

I assume that  $t_{cool}$  is much shorter than the escape time scale of electrons from the emission region. Then, the differential spectrum of electrons in a thin slab with the thickness  $dz'$ ,  $N_e(\gamma, t')$  [electrons  $\text{cm}^{-3}$ ], evolves in time only as a result of the cooling processes and the rate of injection of fresh electrons into the jet. In this case, the spectrum of electrons is described by the kinetic equation with the following form

$$\frac{\partial N'_e(\gamma, t')}{\partial t'} = \frac{\partial}{\partial \gamma} \left( \frac{d\gamma_{tot}}{dt'} N'_e(\gamma, t') \right) + Q_{inj}(\gamma, t'). \quad (4.10)$$

The local density of photons,  $n'_{ph}$ , at the time  $t'$  depends on the conditions in the whole jet. Because of that, I solve the radiation transfer equation in order to calculate  $n'_{ph}$ . For simplicity, I assume that photons from the other parts of the jet are mono-directional. The directions of photons produced closer to the jet base are parallel to the jet axis. I call them the backward photons and represent by subscript “+”. The direction of the photons produced above the considered layer at  $z'$  is opposite to the direction of the jet axis. These photons are called as the forward photons and they are represented by “-”. The schematic representation of the geometrical situation allowing to understand the method of calculations of the local density of photons is presented in Fig. 4.2. The local density of photons in the slab at distance  $z' = \beta_j ct'$  from the jet base is composed of the forward and the backward photons. The backward photons are produced in a part of the jet located between  $z'_0$  and  $z'$ . The forward photons, which direction is opposite to the jet axis, are produced above the distance  $z'$ , up to  $z'_{max}$ . The local density of photons in the slab at the distance  $z'$  is calculated with the following formulas:

$$n'_-(\epsilon; z') = \frac{1}{c\epsilon} \int_{z'}^{z'_{max}} j'(\epsilon, \Omega; z_-) \exp(-\tau_{SSA}) \Delta\Omega dz_-, \quad (4.11)$$

$$n'_+(\epsilon; z') = \frac{1}{c\epsilon} \int_{z_0}^{z'} j'(\epsilon, \Omega; z_+) \exp(-\tau_{SSA}) \Delta\Omega dz_+, \quad (4.12)$$

where  $j(\epsilon, \Omega; z_{\pm})$  (in units of [ $\text{erg cm}^{-3} \text{s}^{-1} \text{sterad}^{-1} \text{GeV}^{-1}$ ]) is the synchrotron emissivity at the distance  $z_{\pm}$  and  $\tau_{SSA}$  is the optical depth of the self-synchrotron absorption

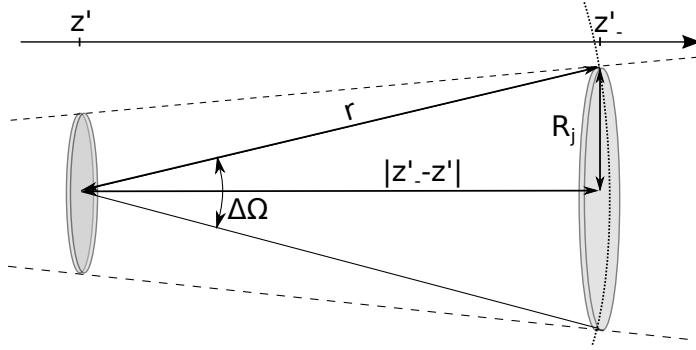


Figure 4.3: The method of the estimation of the solid angle,  $\Delta\Omega$ , between two slabs. The slabs are located at  $z'$  and  $z'_-$ . The distance between the slabs is  $|z'_- - z'|$ . The solid angle,  $\Delta\Omega$ , is estimated as the surface of the spherical cap of the sphere with radius  $r$  with height of the cap,  $h = r - |z'_- - z'|$ , divided by the surface of this sphere.

(SSA). The solid angle at which photons emitted from a slab at  $z'_\pm$  reaches a slab at  $z'$  is estimated from

$$\Delta\Omega(z', z'_\pm) = \frac{2\pi r h}{r^2} = 2\pi \left(1 - \frac{|(z'_\pm - z')|}{r}\right), \quad (4.13)$$

where  $2\pi r h$  is the area of the spherical cap and  $h = r - |(z'_\pm - z')|$  is the height of the spherical cap. The distances  $r$  is expressed by  $r = [(z'_\pm - z')^2 + R_j^2]^{1/2}$  (see Fig. 4.3). The method of calculation of  $\Delta\Omega$  for two slabs is shown in Fig. 4.3. For this approximation, almost a half of the photons produced in the slab at  $z'_\pm$  contributes to the local density of photons in the slab at  $z'$  when the distance between slabs is very small. In the case of very distant layers only small fraction of photons produced at  $z'_\pm$  reaches the slab at  $z'$ . Such an approximation is reasonable for the quite extended shape of the jet.

The electrons are isotropic in the specific slab. However, the radiation field is strongly isotropic. Then, the formula for the IC scattering of directed photon beam on the isotropically distributed electrons must be used (see e.g. Aharonian and Atoyan, 1981). Because the cross-section for the Compton scattering is large for a small scattering angle (especially in the Klein-Nishina regime), the IC radiation is produced efficiently at a very small angle to the jet axis, for the scattering of the forward radiation, or relatively large angle to the jet axis, for the backward radiation. These geometric effects are described in details in the Section 4.4.1.

## 4.2 The steady spectrum of electrons and local density of photons in the non-local jet model

In the inhomogeneous jet, the local conditions change with the distance from the jet base. According to Eq. 4.10, in order to obtain the differential spectrum of electrons

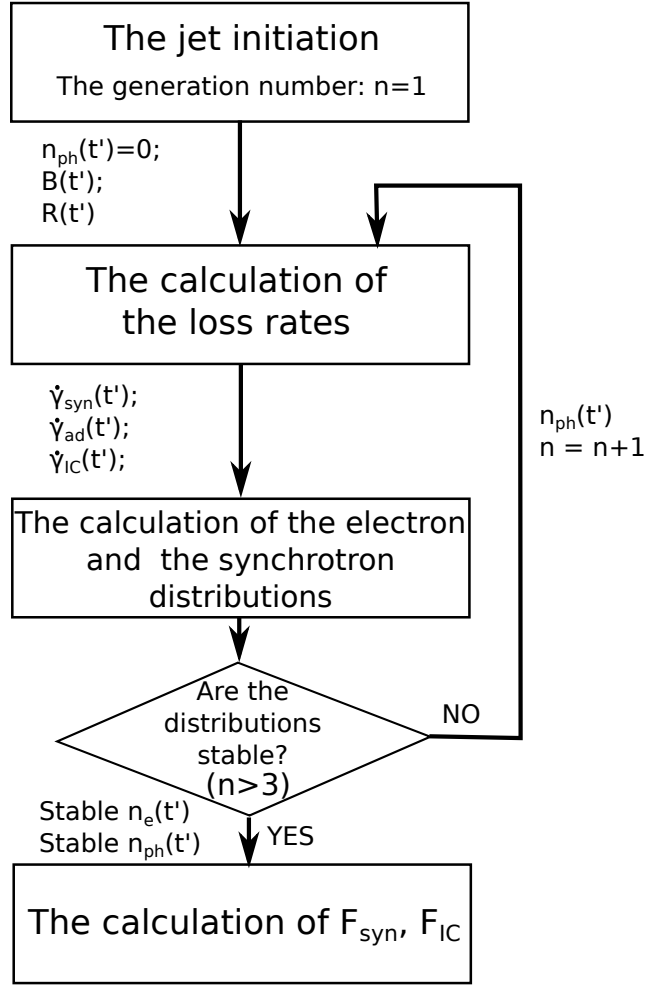


Figure 4.4: Diagram demonstrating the algorithm used to calculate the spectra emitted by the inhomogeneous, non-local model of the jet. In the first generation ( $n = 1$ ), the electron ( $n_e$ ) and the photon ( $n_{ph}$ ) distributions are obtained including only the synchrotron and the adiabatic cooling processes. In the next generations ( $n > 1$ ), the effect of the IC cooling process on the synchrotron photons is included to the calculations of  $n_e$  and  $n_{ph}$ . When the conditions in the layer are stabilized ( $n > 3$ ), then the synchrotron ( $F_{syn}$ ) and the IC ( $F_{IC}$ ) fluxes, emitted by the non-local and homogeneous model of the jet, are calculated.

at the moment,  $t'$ , it is necessary to know the previous state of plasma and local conditions inside the jet. The knowledge about the local magnetic field is needed in order to take into account the synchrotron losses. The transverse expansion has to be known to include the adiabatic losses. The information about the local density of photons is crucial for the IC losses.

In contrast to the one-zone model, the local density of photons in an elongated jet depends on the conditions in other parts of the jet. The strict interrelation between different parts of the jet is an inseparable property of the extended jet models. Then, I use the generation method to calculate the steady differential spectrum of electrons,  $n_{el}$ , at a specific place. In the first generation, I calculate  $n_{el}$  taking into account only

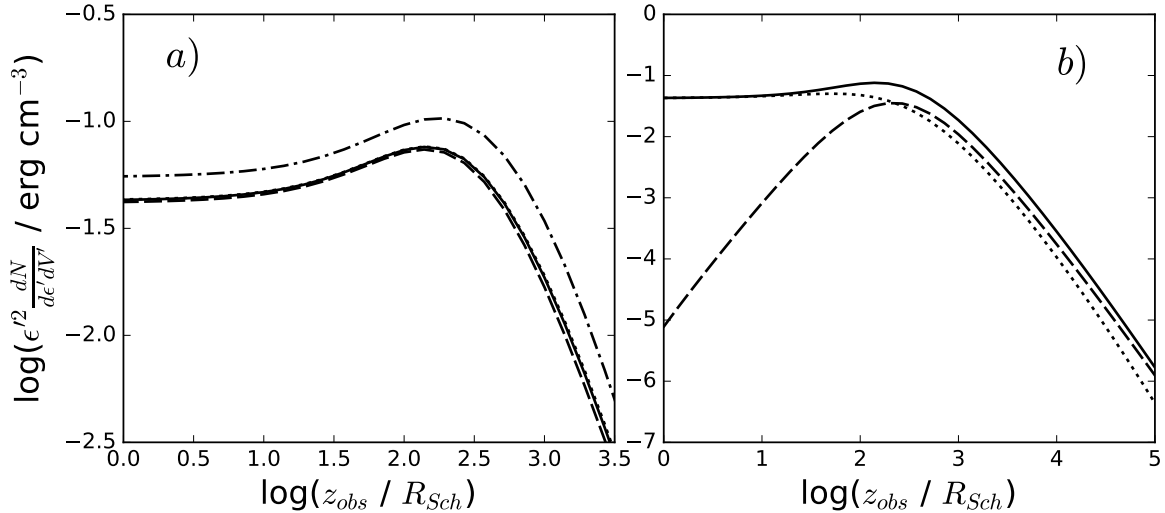


Figure 4.5: Local energy density of photons in the plasma rest frame. Figure (a) shows local density of photons as a function of distance from the jet base for different generations: the first generation of calculations (dot-dashed line, only synchrotron and adiabatic cooling processes are included), the second generation (dashed), the third generation (dotted) and the fourth generation (solid line). Figure (b) shows the local density of photons (for the third generation) as a function of distance for: the backward photons (dashed line), the forward photons (dotted) and the total energy density of photons (solid line). Parameters used in calculations are listed in Tab. 4.1.

the synchrotron and the adiabatic cooling processes. The IC process is ignored due to an unknown local density of photons.  $n_{el}$  is obtained by solving Eq. 4.10. Information about  $n_{el}$  allows to calculate the local density of photons,  $n_{ph}$ , according to Eq. 4.11 and Eq. 4.12. In the second generation, I include the IC cooling of electrons. The local density of photons from the first generation is used in the calculations of  $n_{el}$  in the second generation. In a similar way the next generations are calculated, i.e. the local density of photons from the previous generation is used in the calculation of  $n_{el}$  in the current generation. The scheme of the generation method of calculation of steady  $n_{el}$  and  $n_{ph}$  is shown in Fig. 4.4.

The comparison of the local energy densities of the synchrotron photons is shown in Fig. 4.5. In the first generation, the energy of electrons is lost only in the adiabatic and in the synchrotron processes. Therefore, the local density of photons is noticeably larger. In the second and next generations, where electrons lose energy also on the IC process, the density of photons is smaller. I have found that after the second generation the local density of photons is almost stable.

As I mentioned in section 4.2, it is assumed that the local low-energy photon field is composed of the forward and the backward photons. In Fig. 4.5, I present the local density of photons as a function of distance from the jet base. The local density of the forward photons dominates close to the jet base. On the other hand, the backward photons slightly dominate at the outer part of the jet. The maximum local density of

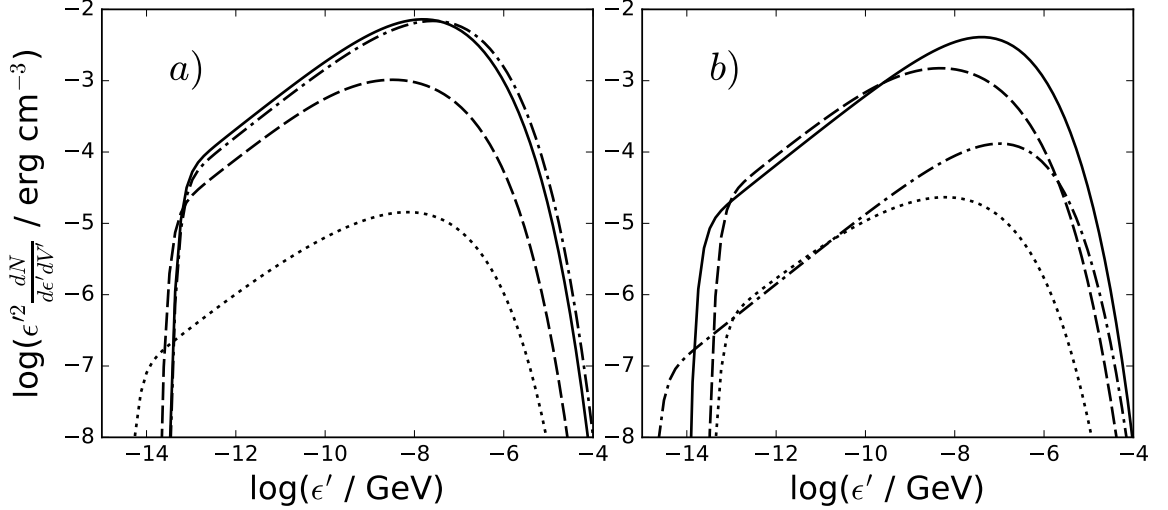


Figure 4.6: The differential energy density of photons as a function of photon energy for the forward photons (a) and for the backward photons (b). The specific curves shows the spectra for different distances from the jet base equal to:  $10R_{Sch}$  (dot-dashed line),  $10^2R_{Sch}$  (solid),  $10^3R_{Sch}$  (dashed) and  $10^4R_{Sch}$  (dotted). Parameters used in the calculations are listed in Tab. 4.1.

photons occurs at distance  $z' \sim 10^2R_{Sch}$ .

Because the backward and the forward photons arrive from the different parts of the jet, the spectra of low energy photons are different. Then, not only the level of the energy density of photons but also the shapes of the photon spectra depend on the distance from the jet base. In Fig. 4.6, I show the differential energy densities of the synchrotron photons for four different places in the jet. For the smallest distances from the jet base, the energy density of the forward photons is much larger than the energy density of the backward photons. For such distances, the energy density of the backward photons extend to lower energies due to the lower efficiency of SSA process (the path traveled by photons is smaller). For the largest distances, the situation is reversed. The energy density of photons is slightly dominated over the backward photons. Whereas, the energy density of the forward photons extend to lower energies than the energy density for the backward photons.

To solve the kinetic equation for electrons given by Eq. (4.10), I use the numerical method described by Chiaberge and Ghisellini (1999). This algorithm is based on the implicit difference scheme presented in Chang and Cooper (1970). In Fig. 4.7a, I present the results of the numerical calculation of the differential spectrum of electrons. This figure shows the differential electron energy density for different generations. The electron spectrum depends on the generation. The maximum energy of electrons decreases when the IC cooling is included in the calculations. In order to get stable electron spectra, the method has to be repeated typically three times. After third generation,  $n_e$  is already stable (Fig. 4.7b).

The electron spectrum changes with the distance from the jet base. The density

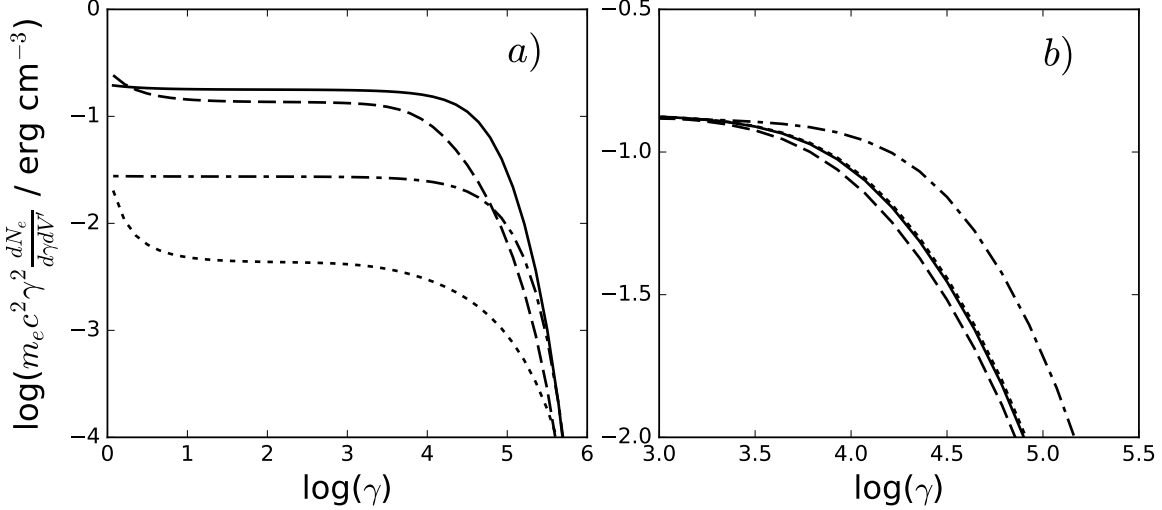


Figure 4.7: (a) The equilibrium spectra of electrons (in the plasma rest frame) at the distance from the jet base,  $z_{obs}$ , at:  $10R_{Sch}$  (dot-dashed line),  $10^2R_{Sch}$  (solid),  $10^3R_{Sch}$  (dashed) and  $10^4R_{Sch}$  (dotted line). (b) The spectra of electrons at the distance  $z_{obs} = 10^3R_{Sch}$  for different generations: the first generation (dot-dashed line, only synchrotron and adiabatic cooling are included), the second generation (dashed), the third generation (dotted) and the fourth generation (solid line). The parameters of the model are listed in Tab. 4.1.

of electrons decreases with the distance as a result of the increasing cross-section of the jet. The magnetic field and the local density of photons decrease with the distance along the jet (cf. Fig. 4.5b). Because of that, the energy losses of electrons drops and the maximum energy of electrons increases with the distance from the jet base (see Eq. 4.7). These dependencies are shown in Fig. 4.7b.

The knowledge about the equilibrium conditions in the jet, i.e.  $n_{el}(\gamma, z')$ ,  $n_{ph}(\epsilon, z')$ , and  $B(z')$ , allows to calculate the emissivities and the absorption coefficients. Finally, the observed flux of the emitted radiation from the jet is obtained. The formulas for the radiation processes are discussed in Chapter 2.

## 4.3 Spectra produced for different parameters of the jet

### 4.3.1 The example of spectral energy distribution

As an example, I calculate the multiwavelength spectra emitted by the jet in terms of the considered inhomogeneous non-local model for typical parameters of BL Lac objects. The model is defined by the following parameters. The black hole mass used in the calculation is  $M_{BH} = 10^8 M_{\odot}$ . It is a typical mass of black holes in AGNs. For such a mass of the SMBH, the Schwarzschild radius is equal to  $R_{Sch} \approx 3 \times 10^{13}$  cm. The calculations are carried out for the region in the jet between  $z_0 = 0$  to  $z_{max} = 10^7 R_{Sch}$ .

Parameter	Symbol	Value	Unit
Mass of the black hole	$M_{BH}$	$10^8$	$M_\odot$
Bulk Lorentz factor of the jet	$\Gamma_j$	10	–
Radius of the jet base	$R_0$	10	$R_{Sch}$
Transverse expansion coefficient	$\rho$	0.2	–
Magnetic field at the jet base	$B_0$	1	G
Index of magnetic field profile	$b$	1	–
Power injected in electrons	$L'_{inj}$	$10^{42}$	erg/s
Index of injection profile	$q$	1	–
Spectral index of electrons	$s$	2.0	–
Acceleration coefficient	$\eta$	$10^{-6}$	–
Minimum energy of electrons	$\gamma_{min}$	1	$m_e c^2$
End point of electron acceleration	$z_{end}$	$10^6$	$R_{Sch}$
Observation angle	$\theta_{obs}$	0.1	rad

Table 4.1: The basic parameters of the jet used in the calculations in this Chapter. I use parameters from this table, unless otherwise noted.

However, electrons are accelerated only to  $z_{end} = 10^6 R_{Sch}$ . Above  $z_{end}$ , the electrons only lose energy. The radius of the jet at its base is fixed on  $R_0 = 10 R_{Sch}$ . The bulk Lorentz factor of the jet is constant. It is equal to  $\Gamma_j = 10$ , which is a commonly accepted value for blazars (see: Chapter 1.). The observation angle of the jet is  $\theta_{obs} = 1/\Gamma_j$ . For this angle, the Doppler factor is  $D_j \simeq \Gamma_j$ . Assuming that the transverse expansion coefficient is  $\rho = 0.2$  (Clausen-Brown et al., 2013), the half-opening angle of the jet is  $\phi = \rho/\Gamma_j = 0.02$  rad. I assume that the magnetic field in the jet is inversely proportional to the jet radius,  $R_j$ , i.e.  $b = 1$ . The strength of the magnetic field at the jet base is  $B_0 = 1$  G. The power in relativistic electrons injected into the jet is much smaller than the Eddington luminosity. It is equal to  $L'_{inj} = 10^{42}$  erg/s. The acceleration coefficient is  $\eta = 10^{-6}$ . The spectral index of injected electrons is fixed to the value of  $s = 2$ . All these parameters are listed in Tab. 4.1

In Fig. 4.8 (on the left), I show the example of the spectral energy distribution (SED) of produced radiation which is calculated by using the considered model. I present the radiation produced in the synchrotron process and in the IC process in the case of the scattering of the backward and the forward photons. The low-energy break, visible in the synchrotron spectrum, is located at  $\sim 10^{-4}$  eV. It is caused by the self-synchrotron absorption (SSA) process. In Fig. 4.8 (on the right plot), the synchrotron flux is shown. Note that the optically thick synchrotron flux is flat which is in agreement with the predictions of the model of Blandford and Königl (1979).

The considered model reconstructs properly the shape of the spectra of the typical HBL blazars in a low activity state. The peak of the synchrotron bump is located at

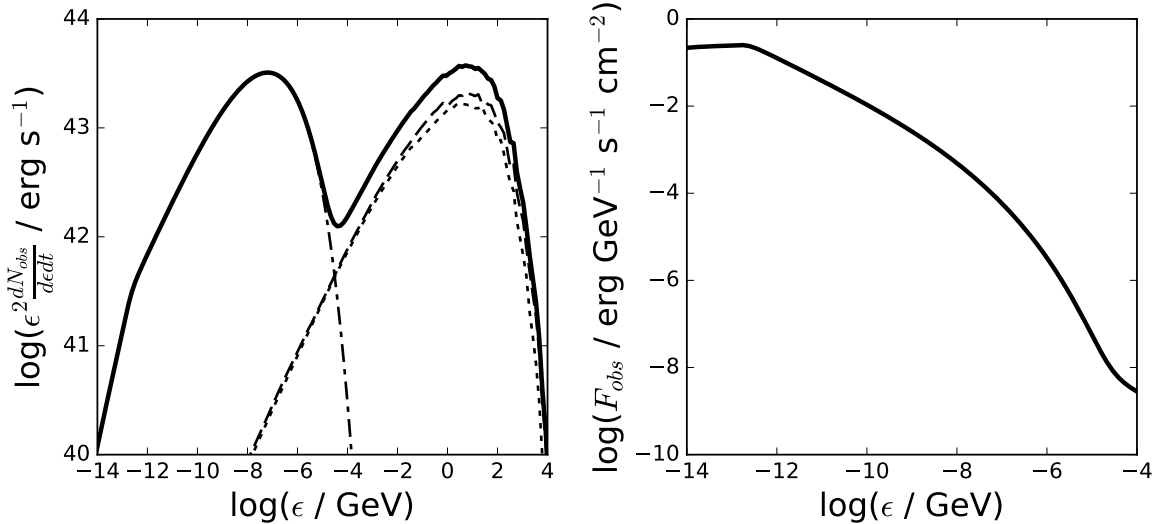


Figure 4.8: (Left plot) The Spectral Energy Distribution (SED) of the multiwavelength spectrum for the parameters listed in Tab. 4.1 in the observer rest frame. Specific curves represent radiation from different emission processes: synchrotron radiation (dot-dashed curve), IC radiation from scattering backward photons (dashed), IC radiation from scattering forward photons (dotted) and total radiation emitted by the jet (thick-solid curve). (Right plot) The observed flux of synchrotron radiation. A visible break is seen between the optically thick and the optically thin emission regimes due to the SSA process in the jet. Note that the optically thick part of the spectrum is flat. It is in agreement with results found by Blandford and Königl (1979). The luminosity distance to the source is  $d_L = 220$  Mpc.

$\sim 10^{-7}$  GeV, i.e. at the typical value for the low luminosity blazars (Ghisellini et al., 2017). The photons of the high energy peak have the multi-GeV energy. The SED shows significant curvature at both peaks. The synchrotron and the IC spectra with energies between the peaks and the SSA break can be well described by single power-laws.

### 4.3.2 Geometry of the jet

In the considered model, I assume that the jet has the shape of the truncated cone with the radius at the base  $R_0$ . The half-opening angle of the jet is  $\phi = \rho/\Gamma_j$ , where  $\Gamma_j$  is constant.  $\rho$  is expected to take the value of the order of  $\sim 0.2$ . I investigate the emission from the jet for different values of  $\rho$ . Except for the standard value  $\rho = 0.2$ , I also examine the jet which has almost cylindrical shape,  $\rho = 0.05$ , and the jet characterized by fast transverse expansion,  $\rho = 0.5$  (see Fig. 4.9a). In the case of a slow transverse expansion of the jet, the magnetic field in the jet is almost independent on the distance. On the other hand, the density of relativistic electrons increases due to the continuous injection of electrons. Therefore, the emission processes in the jet are more efficient. In the opposite case, when the cross-section of the jet expands rapidly, the strength of the magnetic field decreases fast and the adiabatic cooling becomes important.

The jet radius at the base is characterized by the parameter  $R_0$ . The smaller value

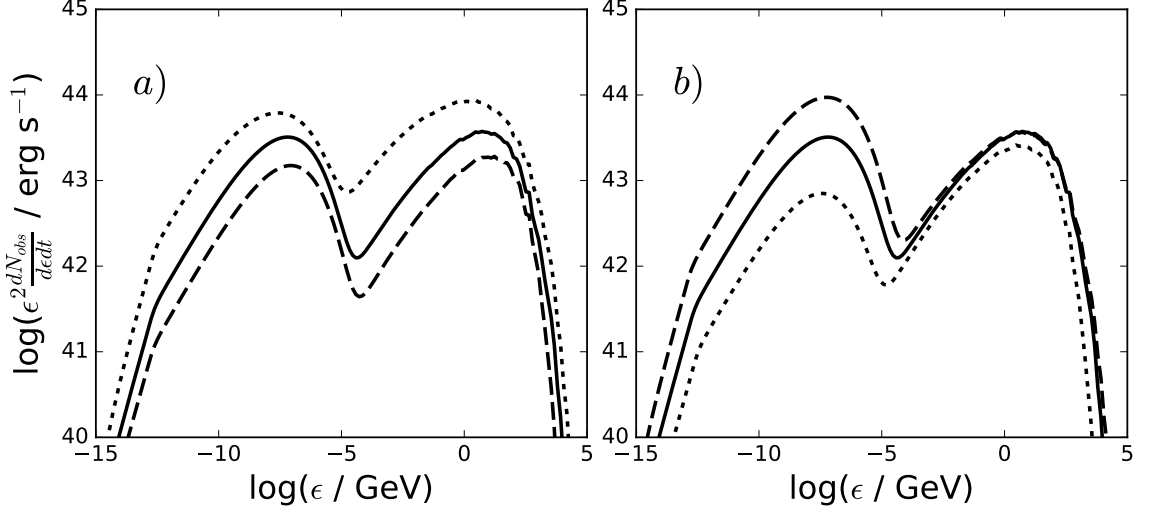


Figure 4.9: (a) SEDs for the different transverse expansion parameter:  $\rho=0.05$  (dotted line),  $\rho=0.2$  (solid) and  $\rho=0.5$  (dashed). (b) SEDs for the different radii of the jet:  $R_0 = 3R_{Sch}$  (dashed line)  $R_0 = 10R_{Sch}$  (solid) and  $R_0 = 30R_{Sch}$  (dotted). Other parameters of the model are listed in Tab. 4.1.

of  $R_0$  means that the density of photons is larger for region placed close to the jet base. But, the influence of  $R_0$  on the conditions inside the jet is more complex because of all parameters of the jet change proportional to  $R(z)$  which is given by Eq. 4.1. The parameters of the jet change relatively slowly close to the jet base. The difference between the values of parameters at the jet base and at the distance  $z$  becomes noticeable for distances  $z \gg R_0$ . The SED obtained for the small value of  $R_0$  shows strong IC emission due to the higher density of the low energy photons. Simultaneously, the synchrotron emission is weaker due to the rapidly decreasing strength of the magnetic field. This behavior is clearly seen in Fig. 4.9b. It should be reminded, that the value of  $R_0$  is given in units of the Schwarzschild radius. Therefore, the absolute value of  $R_0$  depends also on the mass of the black hole,  $M_{BH}$ .

### 4.3.3 Magnetic field

The strength of the magnetic field is a crucial component of the jet. It regulates the emission efficiency of the synchrotron radiation in jets. The magnetic field is especially important for the HBLs, where the synchrotron cooling process dominates over other losses in the jet. Furthermore, the synchrotron radiation produced by the relativistic electrons in the magnetic fields is an important photon field for the inverse Compton scattering. In the considered model, the magnetic field is governed by two parameters: the strength of the magnetic field at the jet base,  $B_0$ , and the index defining the profile of the magnetic field,  $b$  (see Eq. 4.3).

If the Poynting flux along the jet axis is conserved, the profile of the magnetic field should be inversely proportional to the radius of the jet, i.e.  $b = 1$ . In case of the

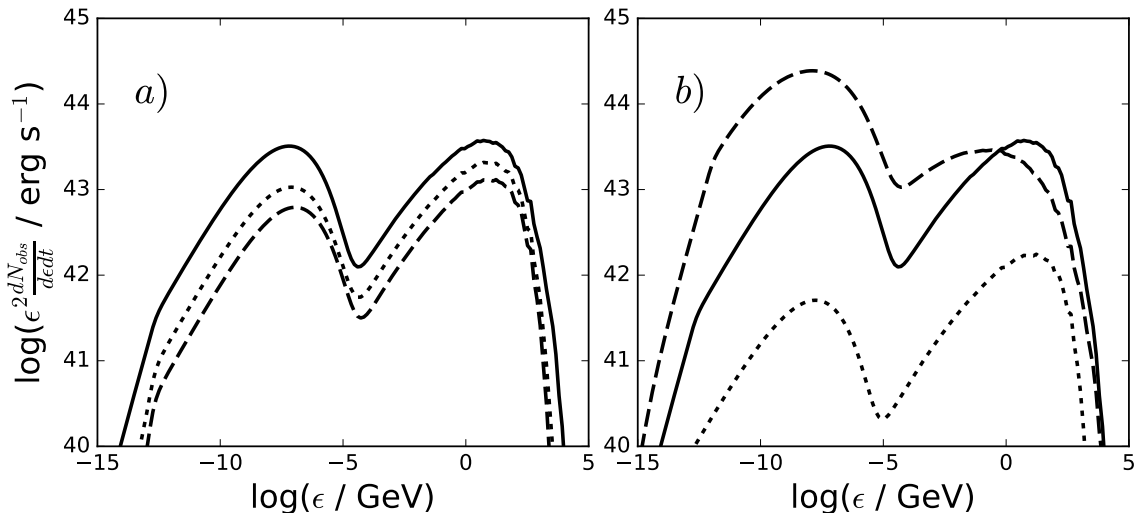


Figure 4.10: (a) SEDs for different index of magnetic field profile:  $b = 1$  (solid line),  $b = 1.5$  (dotted) and  $b = 2$  (dashed). Right plot (b) SEDs for different strength of magnetic field at the jet base :  $B_0 = 10$  G (dashed line)  $B_0 = 1$  G (solid) and  $B_0 = 0.1$  G (dotted). Other parameters of the model are listed in Table 4.1.

dominant poloidal magnetic field or in case of the acceleration of relativistic particles at the expense of the magnetic energy, the magnetic field decreases much faster with the distance, i.e.  $b > 1$ . In Fig. 4.10a, I present the SEDs for three different models of the magnetic field profiles (different values of the parameter  $b$ ). For a higher value of  $b$ , the luminosity of the jet decreases as a result of the inefficient cooling of electrons in more distant regions of the jet.

The strength of the magnetic field at the jet base is one of the most important parameters of the jet. The synchrotron cooling depends on the magnetic field like  $\dot{\gamma}_{syn} \propto B^2$ . Therefore, even a small change of  $B_0$  has a significant influence on the shape of SED. For a small value of  $B_0$ , the IC bump dominates the SED. Only electrons with the higher energies emit efficiently synchrotron radiation, thus the spectra are flat. For higher values of  $B_0$ , the strength of the synchrotron bump increases. As a result of the efficient cooling process, the spectra are smooth and broad. This behavior is shown for different values of  $B_0$  (see Fig. 4.10b). The energy of the break caused by the self-synchrotron absorption increases for the increasing strength of the magnetic field.

The location of peaks of the IC bump depends on the maximum Lorentz factor of electrons according to Eq. 4.7. When the cooling processes are dominated by the synchrotron process, then  $\gamma_{max} \propto B^{-1/2}$ . If the magnetic field is strong ( $B_0 = 10$  G), then the maximum energies of electrons close to the jet base are relatively low due to the large synchrotron losses ( $\gamma_{max} \sim 10^4$ ). In more distant parts of the jet,  $\gamma_{max}$  increases gradually as a result of decreasing magnetic field. Similar situation occurs for  $B_0 = 1$  G. However, in this case,  $\gamma_{max} \sim 10^5$  close to the jet base. Therefore, the peak of the IC bump is located at higher energies. For the low value of the magnetic field strength,  $B_0 = 0.1$  G, the energy losses on the synchrotron process are lower than

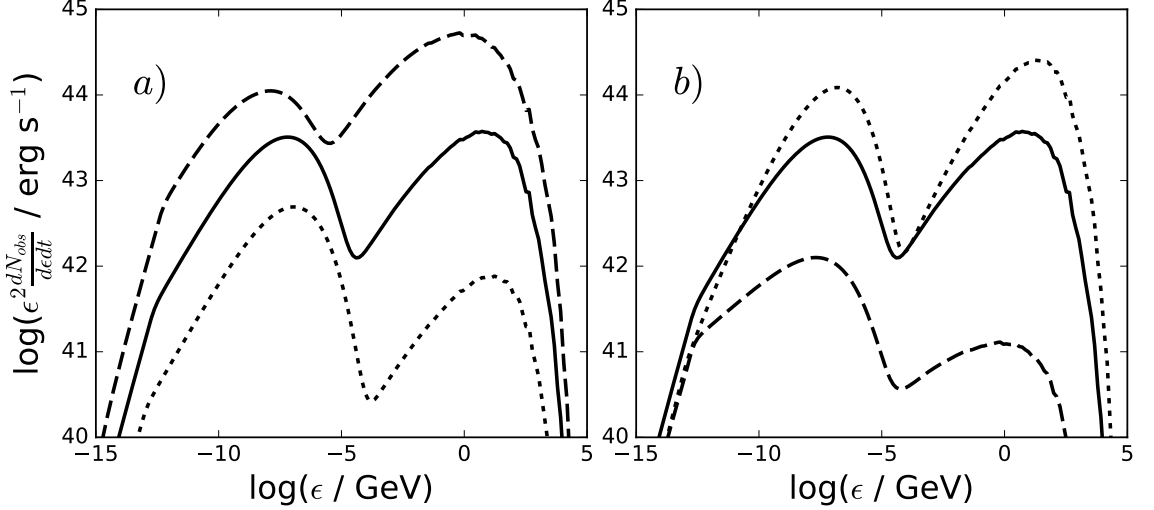


Figure 4.11: (a) SEDs for the different total injected power in relativistic electrons:  $L'_{inj} = 10^{41}$  erg/s (dotted line),  $L'_{inj} = 10^{42}$  erg/s (solid) and  $L'_{inj} = 10^{43}$  erg/s (dashed). (b) SEDs for the different spectral indices of injected electrons:  $s = 2.3$  (dashed line),  $s = 2.0$  (solid) and  $s = 1.7$  (dotted). Other parameters of the model are listed in Tab. 4.1.

on the adiabatic process. Hence, the maximum energy of electrons is governed by the adiabatic losses. In this case,  $\gamma_{max}$  is almost constant in the whole jet,  $\gamma_{max} \sim 10^5$ .

#### 4.3.4 Electron acceleration

The non-thermal radiation emitted by jets is assumed to originate in the leptonic processes produced by the relativistic electrons. The distribution of the relativistic electrons affects the emitted multiwavelength spectra. Typically, the power law distribution of the electrons with the low energy and the high energy cut-offs is adopted. High energy electrons (and positrons) lose efficiently energy in typical conditions of the internal jets. This suggests that the electrons have to be accelerated close to the emission place, (*in situ* acceleration). In the model, I assume that the electrons are accelerated in an extended part of the jet located between  $z_0$  and  $z_{end}$ . In this region, the fresh electrons are injected with the power law distribution and the exponential cut-off. The electron's distribution is parametrized by the spectral index,  $s$ , the local normalization of the injected electrons,  $Q$ , the minimum energy of the injected electrons,  $\gamma_{min}$  and the maximum energy of the electrons,  $\gamma_{max}$ . The local normalization,  $Q$ , depends on the total power injected into the jet in the form of the relativistic electrons,  $L_{inj}$ . The form of the dissipation profile is governed by the parameter  $q$  (see: Eq. 4.4 and Eq. 4.6).  $\gamma_{max}$  is calculated self-consistently by the comparison of the total cooling time scale of the electrons with their acceleration time scale. The latter is characterized by the acceleration coefficient,  $\eta$ .

The relation between observed SED and the injected power in the relativistic electrons,  $L'_{inj}$  is shown in the Fig. 4.11a. The luminosity of the synchrotron radiation rises

roughly linearly with the increasing  $L'_{inj}$ . The IC radiation increases with the square of  $L'_{inj}$ . Such a behavior is characteristic for the synchrotron self-Compton (SSC) process. The luminosity of IC bump is proportional to the energy density of low energy photons and the density of electrons. Increasing the injected power,  $L'_{inj}$ , both this quantities increase linearly. Then, the luminosity of the IC bump increases much faster than  $L'_{inj}$ . Note that the mentioned above features are correct only when the synchrotron bump exceeds the IC one, i.e. when the synchrotron energy losses dominate over the IC losses.

When the IC radiation dominates over the synchrotron radiation, the power emitted in  $\gamma$ -rays begins to increase linearly, where the synchrotron power change clearly slower. For very large  $L'_{inj}$ , the spectra are smooth and broad as a result of large loss rates even for electrons with relatively low energies. Note, that with increasing  $L'_{inj}$  the position of the break caused by SSA in the synchrotron spectrum between the optically thin and the optically thick parts is shifted to higher energies. This is due to the linear relation between the absorption coefficient and differential number of electrons (see Eq. 2.15).

The injected electron spectrum have a power law form. The spectral index,  $s$  depends on the acceleration process and on the conditions in the acceleration region. The most commonly adopted value of the spectral index is 2.0. Distribution of electrons with a similar value of the spectral index can be formed in the acceleration of the shocks. I show SEDs produced by electrons for different values of the spectral index, the hard one ( $s = 1.7$ ), the soft ( $s = 2.3$ ) and the classical value ( $s = 2$ ) (see Fig. 4.11 b). The spectral index affects the slopes of both, the synchrotron and the IC spectra. When the spectral index decreases, then the number of electrons with the highest energy also increases. These electrons lose energy most efficiently. Therefore, the total emitted power is larger in the case of the harder spectral index.

The acceleration time scale of electrons,  $\tau_{acc}$ , is characterized by the acceleration coefficient  $\eta$ . This parameter affects the maximum electron energy in a specific place of the jet (according to Eq. 4.7). Then, with increasing  $\eta$ , the observed spectra are shifted to the higher energies. The dependence of the spectra on  $\eta$  is presented in Fig. 4.12a. Note, that for a larger value of  $\eta$ , the observed luminosity of the jet increases due to the more efficient cooling processes of the electrons with the highest energies. The peak of the synchrotron bump shifts almost linearly with  $\eta$ . The peak of IC bump for large  $\eta$  shifts slowly to the higher energies. This effect is caused by the scattering of the synchrotron photons deeply in the Klein-Nishina regime. Note that even for the very large value of  $\eta$ , the peak of the IC bump is located around 100 GeV.

The injected power-law distribution of electrons may be truncated at low energies. It is described by  $\gamma_{min}$ . For a large value of  $\gamma_{min}$  and this same value of  $L'_{inj}$  more energy is injected in the HE electrons which lose energy more efficiently. Therefore, with increasing value of  $\gamma_{min}$ , the luminosity of the jet also increases.

The form of the acceleration profile along the jet axis,  $Q(t') = Q_0(R_0/R(t'))^q$ , is a very important issue in the elongated jet model. In contrast to the one-zone model, the

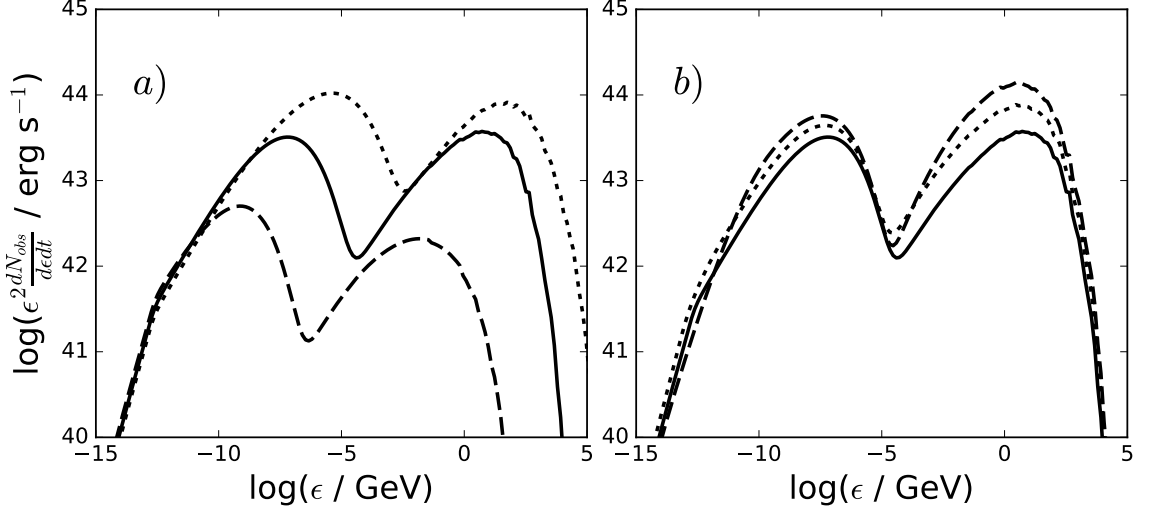


Figure 4.12: (a) SEDs for the different acceleration coefficients:  $\eta = 10^{-4}$  (dotted line),  $\eta = 10^{-6}$  (solid) and  $\eta = 10^{-8}$  (dashed). (b) SEDs for different minimum energy of electrons injected into the jet:  $\gamma_{min} = 1$  (solid line),  $\gamma_{min} = 3 \times 10^2$  (dotted) and  $\gamma_{min} = 3 \times 10^3$  (dashed). Other parameters of the model are listed in Tab. 4.1.

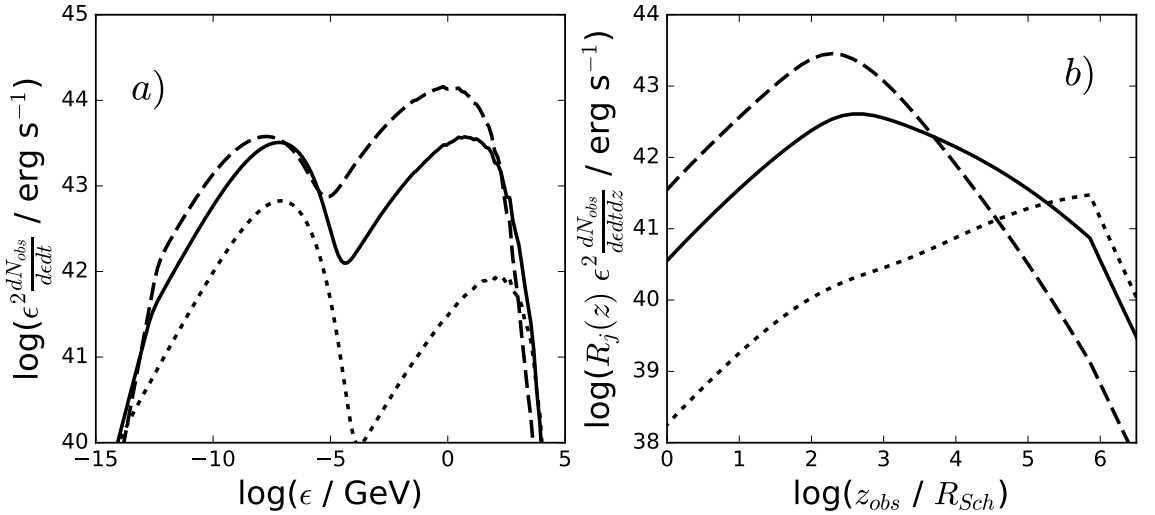


Figure 4.13: (a) SEDs for the different index of injection profile:  $q = 2.0$  (dashed line),  $q = 1.0$  (solid) and  $q = 0.0$  (dotted). (b) The luminosities emitted from the characteristic region of the jet (with volume  $V = \pi R_j^3(z_{obs})$ ) as a function of distance from the jet base in observers frame (more details in the text). Different lines indicate different values of  $q$ :  $q = 2.0$  (dashed line),  $q = 1.0$  (solid) and  $q = 0.0$  (dotted). Other parameters of the model are listed in Tab. 4.1.

acceleration occurs in the large volume of the jet, between  $z_0$  and  $z_{end}$ . I consider three various values of  $q$ , which characterize the acceleration profile. When  $q = 0$ , the same amount of energy is injected into every part of the jet. As a result, the majority of radiation is produced at the outer part of the jet, at distance  $\sim z_{end}$ . In this region, the magnetic field is weak and the density of the synchrotron photons is low. For  $q = 1$ , the radiation is produced in a broad part of the jet. Such emission profile was considered by

e.g. Malzac (2013). For  $q = 2$  mainly the region close to the base of the jet produces a large amount of radiation. This means that such dissipation profile can be successfully replaced with the one-zone model.

I compare the radiation produced in the jets with different dissipation profiles (see Fig. 4.13). For small  $q$ , the  $\gamma$ -ray luminosity of the jet is small because a large part of electron's energy is being injected in a radiatively non-efficient region of the jet. In the case of  $q = 2$ , the dissipation occurs mainly close to the jet base where the magnetic field is strong and the radius of the jet is small. This provides the most favorable conditions for production of the synchrotron and the IC radiation.

I show the dependence of the total emitted power as a function of the distance from the jet base in Fig. 4.13b. This dependence is shown for different values of  $q$ . In each case, I calculate the radiation produced in the characteristic region of the jet, which volume is defined by  $V = \pi R_j^3$  in the observer rest frame, i.e. the volume of the cylinder with the cross-section of the jet at a specific distance and with the length equal to the radius of the jet. The power emitted from the volume  $V$  is  $R_j(z) \times \epsilon^2 dN/(dt d\epsilon dz)$ . I conclude that if the dissipation of energy in the jet is described by  $0 < q \leq 1$ , then the extended jet model has to be considered.

### 4.3.5 Observation angle

The low energy radiation in the extended jet is significantly anisotropic in both the observers and the plasma rest frames (in the contrast to the simplified homogeneous one-zone SSC model, which assumes that the radiation and electrons are isotropic in the emission zone in the plasma rest frame). Because of that, the radiation produced in the IC process is also anisotropic. The cross section for the IC scattering is the largest when the scattering angle (the angle between the direction of incoming photons and the line of sight) is very small. It is especially important for the IC scattering process in the Klein-Nishina regime. However, note that in the Klein-Nishina regime, the cross section for the IC scattering is gradually decreasing with the energy of the scattered photons. The angular dependence of the IC cross section means that the IC bump in the AGN spectrum will be larger for the small observation angles (then the forward photons are scattered) or for the relatively huge observation angle. This means that the backward photons are scattered efficiently.

The SEDs for selected observation angles,  $\theta_{obs}$ , are shown in Fig 4.14. With decreasing observation angle, the observed luminosity of the jet increases as a result of the Doppler boosting effect and the energy of photons are shifted to the higher energies. The dominant component of the IC radiation changes significantly for large and small observation angles. For small  $\theta_{obs}$ , most of the radiation comes from the scattering of the forward photons. Otherwise, for large  $\theta_{obs}$ , the IC radiation is produced mainly in the Compton scattering of the backward photons. Both components, from the scattering of the backward and the forward photons, are comparable when the observational

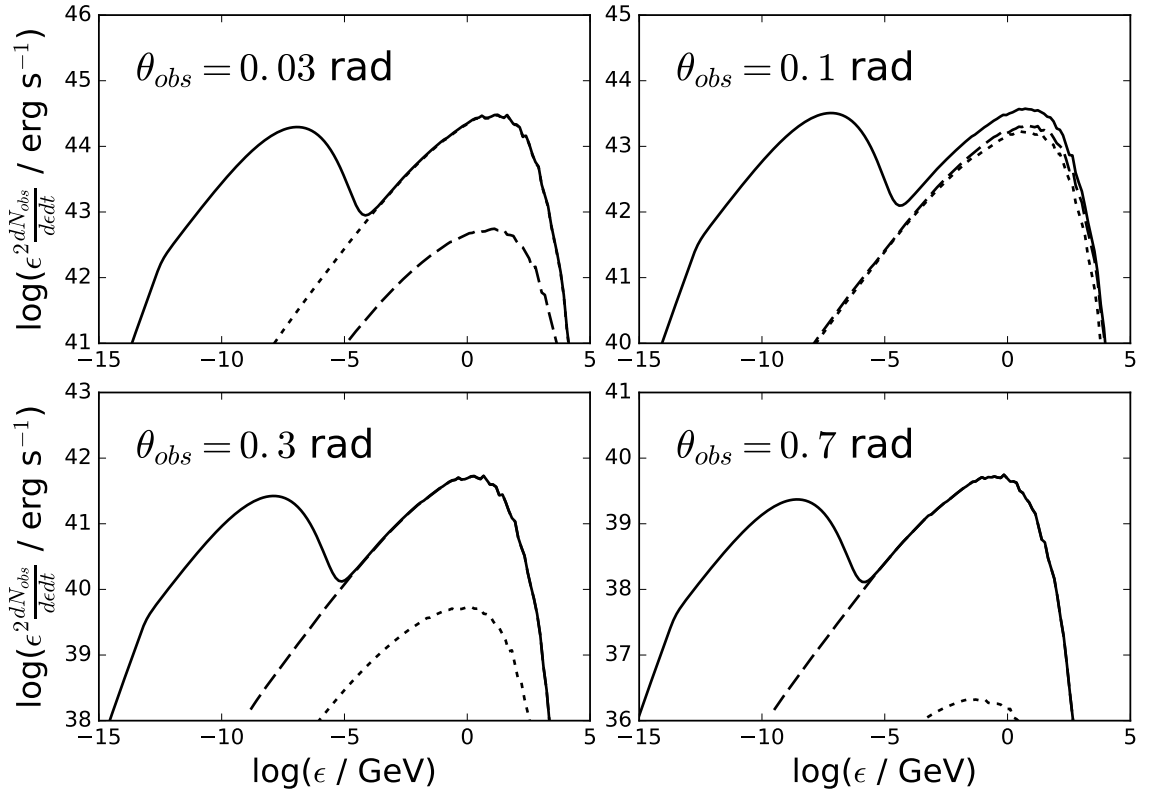


Figure 4.14: SEDs for four different values of the observation angles:  $\theta_{obs}=0.03$ ,  $\theta_{obs}=0.1$ ,  $\theta_{obs}=0.3$ ,  $\theta_{obs}=0.7$  rad. The total emission from the jet is showed by the solid lines, the IC radiation from scattering of the backward photons by the dashed lines, and of the forward photons by the dotted lines. Other parameters are listed in Tab. 4.1.

angle is close to  $1/\Gamma_j$  (see Fig. 4.14 for  $\theta_{obs} = 0.1$  rad). For this angle, the ratio between the luminosities of the synchrotron and the IC bumps is the largest.

## 4.4 Application of non-local inhomogeneous jet model to Mrk 421

As an example, I interpret the long-term observation of well-studied blazar Markarian 421 (Mrk 421). It is the relatively nearby object with the redshift  $z = 0.031$ , which corresponds to the luminosity distance equal to 140 Mpc. Mrk 421 belongs to high-frequency BL Lacs, with the low and high energy peaks located in X-ray and  $\gamma$ -ray ranges. This blazar has been the first extragalactic source detected in VHE range (Punch et al., 1992). Typically, it is modeled with the one-zone SSC model (e.g. Bednarek and Protheroe, 1997b; Tavecchio et al., 1998).

Here, I interpret the Mrk 421 SED in terms of the inhomogeneous stationary model. I compare the SED calculated with the model with the observations that were carried out during the 4.5-month long campaign (Abdo et al., 2011b). During this campaign, Mrk 421 was in the low-activity state. More details about the variability during this

Parameter	Symbol	Model A	Model B	Unit
Mass of the black hole	$M_{BH}$	$3 \times 10^8$	$3 \times 10^8$	$M_\odot$
Bulk Lorentz factor of the jet	$\Gamma_j$	5	30	–
Radius of the jet base	$R_0$	10	10	$R_{Sch}$
Transverse expansion coefficient	$\rho$	0.2	0.2	–
Magnetic field at the jet base	$B_0$	2.1	0.27	G
Index of magnetic field profile	$b$	1	1	–
Power injected in electrons	$L'_{inj}$	$4.9 \times 10^{42}$	$9.5 \times 10^{40}$	erg/s
Index of injection profile	$q$	0.6	1	–
Spectral index of electrons	$s$	1.5	2.0	–
Acceleration coefficient	$\eta$	$1.8 \times 10^{-6}$	$7 \times 10^{-7}$	–
Minimum energy of electrons	$\gamma_{min}$	1	$1.5 \times 10^3$	$m_e c^2$
End point of electron acceleration	$z_{end}$	$10^6$	$10^6$	$R_{Sch}$
Observation angle	$\theta_{obs}$	0.1	0.03	rad

Table 4.2: The parameters of the inhomogeneous model for Mrk 421.

campaign may be found in (Aleksić et al., 2015a). This object gives a good opportunity to interpret this low-activity state in terms of the non-local, inhomogeneous and stationary model of the jet.

The weakness of the inhomogeneous model in the comparison with one-zone SSC models is a relatively large number of free parameters. The considered model is characterized by 13 free parameters. Such a large number of parameters allows to model one SED with different sets of the parameters. However, note that the one-zone SSC model presented in Abdo et al. (2011b) has a similar number of free parameters (11 free parameters) despite a substantial simplicity of the model. Moreover, in the inhomogeneous stationary model, the electron spectrum is obtained self-consistently.

Here, I examine two different scenarios. In the first model, I assume that the bulk Lorentz factor of the jet is relatively small (of the order of a few). This agrees with the radio observations of Mrk 421 (e.g. Lico et al., 2012). In the second model, I adopt a much larger value of the bulk Lorentz factor,  $\Gamma_j \geq 10$ , which is often used in modeling of TeV blazars. In both cases, the black hole mass is  $M_{BH} = 3 \times 10^8 M_\odot$ , what is consistent with the estimations of the black hole mass for Mrk 421 (Wu et al., 2002; Barth et al., 2003). The transverse expansion coefficient is  $\rho = 0.2$  (Clausen-Brown et al., 2013) and the radius of the jet at the base is  $R_0 = 10R_{Sch}$ . I also assume that the magnetic field is dominated by the toroidal component, i.e.  $b = 1$ . These assumptions reduce the number of free parameters to 8. The values of other parameters are obtained with the SED modeling of Mrk 421.

In Fig. 4.15, I show the example of the SED modeling of Mrk 421. I include the effects of  $\gamma$ -ray absorption on the extragalactic background light (EBL). The optical

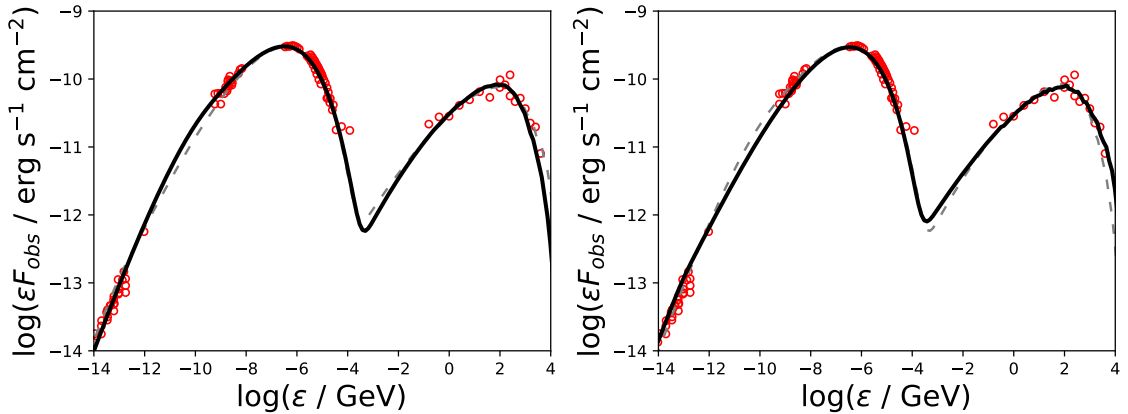


Figure 4.15: SEDs of Mrk 421 calculated with the inhomogeneous model of the stationary jet. Data points (red, open circles) are reconstructed from Abdo et al. (2011b). The left plot shows the fit for the Model B and the right plot for the Model A. The another model (Model A on the left plot, Model B on the right plot) is shown with the dashed grey line. The EBL absorption is included according to the model of Gilmore et al. (2012). The parameters of the models are listed in Table 4.2.

depth for the absorption on the EBL is taken from Gilmore et al. (2012). The values of the parameters used in the modeling are listed in Tab. 4.2. Note, that in this inhomogeneous model, the high energy part of the synchrotron spectrum is characterized by a relatively large curvature. In one-zone models, it is compensated by the postulated breaks in the electron distribution. It is noteworthy that the inhomogeneous model reproduces correctly also the low energy part of SED in the radio range.

Model A is characterized by the small bulk Lorentz factor,  $\Gamma_j = 5$ , the relatively strong magnetic field (strength of magnetic field at jet base is  $B_0 = 2.3$  G) and the hard spectral index ( $s = 1.5$ ) (see Fig. 4.15 on the right). The dissipation profile, in this case, is described by  $q = 0.6$ .

In the model B, the Lorentz factor is much higher,  $\Gamma_j = 30$  and the magnetic field at the base of the jet is smaller ( $B_0 = 0.3$  G). The spectral index is  $s = 2.0$ . It is a typical spectral index in the case of the acceleration in the first-order Fermi process. The power injected in relativistic electrons is inversely proportional to the jet radius (i.e.  $q = 1$ ). The correct description of the radiation flux requires a large value of the minimum energy of accelerated electrons ( $\gamma_{min} = 1.5 \times 10^3$ ).

Both models describe well the multiwavelength spectrum of Mrk 421. The observation of short flares in Mrk 421 favors the model B due to the large Doppler factor of the jet. From the other side, the radio observations of the jet in Mrk 421 indicate a much lower value of the Lorentz factor. Then, it is impossible to conclude which applied set of the parameters is more realistic.



# Chapter 5

## Stationary Stratified Jet Model

In the previous Chapter, I consider the inhomogeneous, non-local model of the jet. In that model, the basic parameters of the jet change along the jet axis, i.e. with the distance from the jet base. However, they do not change with the distance transverse to the jet axis. In general case, it is very likely that the parameters also change in the perpendicular direction. For example, the bulk Lorentz factor of the jet,  $\Gamma_j$ , should gradually decrease from the maximum value expected at the axis of the jet ( $\Gamma_j \sim 10$ ) towards the external regions where it is  $\Gamma_j \simeq 1$ . This gradual change of the Lorentz factor of the jet has a huge impact on the physical processes and the radiation emitted from the jet. In such more realistic jet, the radiation from the outer region moving with the small Lorentz factor is enhanced in the frame of the inner region with the larger  $\Gamma_j$ . As a result, the efficiency of the Compton scattering process can be significantly amplified.

Stratified structure of the jet, with the plasma velocity changing with the distance from the jet axis, was suggested by Chiaberge et al. (2000) as a solution of the inconsistencies in the unification scheme of FR I galaxies with BL Lac objects. Also, radio observations of jets in AGNs suggest complex transverse velocity structure of the jet. The observed low Lorentz factors of jets in TeV  $\gamma$ -ray blazars (Piner and Edwards, 2016, 2018) are in contradiction with the high Doppler factors inferred from the SED modeling (Ghisellini et al., 2010) and from the modelling of the extremely fast flares observed in the TeV  $\gamma$ -rays (Begelman et al., 2008). The transverse velocity structures of the AGN jets are also consistent with the limb-brightening of jets detected in many AGNs (Piner et al., 2009; Nagai et al., 2014; Boccardi et al., 2016b). Furthermore, the transverse gradient of the bulk Lorentz factor of the jet has been measured in the nearby radio galaxy M 87 (Mertens et al., 2016).

The evidences of the transverse structure of jets in AGNs became the basis for spine-sheath model, in which the fast spine is surrounded by another component with smaller velocity (Ghisellini et al., 2005). The spine-sheath model was also adopted to the case of blazars with strong emission lines (Sikora et al., 2016). Spine-sheath model has been also proposed as likely explanation of the TeV  $\gamma$ -ray emission from radio

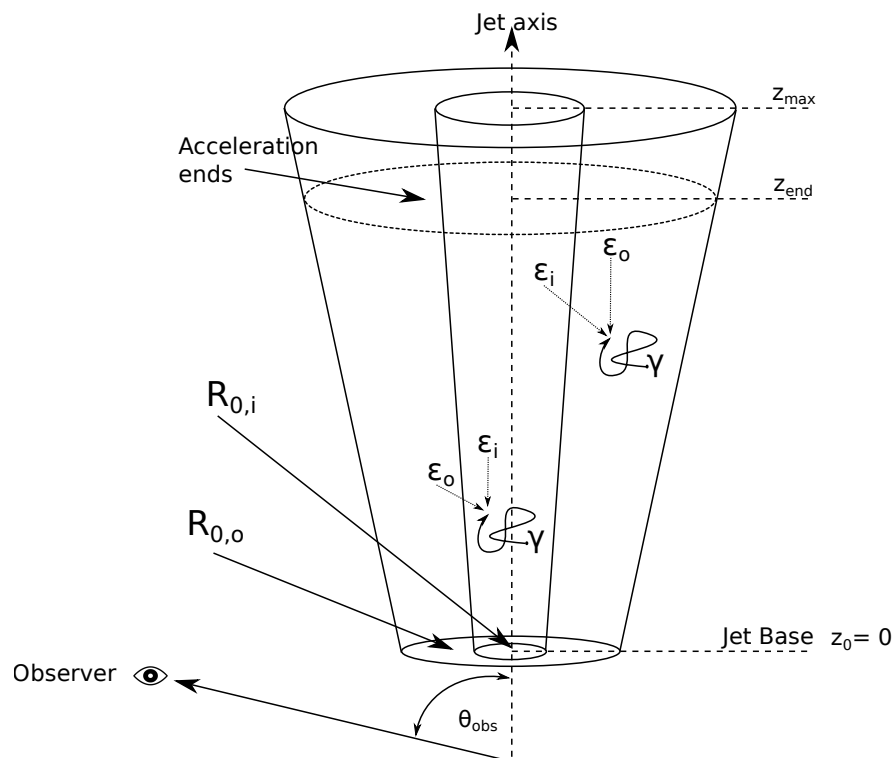


Figure 5.1: The stratified jet in the observer's frame. The jet base is located at the distance  $z_0$ . The jet consists of two components, the outer component with radius at the base  $R_{0,o}$  and the inner component with  $R_{0,i}$ . The observer is located at the angle,  $\theta_{obs}$ , with respect to the jet axes. The relativistic electrons are injected in the region of the jet between  $z_0$  and  $z_{end}$ . Above  $z_{end}$ , electrons only lose energy up to distance  $z_{max} = 10 \times z_{end}$ .

galaxies (Tavecchio and Ghisellini, 2008, 2014; D'Ammando et al., 2015; Janiak et al., 2016).

In this Chapter, I develop an inhomogeneous, non-local spine-sheath jet model (schematically shown in Fig. 5.1). This model can be applied to the quiescent states of blazars and radio galaxies. This two-component model is based on the jet model described in Chapter 4. I calculate photon field in the specific jet component of the jet including the effects of the relativistic boosting and the anisotropic distribution of radiation produced in the other jet components. Due to the interrelation between these jet components, I use the generation method to obtain the steady radiation fields of low-energy photons and the equilibrium spectrum of relativistic electrons in the jet. Afterward, I examine the features of the model for different observation angles. Finally, I use the model to describe the spectra of the HBLs and the FR I radio galaxies in terms of the unification model.

## 5.1 Theoretical description

I consider a jet which is composed of two co-axial cone-shaped components, the inner spine and outer layer (see Fig. 5.1). Both components are described by the model discussed in Chapter 4. The inner component and the outer component (also called *sheath*) are characterized by different sets of physical parameters, including different values of the bulk Lorentz factor  $\Gamma_j$ . Thus, the model considered in this chapter represents the developed version of the two-zone spine-sheath model. In this model, the radiative relation between both components is taken into account, i.e the radiation from one components affects the condition in another component. However, the exchange of particles between the components is not included to the model. In contrast to the original spine-sheath model (e.g. Ghisellini et al., 2005), the emission regions are elongated and inhomogeneous.

In analogy to the single component model described in Chapter 4, I start from defining the geometry of the model. The bases of both components of the jet are located at the distance  $z_0 = 0$ . The radii of the components are different. I assume that the radius at the base of the outer component is equal to  $R_{0,o}$  and the inner component is  $R_{0,i}$  (see: Fig. 5.1). The transverse expansion of the jet components in the plasma rest frame is described by the factor  $\rho_n < 1$ , where  $n$  denotes the outer (*o*) or the inner (*i*) component, respectively. Then, the radius of the specific jet component is described by

$$R_n(z) = R_{0,n} + \phi z, \quad (5.1)$$

where the half-opening angle of the jet,  $\phi$  is equal  $\phi \simeq \rho_n/\Gamma_n$ , and  $\Gamma_n$  is the bulk Lorentz factor of the specific jet component. I assume that  $\phi$  is the same for the inner and the outer jet components. Then, I get relation

$$\rho_n \simeq \phi \Gamma_n. \quad (5.2)$$

Note that for this assumption, the jet at a very large distance from the jet base is dominated by the inner component. In fact, the existence of the limb-brightening close to the jet base and the lack of the limb-brightening in a larger distance has been observed in the X-rays for radio galaxy Cen A (Kataoka et al., 2006).

Each component is a source of soft radiation which penetrates another component. This external (from the point of view of a specific jet component) photon field is relativistically boosted due to the difference between the speeds of the jet components. As a result, the energy density of the external photon field can contribute significantly to the total energy density of the low energy photons in a specific jet component. It has an impact on the electron spectrum in a specific jet component and on the observed IC radiation emitted from the jet.

In order to calculate the photon field in the inner (outer) component, which has been produced in the outer (inner) component, I simplify the transverse structure of

the jet. I assume that the whole radiation from the inner component is emitted at the axis of the jet. In case of the outer component, I assume that the radiation is produced at the distance  $R_2(z)$  from the jet axis, which I call the effective radius of the outer component. The effective radius is obtained by the averaging of the outer component radius, i.e.

$$R_2(z) = \frac{\int_{R_i(z)}^{R_o(z)} 2\pi r^2 dr}{\int_{R_i(z)}^{R_o(z)} 2\pi r dr}. \quad (5.3)$$

In case of  $R_i \ll R_o$  it approaches the value  $R_2 \approx 2/3 R_o$ .

Each component is described by a different speed of the plasma. Then, there are two co-moving frames, associated with the inner and the outer jet components. The quantities in the inner component frame are designated by the single primes and the quantities in the outer component by the double primes. In the co-moving frames of the jet components, the plasma conditions change with time. Let's assume that a thin slab of the plasma is injected at the base of the inner component at time  $t'_0 = 0$ . After time  $t'$  (where  $t'$  is the time measured in the frame of the inner component), this slab is located at a distance of  $z' = \beta_i c t'$  from the jet base. In this same way, the distance from the base of the outer component is  $z'' = \beta_o c t''$ .

Let us consider two thin slabs in the co-moving frame of the outer component. The thin slab of the inner component component is located at the distance  $z'_1$ . The thin slab of the outer component is located at the distance  $z''_2$ . Such a system of two slabs is schematically shown in Fig. 5.2. The number density of the low energy photons in the inner component slab at distance  $z'_1$  coming from the component slab at distance  $z''_2$  per unit solid angle,  $\Omega''$ , is given by (Dermer and Schlickeiser, 1993)

$$n_i(\epsilon'', \Omega'', z'_1, z''_2) = \frac{\dot{N}_o(\epsilon'', z''_2)}{4\pi c (L'')^2} \frac{\delta(\mu'' - \mu''_z)}{2\pi}, \quad (5.4)$$

where  $\dot{N}_o(\epsilon'', z''_2)$  is the differential number of photons emitted by the thin slab at distance  $z''_2$  per unit of time,  $L'' = ((\Delta z'')^2 + R_2^2)^{1/2}$ ,  $\Delta z'' = z'_1 - z''_2$  is the distance between the slabs,  $\mu''_z = \cos \theta'' = \Delta z''/L''$  and  $\delta$  is the Dirac delta function. The above formula (Eq. 5.4) is transformed to the co-moving frame of the inner component using the Lorentz invariance,  $n_i(\epsilon, \Omega)/\epsilon^2$  (Rybicki and Lightman, 1986). Then, the differential density of photons coming to the inner slab at  $z'_1$  from the outer component slab at  $z''_2$  in the co-moving frame of the inner component is

$$n_i(\epsilon', \Omega', z'_1, z'_2) = D_i^2 n_i(\epsilon'', \Omega'' z''_1, z''_2), \quad (5.5)$$

where  $D_i = [\Gamma_{io}(1 + \beta_{io}\mu'_z)]^{-1} = [\Gamma_{io}(1 - \beta_{io}\mu''_z)]$  is the relative Doppler factor between inner and outer jet component,  $\Gamma_{io} = \Gamma_i \Gamma_o (1 - \beta_i \beta_o)$  is the relative Lorentz factor between the inner and the outer jet component, and  $\beta_{io} = (1 - \Gamma_{io}^{-2})^{1/2}$ . Note that the angle between direction of photons, coming from the slab in the outer component, and the jet axis,  $\theta''_z = \arccos \mu''_z$ , also changes in the inner component frame. The

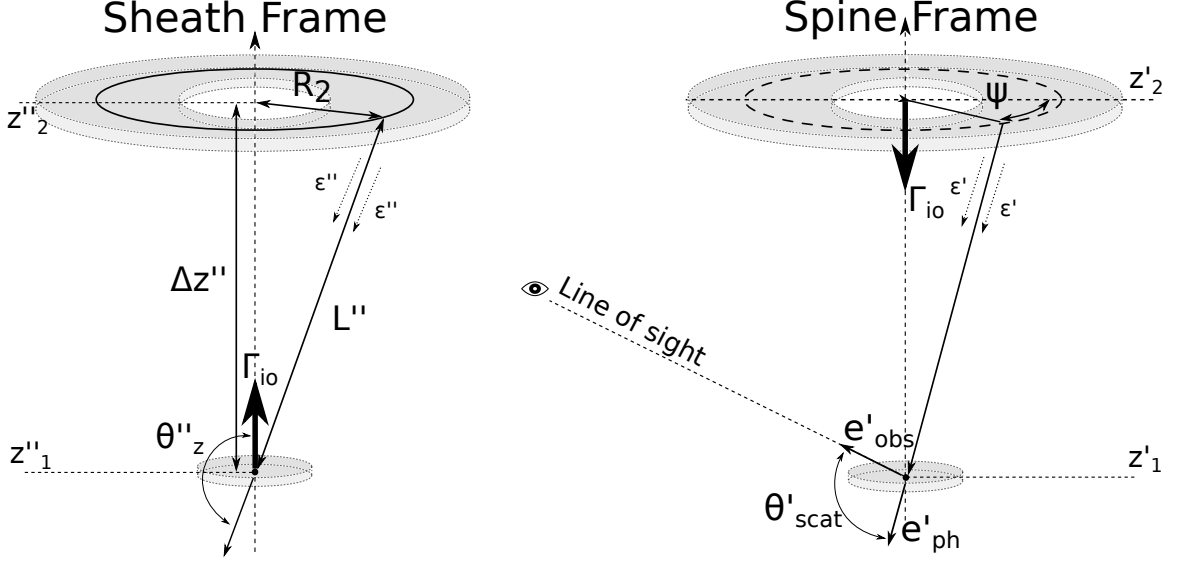


Figure 5.2: The schematic picture of two slabs, in the inner and the outer jet components, with simplified geometry, in the co-moving frame of the plasma in the outer component (left) and in the co-moving frame of the plasma in the inner component (right). It is assumed that all radiation in the outer slab is produced in the circle with radius  $R_2$  and electrons in the inner slab are located at the jet axis. The outer slab at the distance  $z''_2$  emits the synchrotron photons, which arrive at the inner slab located at the distance  $z''_1$  from the jet base. The distance between the slabs is  $\Delta z''$ . The angle between the direction of photons and the jet axis is  $\theta''_z$ . The photons are scattered at the angle  $\theta'_{scat}$  by the electrons in the inner slab. The observer is located at the angle  $\theta_{obs}$  (given by unit vector  $e'_{obs}$ ). The relative Lorentz factor between slabs is  $\Gamma_{io}$ .  $\psi$  is the azimuthal angle. Note that after the change of the frame, the real structure of the slabs can vary greatly in both frames and it is only a schematic picture.

transformation of the cosine of the angle  $\mu''$  from the co-moving frame of the outer component to the co-moving frame of the inner component is given by

$$\mu'_z = \frac{\mu''_z - \beta_{io}}{1 - \beta_{io}\mu''_z}. \quad (5.6)$$

The photons from the outer component (coming to the inner slab at the angle  $\mu'_z$ ) are scattered by the electrons in the inner component. Because electrons in the plasma rest frame are isotropic, I can use the formula for the scattering of directed photon beams on isotropically distributed relativistic electrons derived by Aharonian and Atoyan (1981). Thus, the radiation produced per solid angle  $\Omega_{obs}$  in the inner component by the slab located at the distance  $z'_1$  by scattering photons from the outer component is

$$\dot{n}_{IC}(\epsilon'_1, z'_1, \Omega'_{obs}) = \int_0^{z'_{max}} dz'_2 \int_0^{2\pi} d\psi \int_{\gamma_{min}}^{\gamma_{max}} d\gamma' \int_{\epsilon_{min}} d\epsilon' \times \frac{n_e(\gamma', z'_1)}{(\gamma')^2} \frac{n_i(\epsilon', \Omega', z'_1, z'_2)}{\epsilon'^2} f(\epsilon'_1, \epsilon', \gamma', \mu'_{scat}), \quad (5.7)$$

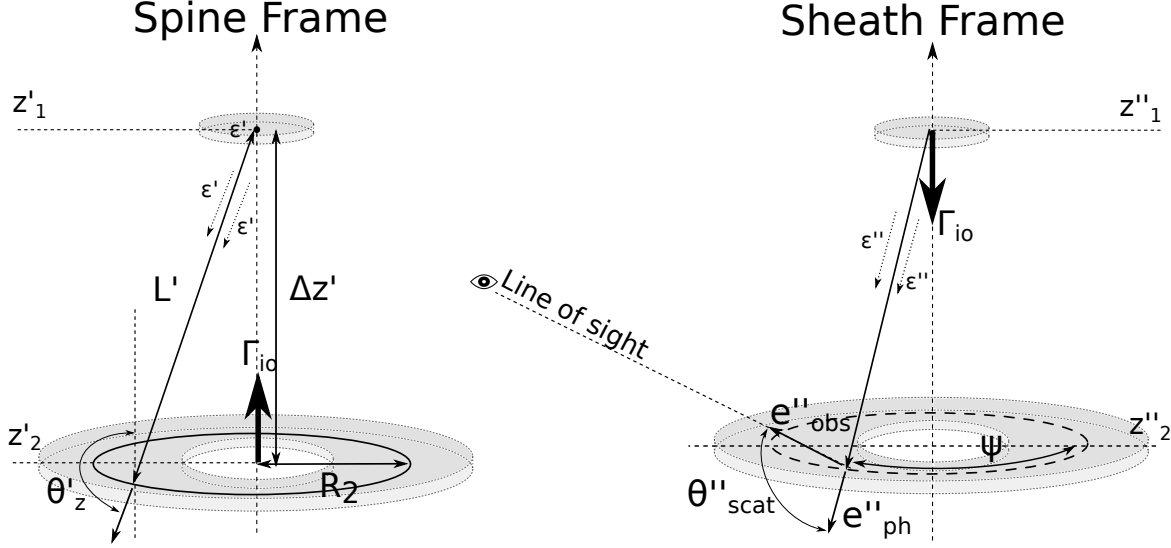


Figure 5.3: The schematic picture of two slabs in the case of scattering of the radiation from the inner component by electrons in the outer component, in the co-moving frame of the plasma in the inner component (left) and in the co-moving frame of the plasma in the outer component (right). It is assumed that all radiation in the inner slab is produced at the jet axis. Electrons in the outer slab are located in the circle with radius  $R_2$ . The inner slab at the distance  $z'_1$  emits photons, which arrive at the outer slab at the distance  $z'_2$ . The distance between slabs is  $\Delta z'$ . The angle between the direction of the photons and the jet axis is  $\theta'_z$ . The photons are scattered at the angle  $\theta''_{scat}$  by the electrons in the outer slab. The observer is located at the angle  $\theta_{obs}$  (given by unit vector  $e''_{obs}$ ). The relative Lorentz factor between slabs is  $\Gamma_{io}$ .  $\psi$  is the azimuthal angle. Note that after the change of the frame, the real structure of the slabs can vary greatly in both frames and it is only a schematic picture.

where  $n_e$  is the differential density of electrons,  $\gamma_{min}$  is obtained from the kinematic condition,  $\psi$  is the azimuthal angle,  $\mu_{scat}$  is the cosine of scattering angle (the angle between the directions of photons before and after the scattering) and  $f(\epsilon'_1, \epsilon', \gamma', \mu'_{scat})$  is given by Eq. 2.22 in Chapter 2.

The unit vector pointing towards the observer is

$$\mathbf{e}'_{obs} = (\sin \theta'_{obs}, 0, \cos \theta'_{obs}) = (\sqrt{1 - (\mu'_{obs})^2}, 0, \mu'_{obs}), \quad (5.8)$$

and the unit vector, which describes the direction of the photons in the co-moving frame of the inner component, is

$$\mathbf{e}'_{ph} = (\sin \theta'_z \cos \psi, \sin \theta'_z \sin \psi, \cos \theta'_z) = (\sqrt{1 - (\mu'_z)^2} \cos \psi, \sqrt{1 - (\mu'_z)^2} \sin \psi, \mu'_z). \quad (5.9)$$

Then, the cosine of scattering angle  $\mu_{scat}$  is given by

$$\mu'_{scat} = \mathbf{e}'_{obs} \cdot \mathbf{e}'_{ph} = \mu'_z \mu'_{obs} + \sqrt{1 - (\mu'_z)^2} \sqrt{1 - (\mu'_{obs})^2} \cos \psi. \quad (5.10)$$

In a similar way, I obtain the density of photons from the inner component in the reference frame of the outer component. However, some formulas differ due to the

different velocity of the jet components and the geometry of the slabs in the outer and the inner jet component (see Fig. 5.3). The density of photons in the outer component at distance  $z'_2$  can be written as

$$n_o(\epsilon', \Omega', z'_2, z'_1) = \frac{\dot{N}_i(\epsilon', z'_1)}{4\pi c(L')^2} \times \delta(\mu' - \mu'_z), \quad (5.11)$$

where  $\dot{N}_i(\epsilon', z'_1)$  is the total number of photons with energy  $\epsilon'$  produced by the slab in the inner component at distance  $z'_1$ . Note, that the density of photons  $n_o$  (given by Eq. 5.11) is larger by factor  $2\pi$  than the density of photons  $n_i$  (given by Eq. 5.4). It is the result of the approximation of the inner slab as a point source, in contrast to the outer-component slab, which is approximated as a ring.

The transformation formula between the co-moving outer component frame and the inner component frame, analogously to Eq. 5.5, is given by

$$n_o(\epsilon'', \Omega'', z''_2, z''_1) = D_o^2 n_o(\epsilon', \Omega', z'_2, z'_1), \quad (5.12)$$

where the Doppler factor in this case is  $D_o = [\Gamma_{io}(1 - \beta_{io}\mu''_z)]^{-1} = [\Gamma_{io}(1 + \beta_{io}\mu'_z)]$  and  $\mu''_z = (\mu'_z + \beta_{io})/(1 + \beta_{io}\mu'_z)$ .

Due to the additional photon field from another jet component, in the total energy loss rate (given by Eq. 4.8) have to be included the cooling process on photons produced in another jet component. Then, the total energy loss rate, in the case of the stratified jet, has to be supplemented by energy loss rate for the inverse Compton scattering on the inner component photons (in the case of the outer component) or the outer component photons (in the case of the inner component).

## 5.2 The equilibrium spectrum of electrons and local density of photons in stratified jet

The calculation of the emission from the stratified jet is much more complex than the calculation of the emission from the sequence of the independent jet components. The radiation from one component affects the cooling processes in every other component. What is more, the radiation from one component is enhanced by the relativistic boosting in the reference frame of the other jet components. Then, the IC cooling process on the external radiation (radiation from other jet components) may exceed other cooling processes. Therefore, the strong exchange of radiation between different jet components has to be taken into account.

To obtain the radiation emitted by the stratified jet, I use the generation method (see Fig. 5.4). Firstly, I model both jet components separately, without the influence of another component. For this purpose, I use the model described in Chapter 4. In this way, I calculate the density of photons from the specific jet component in every place in the jet. This stage of calculations is called the first generation. In the next step, I

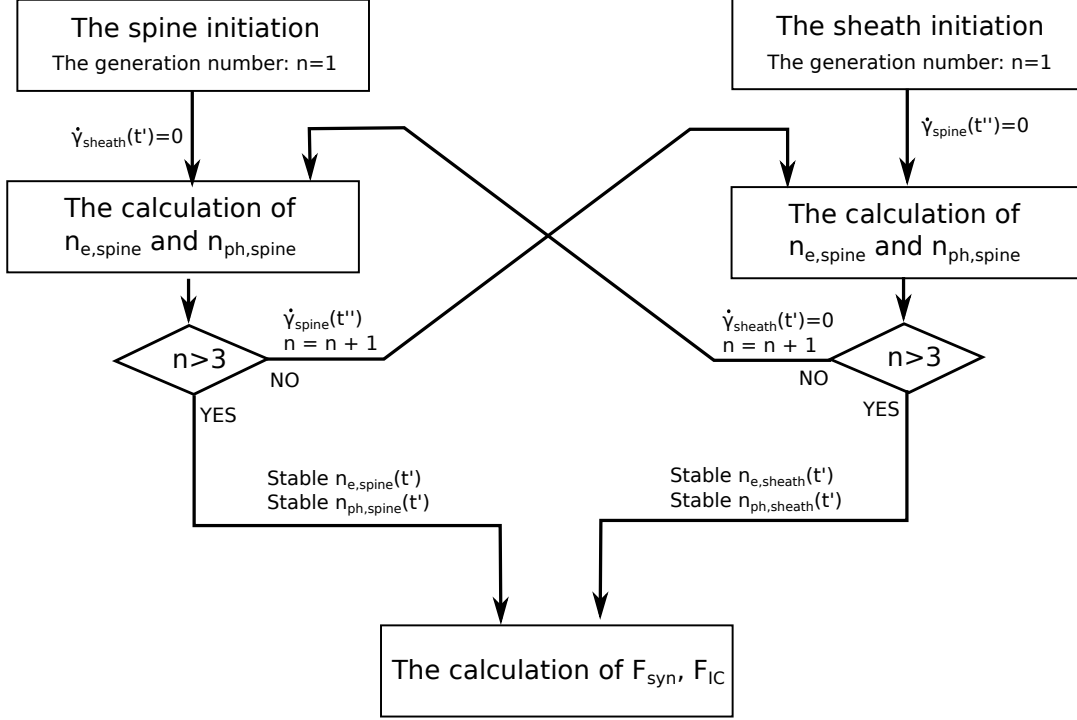


Figure 5.4: Diagram demonstrating the algorithm used to calculate the spectra produced in the self-consistent spine-sheath model of the jet. In the first generation ( $n = 1$ ), the electron distribution ( $n_e$ ) and the photon distribution ( $n_{ph}$ ) are obtained separately in terms of one-component jet model described in Chapter 4 (see Fig. 4.4). In the next generations ( $n > 1$ ), the IC cooling process on external photons is included into the calculations of  $n_e$  and  $n_{ph}$  for the specific jet component. When the conditions in the jet components are stabilized ( $n > 3$ ), then the synchrotron ( $F_{syn}$ ) and the IC ( $F_{IC}$ ) spectra from the jet are calculated.

add the external radiation to the component using the transformation formulas given by Eq. 5.5 and Eq. 5.12. As an example, I show the photon densities of external and internal radiation in the Fig. 5.5. It is assumed that the power injected in relativistic electrons into the outer component is three times greater than the power injected into the inner component, i.e.  $L'_{inj,o} \simeq 3 \times L'_{inj,i}$ . Despite this, the photon density in the inner component is higher due to the smaller radius, i.e.  $R_{0,o} = 3 \times R_{0,i}$  (all model parameters can be found in Table 5.1). Including the relativistic effects between the jet components, the photon field in the outer component is dominated by the radiation from the inner component (in the co-moving frame of the sheath). In the case of the inner component, the external photon density is at the level of the internal density of photons (in the co-moving frame of the inner component). I conclude that in the spine-sheath model, the external radiation dominates the internal radiation at least in one of the two jet components.

When the external photon field is added, I can calculate the second generation of the electron spectra. In the second and later generations, the total energy loss rate,

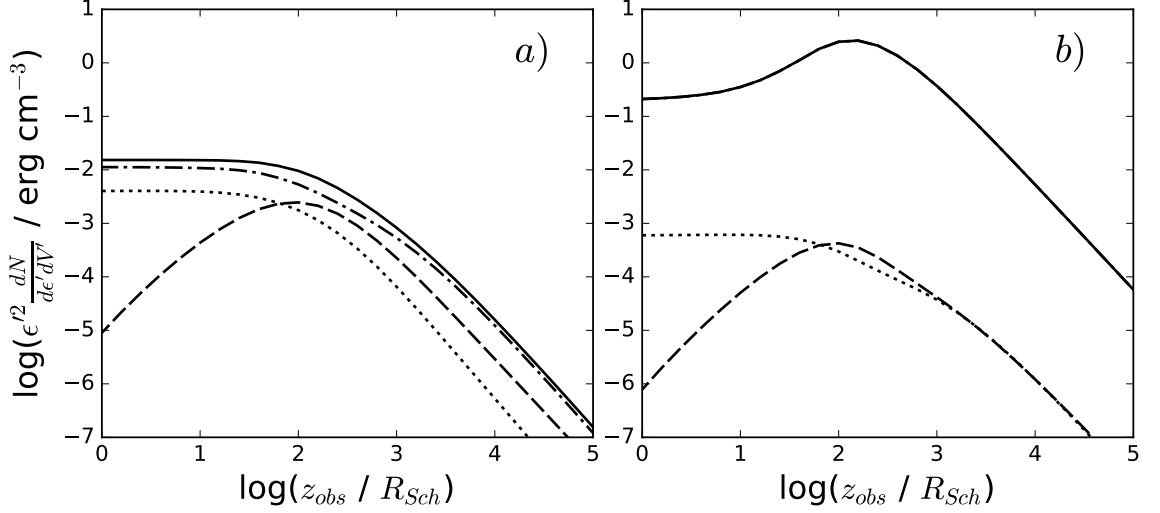


Figure 5.5: The photon density as a function of the distance from the jet base (in the Schwarzschild radius). (a) The density of photons in the inner component (in the co-moving frame of the inner component). (b) The density of photons in the outer component (sheath, in the co-moving frame of the outer component). I show the energy density of the backward photons (dashed line), the forward photons (dotted line), the density of photons from another component (dot-dashed) and the total energy density of photons in a specific jet component (solid line). The parameters of the model are listed in Tab. 5.1.

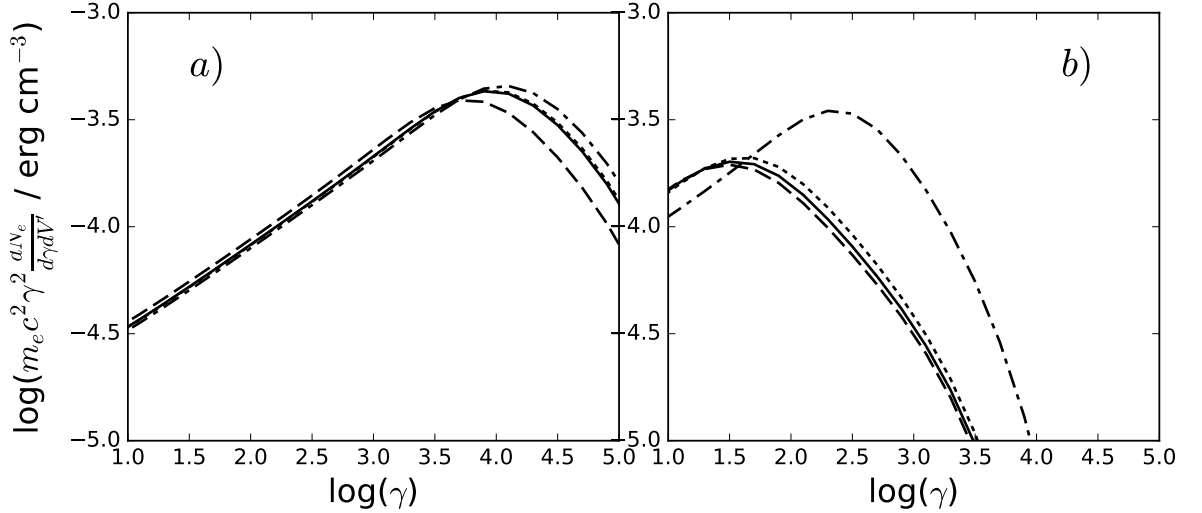


Figure 5.6: The spectrum of the electrons for in the subsequent generations: the first generation (dot-dashed line), the second (dashed), the third (dotted) and the fourth (solid). (a) The electron spectrum in the inner component. (b) The electron spectrum in the outer component. The electron spectra are calculated for the distance  $z_{obs} = 100R_{Sch}$ . The parameters of the model are listed in Tab. 5.1.

$\hat{\gamma}_{tot}$ , includes the synchrotron, the adiabatic, the synchrotron self-Compton, and also the external IC cooling processes. Knowing all the cooling processes occurring in the jet, I can solve the kinetic equation describing the evolution of electrons (given by Eq. 4.10). In such a way, the second generation of the electron spectra is obtained. Other

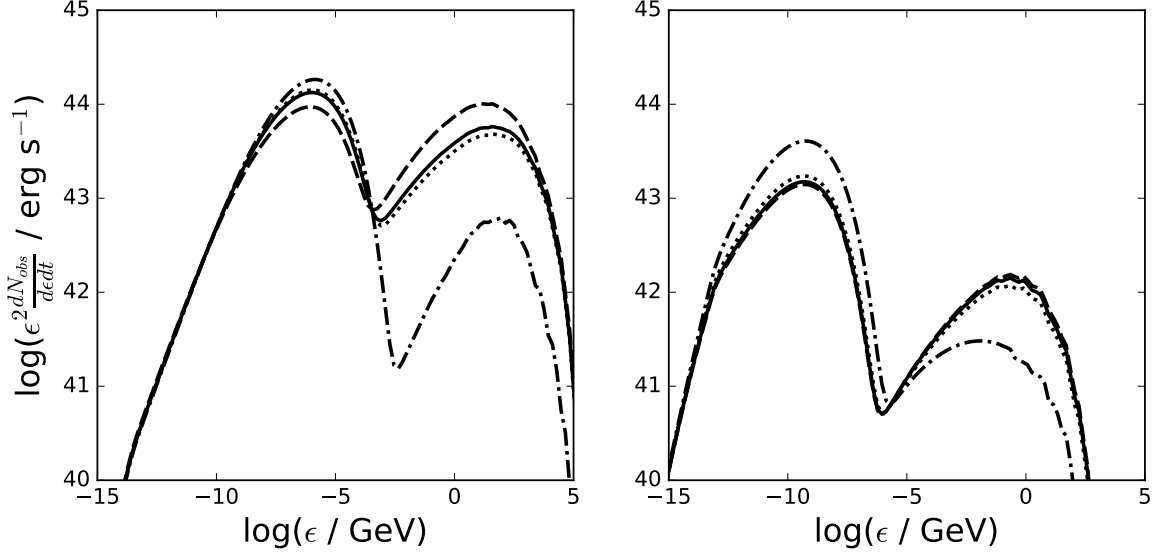


Figure 5.7: SEDs calculated for different generations: the first generation (dot-dashed line), the second (dashed), the third (dotted) and the fourth (solid). The radiation from the inner component (on the left plot) and the radiation from the outer component (on the right). The parameters of the model are listed in Tab. 5.1.

generations are calculated using the external density of photons from the previous generation. In this way, the self-consistent equilibrium spectrum of electrons is reached. In the Fig. 5.6, I show how the electron spectra change in the specific generations. The large differences between the first and the second generations are due to the additional photon fields included in the second generation. With subsequent generations, the differences become smaller. After the fourth generations, the electron spectra in both jet components become stable (see Fig. 5.6). The scheme of the generation method for the calculation of the equilibrium spectra of electrons,  $n_{elec}$ , and photons,  $n_{ph}$ , is shown in Fig. 5.4.

The differences between particular generations are especially visible for the IC radiation emitted by the jet components (see Fig. 5.7). After the first generation, the IC luminosity of the jet increases due to the additional external radiation. Note that the shape of the IC radiation emitted by the component is regulated by the external photon field. After the first generation, the shape of the synchrotron radiation changes. The luminosity of the synchrotron component decreases as a result of the additional IC cooling process on the external radiation. The multiwavelength spectra obtained in specific generations are shown in Fig. 5.7. It may be surprising that the level of the IC radiation from the inner components increase so much in contrast to the IC radiation from the outer component. This effect is caused by the anisotropy of the external radiation. This issue is discussed in more detail in the Section 5.3.2.

## 5.3 Spectra from the whole jet obtained in the spine-sheath model

Below, I investigate the inhomogeneous spine-sheath model. I present SED of the jet for the selected set of the model parameters. I examine the SED for different observation angles.

### 5.3.1 The example of spectral energy distribution obtained with the model

The presented stratified model of the jet assumes that the inner component is immersed in the outer one. Then, the effective cross-section of the outer component is  $\pi(R_o^2 - R_i^2)$ . In order to avoid the influence of the cross-section of the inner component on the outer component, I assume that the cross-section of the inner component is smaller than the cross-section of the outer component. I adopt the value of the radii of the specific jet components at the base at  $30R_{Sch}$  and  $10R_{Sch}$  for the outer and the inner jet component, respectively. Close to the jet base, the cross-section of the inner component is only 11% of the cross-section of the outer one.

For blazars in which the luminosity of the synchrotron component is comparable to the luminosity of the IC one ( $L_{syn} \sim L_{IC}$ ), the energy density of the magnetic field and the energy density of the low energy photons in the emission region should be similar to each other, i.e.  $u'_B \sim u'_{rad}$  (see Eq. 3.9). In the case of the stratified jet, the external radiation is relativistically boosted. Then, the energy density of the low energy photons can be dominated by the external radiation. In such a case, the similar luminosities of both, the synchrotron and the IC, components are achieved for a higher value of the magnetic field, than it is expected in the local SSC model.

The synchrotron peaks in FR I radio galaxies, such as M87, Cen A and NGC 1275, which are detected in VHE  $\gamma$ -rays, are located at  $\sim 1$  eV. Due to the large observation angle, it is reasonable to assume that this synchrotron radiation is produced by the outer component. In terms of the model described in Chapter 4, the peak of the observed synchrotron radiation at  $\sim 1$  eV indicates that the acceleration coefficient,  $\eta$ , is of the order of  $10^{-9}$  (which results from Eq. 2.12 and Eq. 4.7). For such a small value of  $\eta$ , the maximum energy of the electrons is only  $E_{max} \sim 10(B/1 \text{ G})^{-1/2}$  GeV. From the other side, the VHE radiation detected from these objects suggests the existence of electrons with energy  $\sim 1$  TeV. Such large energies of electrons require much more efficient acceleration process (determined by  $\eta$ ). Based on this, I assume that the outer component is characterized by a relatively small acceleration coefficient,  $\eta \sim 10^{-8}$ , in contrast to the inner component which is characterized by  $\eta \sim 10^{-5}$ .

As an example, I chose the acceptable set of parameters which allows to reproduce the typical HBL spectrum for a small observation angle. The half-opening angle of the

Parameter	Symbol	Spine	Sheath	Unit
Mass of the black hole	$M_{BH}$	$10^9$	$10^9$	$M_\odot$
Bulk Lorentz factor of the jet	$\Gamma_j$	9	3	–
Radius of the jet at the base	$R_0$	10	30	$R_{Sch}$
Transverse expansion coefficient	$\rho$	0.6	0.2	–
Magnetic field at the jet base	$B_0$	1	3	G
Index of magnetic field profile	$b$	1	1	–
Power injected in electrons	$L'_{inj}$	$3 \times 10^{41}$	$10^{42}$	erg/s
Index of injection profile	$q$	1	1	–
Spectral index of electrons	$s$	1.6	1.6	–
Acceleration coefficient	$\eta$	$10^{-5}$	$10^{-8}$	–
Minimum energy of electrons	$\gamma_{min}$	1	1	$m_e c^2$
End point of electron acceleration	$z_{end}$	$10^6$	$10^6$	$R_{Sch}$
Observation angle	$\theta_{obs}$	0.1	0.1	rad

Table 5.1: The reference parameters for the spine-sheath model of a jet. In the calculations described in the Chapter 5, I use parameters from this table, unless otherwise noted.

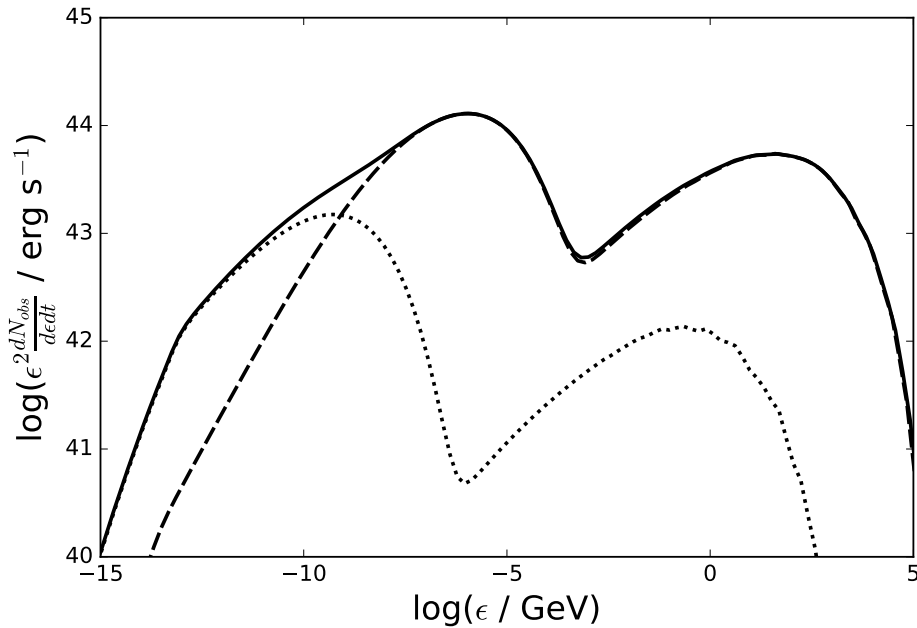


Figure 5.8: SED calculated for the stratified jet for the parameters listed in Table. 5.1, in the observer reference frame. The radiation from the outer layer (dotted line), from the inner component (dashed) and the total radiation emitted by the stratified jet is shown by the solid line.

jet is fixed at  $\phi = 0.07$  rad. According to Eq. 5.2, the  $\rho_i = 0.6$  and  $\rho_o = 0.2$  for  $\Gamma_i = 9$  and  $\Gamma_o = 3$ , respectively. The parameters are listed in Table 5.1. The SED calculated with these parameters is shown in Fig. 5.8.

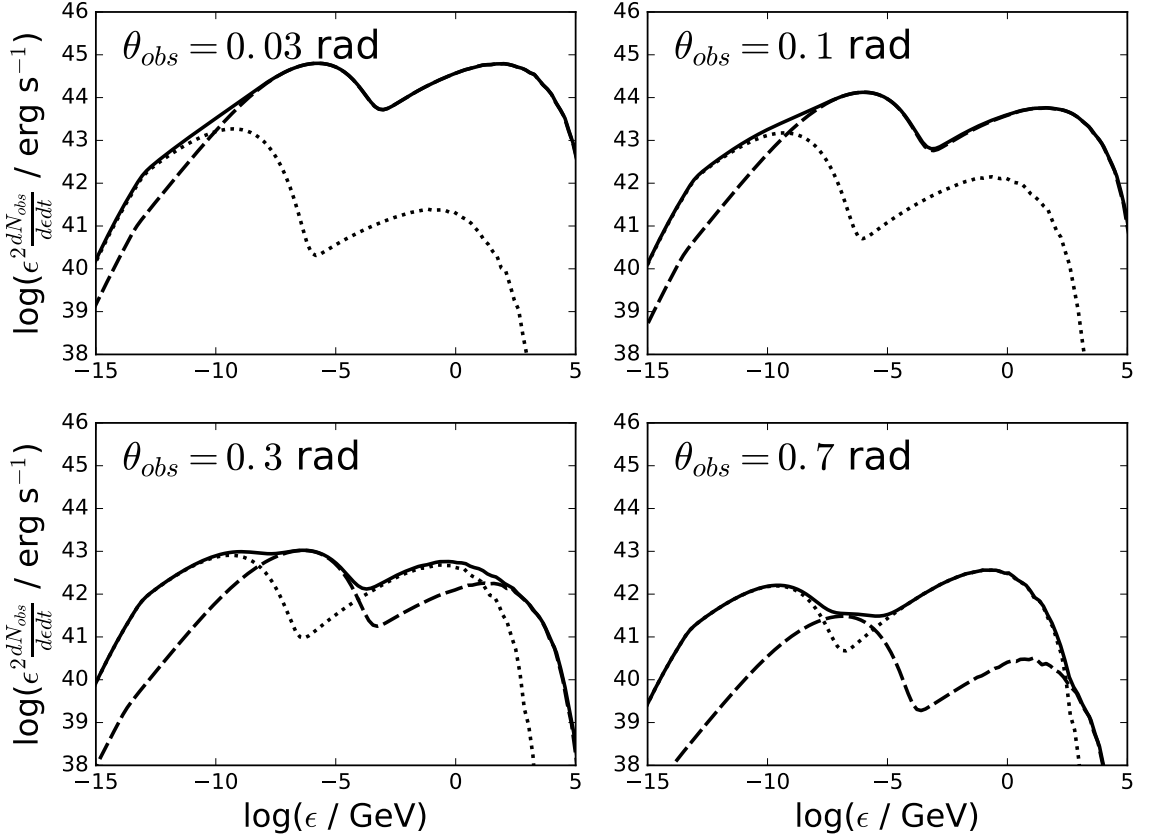


Figure 5.9: SEDs calculated for the stratified jet for the different observation angles (the value of the observation angle is shown on the plot). Specific curves represent radiation emitted by the outer component (dotted), the inner component (dashed) and both jet components (solid). Note that with the increasing of the observation angle,  $\theta_{obs}$ , the ratio between the luminosity of the synchrotron and the IC humps, produced in the specific jet component, changes significantly.

### 5.3.2 Observation angle

The dependence of the observed radiation from the stratified and elongated jet on the observation angle,  $\theta_{obs}$ , is complex due to the anisotropy of the local photon field and different velocities of the jet components. The radiation from the faster, inner jet component is Compton upscattered by the slower, outer layer mainly in the direction opposite to the propagation of the jet due to the Doppler beaming of this radiation. Due to the same effects, the faster component upscatter the radiation from the slower one, mainly in the direction of the jet propagation. Therefore, the parts of the jet described by these same set of parameters emit different spectra depending on the observation angle.

The relation between the observation angle and the emitted SED is shown in Fig. 5.9. The ratio between the synchrotron radiation from the inner and the outer jet components changes with the observation angle due to the Doppler beaming. The synchrotron radiation from the inner component, which moves with the larger Lorentz

factor, decreases much faster with increasing observation angle than the synchrotron radiation from the outer component. Therefore, the radiation from the inner component dominates the SED for small observation angle of the jet, i.e.  $\theta_{obs} < 0.3$  rad. For large  $\theta_{obs}$ , the apparent luminosity of the radiation from the outer layer is much higher.

The noteworthy feature of the spectra calculated in terms of the model is the ratio between the luminosities of the synchrotron and the IC humps. The luminosities of both humps are almost equal in the case of the inner component and small  $\theta_{obs}$ . With increasing observation angle, the synchrotron hump starts to dominate the IC one. For  $\theta_{obs} = 0.7$  rad the luminosity of the synchrotron hump is almost ten times higher than the luminosity of the IC hump (see dashed line in Fig. 5.9). In the case of the outer component, the behavior of the synchrotron and the IC humps is reversed. The luminosity of the IC hump produced by the outer component overcomes the synchrotron hump. This effect drops with the increasing observation angle. For the outer component, this effect is even more visible (see dotted line in Fig. 5.9).

## 5.4 Interpretation of the blazar sequence for HBLs and FRI radio galaxies in spine-sheath model

According to the unification model of the radio loud galaxies (Urry and Padovani, 1995), the BL Lac objects are the counterparts of FR I radio galaxies. Provided that the unification model is correct, the smooth transition between SEDs of BL Lacs and FR I galaxies should be observed depending on the observation angle. Furthermore, the accurate model of AGN jets should be able to reproduce such a transition.

The peaks of radiation in HBLs type of blazars (in  $\epsilon F_\epsilon$  versus  $\epsilon$  plot) are located in the X-rays and in the sub-TeV range. On the other hand, the low energy peaks of the radio galaxies occur in the optical–UV range (Abdo et al., 2009b; Fukazawa et al., 2015). The persistent TeV  $\gamma$ -rays in these objects are not observed or they are seen on a much lower level than the GeV  $\gamma$ -ray emission. It is obvious that the one-zone model is unable to explain simultaneously the SEDs of the HBLs and FR I galaxies. Therefore, I try to reproduce SEDs of HBLs and FR I radio galaxies with the spine-sheath model.

As a reference point, I use the observations of IC 310. This nearby radio galaxy (redshift  $z = 0.0189$ , Bernardi et al., 2002) shows behavior typical for blazars, i.e. rapid variability in X-rays and  $\gamma$ -rays (Aleksić et al., 2014c). The mass of the black hole in IC 310 is estimated on  $M_{BH} \simeq 3 \times 10^8 M_\odot$  (Aleksić et al., 2014b). The observation angle of this misaligned blazar was estimated on 0.18-0.35 rad (Aleksić et al., 2014b). The broadband spectral energy distribution was measured in a quiescent state by Ahnen et al. (2017). The modeling of this spectrum is shown in Fig. 5.10. The parameters of the model are listed in Table 5.2. The jet components are characterized by the Lorentz factor equal to 2 and 6 for the outer and the inner components, respectively. Note also the relatively large value of the magnetic field strength in the comparison to the

Parameter	Symbol	Spine	Sheath	Unit
Mass of the black hole	$M_{BH}$	$3 \times 10^8$	$3 \times 10^8$	$M_{\odot}$
Bulk Lorentz factor of the jet	$\Gamma_j$	6	2	–
Radius of the jet base	$R_0$	3	30	$R_{Sch}$
Transverse expansion coefficient	$\rho$	0.6	0.2	–
Magnetic field at the jet base	$B_0$	7	5	G
Index of magnetic field profile	$b$	1	1	–
Power injected in electrons	$L'_{inj}$	$5.3 \times 10^{41}$	$2.2 \times 10^{41}$	erg/s
Index of injection profile	$q$	0.7	1	–
Spectral index of electrons	$s$	1.6	1.6	–
Acceleration coefficient	$\eta$	$10^{-5}$	$3 \times 10^{-7}$	–
Minimum energy of electrons	$\gamma_{min}$	300	$10^3$	$m_e c^2$

Table 5.2: List of parameters used to fit spectra of the misaligned blazar IC 310.

one-component models of Mrk 421 obtained in Chapter 4.

The radiation produced by the jet in the spine-sheath model for different observation angles are compared with the observed spectra of FR I radio galaxy, 3C 78 (Fukazawa et al., 2015), and with the nearby HBLs, i.e. Mrk 501 (Abdo et al., 2011a) and Mrk 421 (Abdo et al., 2011b). All three sources, together with IC 310, belong to the group of low-luminosity AGNs. In order to compare the results for different observation angles, the calculated spectrum of IC 310 is recalculated for the redshifts corresponding to the mentioned objects, i.e.  $z = 0.029$  for 3C 78,  $z = 0.031$  for Mrk 421 and  $z = 0.033$  for Mrk 501.

The calculated SEDs reproduce characteristic features of the multiwavelength spectra of these two HBLs (such as the peaks energy), for the observation angle  $\theta_{obs} < 0.15$  rad. Also, the characteristic shape of the SED of the radio galaxy 3C 78 (NGC 1218) is reconstructed (see black lines in Fig. 5.10). However, the level of the recalculated spectra of IC 310 is smaller than the level of the spectra observed from 3C 78, Mrk 421 and Mrk 501. It indicates that the jet power or the Lorentz factor of the components in these sources have to be higher than in the case of IC 310. Also the other parameters may be different. For example, the black hole mass in 3C 78 is estimated at  $\sim 10^9 M_{\odot}$  (Bettoni et al., 2003).

In order to precisely compare the shapes of the SEDs calculated for different angles with the measured SEDs of 3C 78, Mrk 421 and Mrk 501, I shift vertically the calculated spectra on the plot (see red lines in in Fig. 5.10). The calculated spectra are raised by factor 4, 8 and 10 in the case of 3C 78, Mrk 421 and Mrk 501, respectively. After these modifications, the calculated spectra fit well to the observer spectra from the considered AGNs. The exemption is Mrk 421 where some differences are noticeable.

The spectra obtained for different angles form *a unification sequence* of the BL Lacs

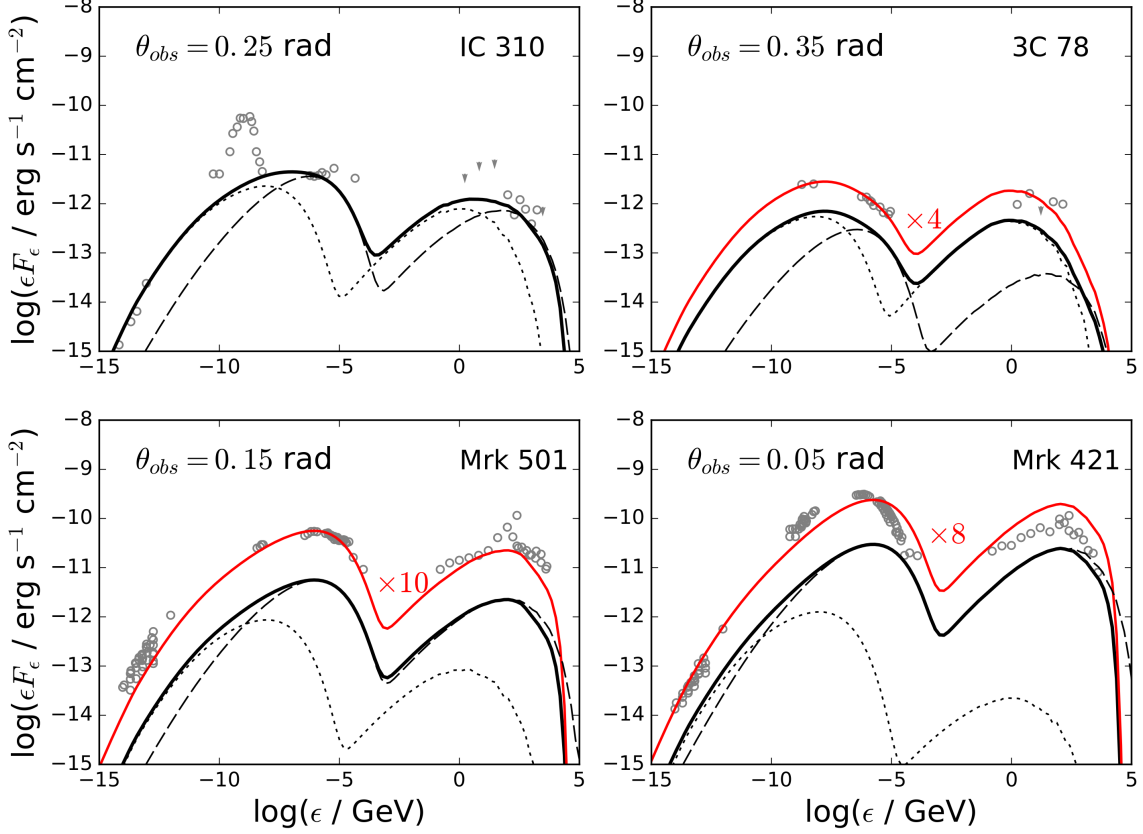


Figure 5.10: The observed SED obtained with the stratified, inhomogeneous and non-local jet model for the different observation angles. The value of the observation angle is reported on the plots. The results of the modelling are compared with the measured SEDs for IC 310 (Ahnen et al., 2017), 3C 78 (Fukazawa et al., 2015), Mrk 501 (Abdo et al., 2011a) and Mrk 421 (Abdo et al., 2011b). Specific figures show SEDs emitted by the inner component (black dashed line), the outer component (black dotted) and the sum of radiation from both jet components (black solid). The SED emitted by both jet components (solid lines) is corrected for the EBL absorption according to Gilmore et al. (2012). For clarity, the obtained spectra of IC 310 in the case of 3C 78, Mrk 421 and Mrk 501 are raised by factor 4, 8 and 10, respectively (red solid lines). The parameters of the model are listed in Tab. 5.2.

with the radio galaxies. They compose smooth transition between the characteristic shapes of spectra for radio galaxies (e.g. 3C 78), through the misaligned blazar (e.g. IC 310) to the HBL (e.g. Mrk 501 and Mrk 421). In terms of this model, for the case of a large observation angles ( $> 0.35$  rad), the IC bump is expected to exceed the synchrotron bump. On the other hand, for a very small observation angles, both bumps should be characterized by hard spectra extended to larger energies (cf. Costamante et al., 2018).

# Chapter 6

## Electromagnetic Cascades in Extended Inhomogeneous Jet

Exceptionally short flares in the X-ray and the  $\gamma$ -ray ranges have been observed from some AGNs. For these events, the variability time scale is close to or even smaller than the light-crossing time of the supermassive black hole (SMBH), which is the smallest physically reasonable size of the emission region. The most extreme examples of such behavior are the flares in PKS 2155-304 (Aharonian et al., 2007), Mrk 501 (Albert et al., 2007) and IC 310 (Aleksić et al., 2014b). The variability time scale can be even shorter than the light crossing time of the black hole horizon when the emission region moves with the relativistic velocity. Then, the observed variability time scale is shorter than the intrinsic variability time scale of the emission region by the Doppler factor,  $D_j$ . This explanation does not work for the radio galaxy IC 310 because it is expected that the Doppler factor for IC 310 is relatively small, i.e. of the order of a few, due to the relatively large observation angle of the jet (Kadler et al., 2012). This fact may indicate that  $\gamma$ -rays are produced in the immediate vicinity of SMBH.

Models of the  $\gamma$ -ray production in the vicinity of a SMBH have been considered by several authors. Such models can be divided into three groups. In the first group, particles are accelerated in the vacuum gap region close to the SMBH. In this model, the particles accelerated in the black hole magnetosphere emit the high energy (HE) radiation analogous to the emission mechanism of the pulsar models (Neronov and Aharonian, 2007; Hirovani et al., 2016). The second group of the models assumes that the emitting particles are accelerated in the magnetic reconnection which occurs close to the jet base where the jet is dominated by the Poynting flux. In the jets-in-a-jet scenario, the extremely fast flares are produced by small blobs of plasma which leave the reconnection site with relativistic velocities in the frame co-moving with the jet. In that case, the bulk Lorentz factor of the emission region can reach a value of the order of 100 (Giannios et al., 2009). In the third group of models, the magnetic reconnection occurs in the magnetic field of the accretion disk or the X-ray corona. Afterward, the accelerated particles streaming along the magnetic field lines emit the very high energy

(VHE) curvature radiation (Bednarek, 1997).

In the case of blazars, where the angle between the jet axis and the line of sight is smaller than the opening angle of the jet, HE  $\gamma$ -rays have to propagate in the radiation field of the jet. They can be absorbed in collisions with low energy photons. As a result,  $e^\pm$  pairs are created. Such  $e^\pm$  pairs produce secondary photons in the IC process which can be also absorbed. In this way, the electromagnetic cascades are developed within the jet volume. If the cascades propagate close to the line of sight and the cooling of leptons is efficient then the observed duration of the cascade (corrected for the relativistic and the geometrical effects) is comparable to the injection time of the primary VHE  $\gamma$ -rays.

In this chapter, I present scenario where a persistent radiation is produced in the extended parsec-scale jet but the flares are caused by VHE  $\gamma$ -rays emitted from the vicinity of the SMBH. These  $\gamma$ -rays have to propagate in the radiation field of the jet. The primary and the secondary  $\gamma$ -rays are absorbed by the radiation produced within an extended jet, initiating IC  $e^\pm$  pair cascades. The persistent emission from the parsec-scale jet is obtained in terms of the non-local, inhomogeneous jet model described in Chapter 4. The HE radiation from the IC  $e^\pm$  pair cascades is calculated by using dedicated Monte Carlo simulations.

## Theoretical description

In the first approximation, the shape of AGNs jets can be well estimated by the truncated cone with the half-opening angle  $\phi$ . When the observer is located at the angle to the jet axis  $\theta_{obs} < \phi$ , then  $\gamma$ -rays produced close to the jet base have to propagate inside the jet volume. Because of the elongated shape of the jet, the propagation path of  $\gamma$ -rays is comparable to the length of the jet. Thus, the probability of the absorption is much higher than for the observer located at  $\theta_{obs} > \phi$ . Then, it is plausible that the jet is optically thick for the HE  $\gamma$ -rays. In such a case, the VHE  $\gamma$ -rays produced close to the jet base are absorbed within the jet before they are able to reach the observer. Absorbed  $\gamma$ -ray photons, with energy  $\epsilon_0$ , create electron-positron pairs with an energy of roughly  $\sim \epsilon_0/2$ . In this way, the population of energetic  $e^\pm$  pairs can appear in the jet region, even if the cooling time scale of such energetic leptons is very short and the local conditions are not favorable for the acceleration of leptons to such large energies.

In the model described in Chapter 4, the radiation is emitted in a large part of the extended jet. Then, the  $e^\pm$  pairs produced in photon-photon absorption process appear in a relatively large volume. They produce secondary radiation close to their place of origin. Then, the emission region of the secondary radiation is also relatively large. However, the observation period of the secondary emission from the cascades is relatively small for small observation angles.

For instance, let me assume that the IC  $e^\pm$  pair cascade in a specific blazar is initiated by VHE  $\gamma$ -rays. These  $\gamma$ -rays are injected into the jet during the very short

period of time,  $\Delta t_{inj}$ . The secondary  $e^\pm$  pairs are created in a part of the jet with the length,  $\Delta z$ . Moreover, the cooling time of the  $e^\pm$  pairs in the place of their creation is also very short. Then, the observed variability time scale of the radiation produced in the  $e^\pm$  pair cascades depends on the observation angle  $\theta_{obs}$ . This variability time scale is approximately equal to  $\Delta t_{obs} \simeq (1 - \cos \theta_{obs}) \Delta z / c$ .

The accurate calculation of the electromagnetic cascades, developing inside the jet volume is a very complicated task. The radiation inside the jet is non-isotropic. The parameters of the jet change with the distance from the jet base. Photons and  $e^\pm$  pairs must be traced in the three dimensions. The conditions in the jet can change with time. Because of all these complications, it is necessary to apply a number of simplifications.

First of all, I limit the problem to the one spatial dimension. I assume that the injected photons move parallel to the jet axis, i.e. the secondary  $e^\pm$  pairs are created at the jet axis. Then, the direction of emitted secondary  $\gamma$ -ray photons also agrees with the direction of the jet axis. Such a simplification is justified by the elongated shape of the jet, in which the local radiation is dominated by photons from the forward and the backward regions of the jet (see Fig. 4.2).

Created  $e^\pm$  pairs appear at some distance  $z_{abs}$  along the jet. They are immediately isotropized by the random component of the magnetic field (in the frame co-moving with the plasma). These pairs are advected with the plasma along the jet axis with the velocity  $\beta_j = (1 - \Gamma_j^{-2})^{1/2}$ , where  $\Gamma_j$  is the bulk Lorentz factor of the jet. These  $e^\pm$  pairs lose energy on the synchrotron and the IC processes. They also emit the secondary  $\gamma$ -ray photons which can be absorbed. I assume that the secondary synchrotron and IC radiation is collimated into a cone with the half-opening angle  $\sim 1/\Gamma_j$ .

The synchrotron and the IC radiation is emitted by the secondary particles produced in the IC  $e^\pm$  pair cascade. This radiation leads to increase the local density of photons in the jet. However, I assume that these additional photons do not affect the absorption and the scattering processes of electrons previously present in the jet. The energy of the secondary  $e^\pm$  pairs is of the order of  $\sim$  TeV. Therefore, the secondary  $e^\pm$  pairs produce the synchrotron radiation in the X-ray range for typical parameters of the jet. For such energies, the IC scattering occurs deeply in the Klein-Nishina regime, where the Compton cross-section is relatively small. Simultaneously, the excess of the X-ray radiation does not lead to a significant increase of the  $\gamma$ -ray absorption. Therefore, slight absorption effects can be safely neglected.

With these simplifications, I calculate the place of absorption of the primary  $\gamma$ -rays, the energy of created  $e^\pm$  pairs, and the energies of the secondary photons emitted by them. The absorption probability of photons with energy,  $\epsilon_0$ , which are injected at the jet base at  $z = z_0$  is

$$p_\gamma(\epsilon_0) = 1 - \exp(-\tau_{\gamma\gamma}(\epsilon_0)), \quad (6.1)$$

where  $\tau_{\gamma\gamma}$  is the optical depth for the  $\gamma$ -rays along the jet axis. When the  $\gamma$ -rays are absorbed, then the place of the absorption is found with the Inverse Transform Method.

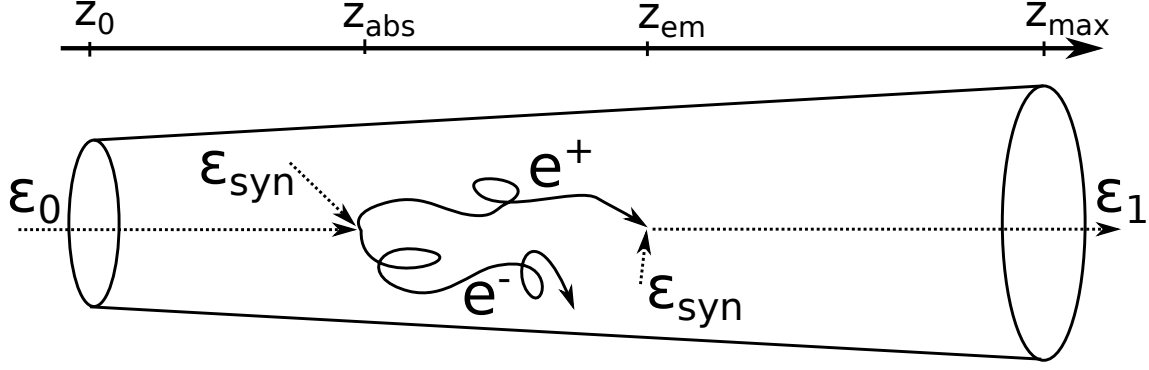


Figure 6.1: The schematic picture of IC  $e^\pm$  cascade in the radiation of the inhomogeneous jet. The primary  $\gamma$ -ray photon,  $\epsilon_0$ , is injected at the jet base located at  $z_0$ . The photon is absorbed in the synchrotron radiation of the inhomogeneous jet. The  $e^\pm$  pair is created as a result of the absorption at distance  $z_{abs}$ . The  $e^\pm$  pair is isotropized in the random magnetic field and advected with the plasma of the jet. The secondary leptons emit the synchrotron photons. The secondary  $\gamma$ -ray photon,  $\epsilon_1$ , is produced at distance  $z_{em}$  as a result of IC scattering process of the secondary particles with the synchrotron radiation. The secondary  $\gamma$ -ray photon,  $\epsilon_1$ , can be also absorbed in the synchrotron radiation of the jet or it can escape from the jet.

The cumulative distribution function (CDF) for absorption at distance  $z_{abs}$  is calculated from

$$F(z_{abs}, \epsilon_0) = \frac{1 - \exp(-\int_{z_0}^{z_{abs}} \alpha_{\gamma\gamma}(z, \epsilon_0) dz)}{1 - \exp(-\tau_{\gamma\gamma}(\epsilon_0))}, \quad (6.2)$$

where  $\alpha_{\gamma\gamma}(z)$  is the absorption coefficient and  $z$  is the distance from the jet base. Afterwards, the absorption place can be found with the inverse function of  $F$  and the random number,  $u$ , from a uniform distribution over  $(0, 1)$ ,

$$z_{abs} = F^{-1}(u). \quad (6.3)$$

The energy of the electron-positron pair can be found with the procedure described in Chapter 2. Firstly, the photons are transferred to the center-of-momentum frame. The  $e^\pm$  pair is created with the equal energies and opposite momentum vector in the center-of-momentum frame. In the last step, the energy of the leptons is transformed to the reference frame. The electron-positron pair is isotropized in the random magnetic field. They lose energy on the synchrotron and the IC processes. The synchrotron and IC cooling in the Thomson regime is subtracted continuously from the electron during its propagation within the jet. However, in the Klein-Nishina regime the electron-positron pair loses energy in the discrete amounts (as shown in Fig. 2.4).

Due to the isotropy of electrons in the co-moving frame of the jet, it is more convenient to consider the emission process in the jet frame. In such a frame, the emission probability of HE photon per unit time,  $dt'$ , in IC process is given by

$$\frac{dp_{em}}{dt'} = \int d\epsilon'_1 \int d\Omega' \int d\epsilon'_{syn} \frac{dN}{dt' d\epsilon'_{syn} d\epsilon'_1 d\Omega'}. \quad (6.4)$$

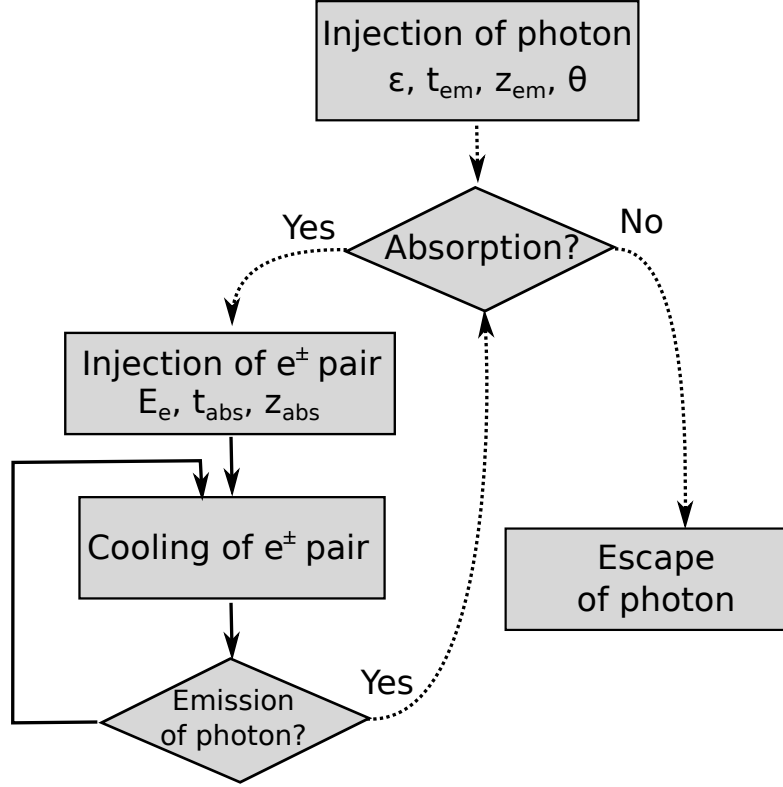


Figure 6.2: Diagram demonstrating the algorithm used to calculate the emission from the IC  $e^\pm$  cascades initiated by VHE  $\gamma$ -rays. The primary VHE  $\gamma$ -rays are injected into the jet. Some of them are absorbed in the radiation field of the jet and produce the  $e^\pm$  pairs. These pairs cool in the jet and produce the secondary HE  $\gamma$ -ray photons. Such photons can also be absorbed in the jet volume. Alternatively, they can escape from the jet. The calculations are continued as long as the energy of the  $e^\pm$  pairs are large enough to produce the HE  $\gamma$ -rays or the  $e^\pm$  pairs do not leave the jet volume (i.e. the position of a lepton is smaller than  $z_{max}$ ).

where  $d\Omega'$  is the solid angle,  $\epsilon'_1$  is the energy of scattered photon in the reference frame of the plasma,  $\epsilon'_{syn}$  is the energy of the synchrotron photons from the inhomogeneous jet and  $dN/dt'd\epsilon'_1d\epsilon'_{syn}d\Omega'$  is the formula for the Compton scattering of directed photons on the isotropically distributed relativistic electrons (given by Eq. 2.22). If the HE photon is emitted, its energy is found with the Inverse Transform Method.

## 6.1 Numerical implementation

The spectra of  $\gamma$ -ray photons emitted in the  $e^\pm$  pair cascade process are calculated with the method illustrated in Fig. 6.2. In the first step, the VHE  $\gamma$ -rays are injected into the jet. They are described by the photon energy,  $\epsilon_0$ , the place of emission,  $z_{em} = 0$  and the time of emission  $t_{em}$  (all in the observer's reference frame). Some of the photons are absorbed within the jet volume. The rest of the photons escape from the jet reaching

the observer. For sources in cosmological distances, the absorption on the EBL must be also included.

The absorbed photons create the electron-positron pairs at the place  $z_{\pm} = z_{abs}$ , the time  $t_{\pm} = z_{abs}/c + t_{em}$  and the energy  $E_{\pm}$ . The  $e^{\pm}$  pairs are isotropized by the random component of the magnetic field of the jet. They are advected with the jet plasma. The  $e^{\pm}$  pairs lose energy continuously on the synchrotron process and on the IC scattering process in the Thomson regime. The HE leptons interact also with the low energy photons in the IC process in the Klein-Nishina regime and lose energy in discrete amounts. The energy of leptons decreases by the amount equal to the energy of the produced HE photon. As a result, the HE photons are emitted. These steps are repeated until a lepton leaves the volume of the jet ( $z_{\pm} > z_{max}$ ) or the energy of a lepton decreases below 100 MeV. After every step,  $\Delta t$ ,  $t_{\pm}$  and  $z_{\pm}$  increases by  $\Delta t$  and  $c\beta_j\Delta t$ , respectively.

The secondary HE photons can also be absorbed in the radiation field of the jet. However, for secondary HE  $\gamma$ -rays, the optical depth for  $\gamma + \gamma \rightarrow e^+ + e^-$  process is smaller because the place of emission is already at some distance from the jet base, i.e.  $z_{em} = z_{\pm}$ . Also the time of emission is delayed compared to the initial photons, i.e.  $t_{em} = t_{\pm}$ .

The photon emitted at the time  $t_{em}$  and at the distance from the jet base  $z_{em}$  is detected by the observer after the period of time equal to

$$t_{obs} = t_{em} - \frac{z_{em}}{c} + \frac{d_L}{c}, \quad (6.5)$$

where  $d_L$  is the luminosity distance to the jet base. I assume here that the observation angle is equal to  $\theta_{obs} = 0$ , i.e. the observer is located at the jet axis.

## 6.2 Intrinsic $\gamma$ -ray opacity for different parameters of the jet

Most often, the geometry of the emission region in blazars is approximated as a spherical blob with the radius obtained from the variability of the source,  $r_{em} \approx 0.5cDt_{var}$ . The optical depth for  $\gamma + \gamma \rightarrow e^+ + e^-$  process,  $\tau_{\gamma\gamma}$ , is proportional to the product of the photon density and the radius of the emission region, i.e.  $\propto n_{ph}r_{em}$ . In the case of the uniformly emitting sphere, the number of non-absorbed photons is proportional to reduction factor  $R$ . The reduction factor of the  $\gamma$ -rays in such a homogeneous sphere is

$$R = \frac{1 - e^{-\tau_{\gamma\gamma}}}{\tau_{\gamma\gamma}}. \quad (6.6)$$

The different situation occurs for an elongated and inhomogeneous jet. In this case, the optical depth depends on the direction and the place of the origin of  $\gamma$ -rays. If a  $\gamma$ -ray is produced close to the jet base and propagates along the jet axis,  $\tau_{\gamma\gamma}$  is

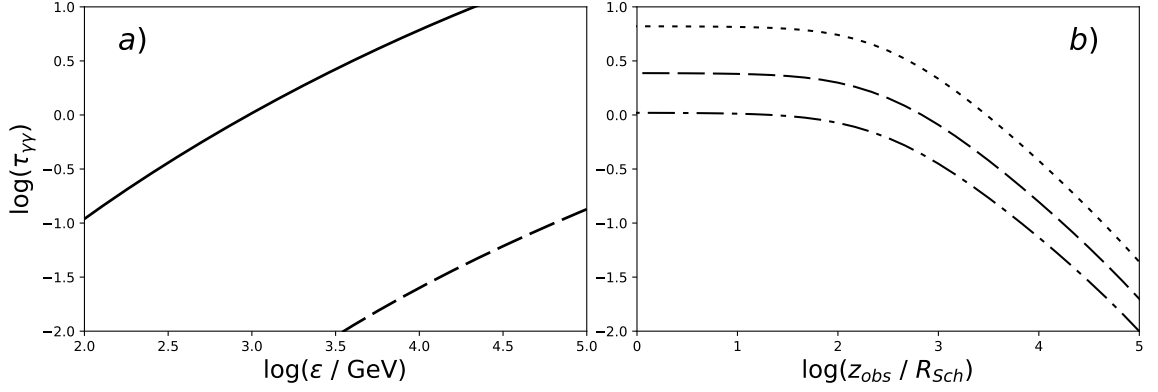


Figure 6.3: (a) The optical depth for the  $\gamma + \gamma \rightarrow e^+ + e^-$  process in the jet described for the parameters of the Model A (solid line) and the Model B (dashed line; see parameters in Table 4.2). (b) The optical depth for the  $\gamma + \gamma \rightarrow e^+ + e^-$  process for the Model A as a function of the injection distance from the jet base for different energies of the primary  $\gamma$ -rays:  $E_\gamma = 1$  TeV (dot-dashed line),  $E_\gamma = 3$  TeV (dashed) and  $E_\gamma = 10$  TeV (dotted).

calculated by integration of absorption coefficient for  $\gamma + \gamma \rightarrow e^+ + e^-$  process during its propagation along the jet,

$$\tau_{\gamma\gamma}(\epsilon; z_{em}) = \int_{z_{em}}^{z_{max}} \alpha_{\gamma\gamma}(\epsilon, z) dz, \quad (6.7)$$

where  $z_{max}$  is the end of the active part of the jet and the absorption coefficient,  $\alpha_{\gamma\gamma}$ , is given by Eq. 2.29. The propagation path for the photon in the case of small observation angle,  $\sim (z_{max} - z_{em})$ , is much larger than the characteristic size of the emission region,  $R_{obs}(z)$ , given by Eq. 4.1. It is expected that in the case of the elongated jet observed at a small angle, the absorption of  $\gamma$ -rays produced close to the jet base can be significant. Especially, the efficient absorption occurs in a jet with a large density of low energy photons. In terms of the inhomogeneous jet model presented in Chapter 4, the condition of the large density of photons is fulfilled for the large power injected in relativistic electrons into the jet, i.e. the large value of  $L'_{inj}$  (see Eq. 4.6). The conditions favorable for the  $\gamma$ -ray absorption also become more extreme when the emission region is small, i.e. for small values of  $R_0$  and  $\rho$  (see Eq. 4.2).

I have calculated the optical depth for two models of the SED of Mrk 421 discussed in Chapter 4 (Model A and Model B in Table 4.2). In the Model A, which is characterized by the low bulk Lorentz factor, the jet is optically thick for photons with energies larger than 1 TeV (see Fig. 6.3a). Model B is optically thin even for VHE  $\gamma$ -rays. I show also the optical depth as a function of distance from the jet base for the  $\gamma$ -rays injected with different energies (see Fig. 6.3b). The optical depth,  $\tau_{\gamma\gamma}$ , is constant in the region close to the jet base. In the outer part of the jet,  $\tau_{\gamma\gamma}$  decreases quickly. However, note that for other values of  $q$  (see Eq. 4.4), the profile of  $\tau_{\gamma\gamma}$  may be different.

## 6.3 Spectra from the cascades for different parameters of the primary VHE photons

### 6.3.1 Injection of the monoenergetic VHE $\gamma$ -rays

As an example, I consider the injection of the primary  $\gamma$ -rays with the monoenergetic distribution into the jet described by the parameters of the Model A (see Table 4.2). The photons with energies  $\epsilon_0$  and with a direction parallel to the jet axis are injected at the jet base. The injected photons are partially absorbed initiating the IC  $e^\pm$  cascades. The spectra of the secondary photons are presented in Fig. 6.4. The calculations are performed for four different energies of the primary photons: 3 TeV, 10 TeV, 30 TeV and 100 TeV. The injected power in the primary photons is equal to  $L_\gamma = 10^{42}$  erg/s in the observer's frame. The primary  $\gamma$ -rays are injected during the period of time equal to  $\Delta t_{inj} = 3 \times 10^3$  s.

The shape of the  $\gamma$ -ray spectrum is similar for all considered energies of the primary  $\gamma$ -ray photons. However, the levels of the spectra are inversely proportional to the energy of the primary photons. The primary  $\gamma$ -ray photons with higher energies produce more energetic  $e^\pm$  pairs. Leptons with high energies lose more energy in the synchrotron process than in the IC process. Deep in the Klein-Nishina regime, the energy loss rate for the IC process increases only logarithmically with increasing energy of electrons, whereas the synchrotron energy loss rate increases with the square of the electron's energy.

For the jet parameters used in the calculations, the optical depth of  $\gamma$ -rays in the jet radiation field is equal to unity for photons with energies close to  $\epsilon_{tr} = 1$  TeV (see the grey line in Fig. 6.4b). For all considered energies of the primary  $\gamma$ -rays, the secondary  $\gamma$ -ray spectrum has a peak below the threshold energy,  $\epsilon_{tr}$ . Above this energy, the spectra have sharp cut-offs.

The synchrotron spectra from the cascades initiated by the monoenergetic photons are shown in Fig. 6.4a. The synchrotron peak depends on the initial energy of  $\gamma$ -rays,  $\epsilon_0$ . The energy of the peak is determined by Eq. 2.12 in which the energy of electrons can be approximated by a half of the energy of the initial  $\gamma$ -ray photons. The luminosity of the synchrotron radiation is roughly the same for different energies of the primary  $\gamma$ -ray photons because the synchrotron cooling process dominates in the jet, especially for the VHE electrons.

The time scale for the development of the cascade observed at a very small angle is comparable to the period of the injection of the primary VHE photons. Two light curves for the secondary emission from the  $e^\pm$  cascades are shown in Fig. 6.5. The light curves are calculated for the two initial energies of the primary  $\gamma$ -ray photons, i.e.  $\epsilon_0 = 3$  TeV (Fig. 6.5a) and  $E\epsilon_0 = 30$  TeV (Fig. 6.5b). All the light curves have the peaks at the end of the injection period. After the injection phase, the energy of the

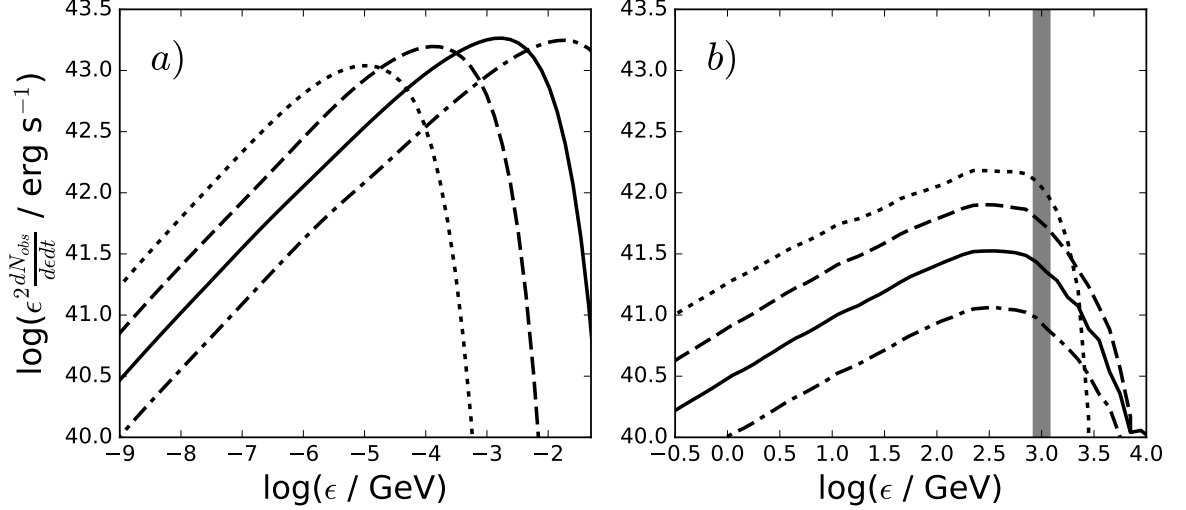


Figure 6.4: The secondary synchrotron (a) and  $\gamma$ -ray (b) spectra produced in the IC  $e^\pm$  pair cascades propagating within the jet and initiated by the mono-energetic primary  $\gamma$ -rays. The energies of the primary  $\gamma$ -rays are:  $\epsilon_0 = 3$  TeV (dotted line),  $\epsilon_0 = 10$  TeV (dashed),  $\epsilon_0 = 30$  TeV (solid) and  $\epsilon_0 = 100$  TeV (dot-dashed). The thick grey line, on the plot (b), shows the energy for which  $\tau_{\gamma\gamma} = 1$  at the base of the jet. In every case the the power injected in primary  $\gamma$ -rays into the jet is  $L_\gamma = 10^{42}$  erg/s. The parameters of the model are listed in Table 4.2 (Model A).

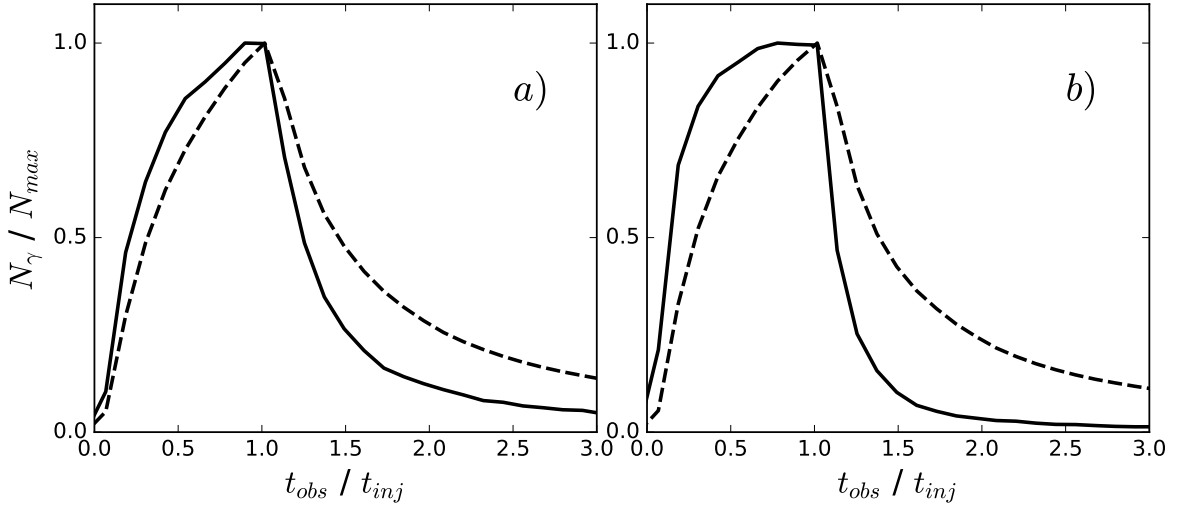


Figure 6.5: The light curves of the secondary  $\gamma$ -ray radiation from the IC  $e^\pm$  pair cascade for two energies of the initial photons:  $\epsilon_0 = 3$  TeV (a) and  $\epsilon_0 = 30$  TeV (b). The light curves shows the  $\gamma$ -ray fluxes above 100 GeV (the energies of  $\gamma$ -rays characteristic for the IACTs, solid line) and between 100 MeV and 300 GeV (the energies of  $\gamma$ -rays characteristic for the *Fermi* LAT telescope, dashes line). Both light curves are normalized to the peak in the photon distribution,  $N_\gamma$ . The parameters of the jet are listed in Table 4.2 (Model A).

emitting  $\gamma$ -rays decreases as a result of the cooling of  $e^\pm$  pairs.

The SEDs of the secondary  $\gamma$ -ray emission from the cascades for different epochs are shown in Fig. 6.6. This figure shows the evolution of the secondary emission produced

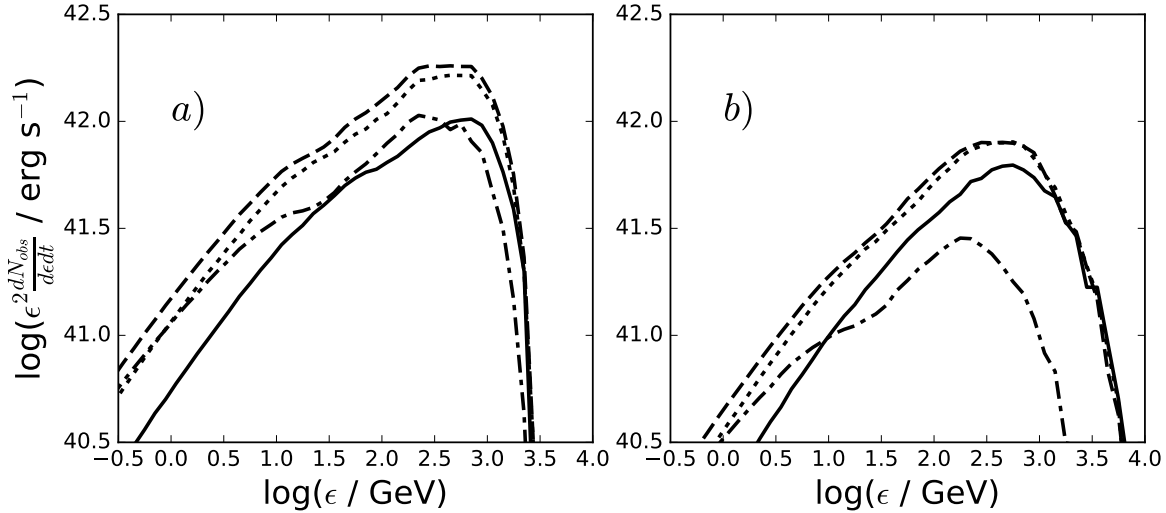


Figure 6.6: The  $\gamma$ -ray spectra produced in the IC  $e^\pm$  cascades which propagate within the jet. The energy of initial photons are  $\epsilon_0 = 3$  TeV (a) and  $\epsilon_0 = 10$  TeV (b). The power injected in the primary  $\gamma$ -rays is  $L_\gamma = 10^{42}$  erg/s. The injection period of the primary  $\gamma$ -rays is  $\Delta t_{inj} = 3 \times 10^3$  s. The lines represent different epochs after the beginning of the flare:  $0 < t < \Delta t_{inj}/3$  (solid line),  $\Delta t_{inj}/3 < t < 2\Delta t_{inj}/3$  (dotted),  $2\Delta t_{inj}/3 < t < \Delta t_{inj}$  (dashed) and  $\Delta t_{inj} < t < 4\Delta t_{inj}/3$  (dot-dashed). The parameters of the model are listed in Table 4.2 (Model A).

in the IC  $e^\pm$  cascades with time. After the injection period, the peak of the  $\gamma$ -ray spectrum is shifted to lower energies and the spectrum decreases as a result of the electron cooling.

### 6.3.2 Injection of VHE $\gamma$ -rays with the power-law distribution

As a second example, I examine the case of the injection of the primary  $\gamma$ -rays described by the power law spectrum. I assume that the energies of the primary photons ranges from  $\epsilon_{min} = 100$  MeV to  $\epsilon_{max} = 10$  TeV. The different spectral indices of the primary photons are considered in Fig. 6.7. The power injected into the jet in the form of the primary  $\gamma$ -ray photons is  $L_\gamma = 10^{42}$  erg/s. As in the previous section, the jet is described by the Model A (see Chapter 4). For this model, the energy threshold for the absorption of  $\gamma$ -rays is  $\epsilon_{tr} = 1$  TeV. The synchrotron and the IC spectra of the secondary emission from the cascades are shown in Fig. 6.7a and Fig. 6.7b, respectively.

The secondary synchrotron radiation changes slightly for different spectral indices. Only the part of the spectrum close to the peak depends on the spectral index. The secondary  $\gamma$ -ray IC spectrum is almost independent on the spectral index of the primary  $\gamma$ -rays. The location of the peak of the secondary IC spectrum is smaller than the threshold energy,  $\epsilon_{tr}$ . The IC spectrum at low energies is described by the power law with the spectral index close to -1.5. I conclude that the value of the spectral index of primary  $\gamma$ -rays does not affect the shape of the secondary spectrum from the IC  $e^\pm$

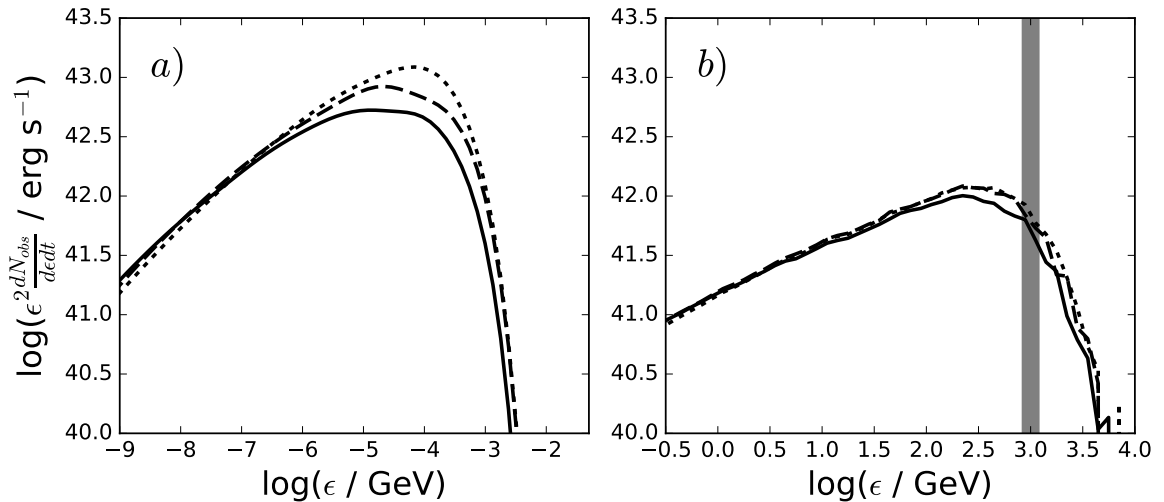


Figure 6.7: The secondary synchrotron (a) and  $\gamma$ -ray (b) spectra produced in the IC  $e^\pm$  cascades propagating within the jet. The spectrum of the primary  $\gamma$ -rays is described by the power law with the spectral index equal to:  $s = 1.0$  (dotted line),  $s = 1.3$  (dashed) and  $s = 1.6$  (solid). This spectrum is defined in the range from  $\epsilon_{min} = 100$  MeV to  $\epsilon_{max} = 10$  TeV. In every case the same power in primary  $\gamma$ -rays has been injected into the jet, equal to  $L_\gamma = 10^{42}$  erg/s. The parameters of the model are listed in Table 4.2 (Model A).

cascades in the jet.

## 6.4 Application of the $e^\pm$ cascade-inside-jet model to blazars

The excess of the hard X-rays in the nearby BL Lac objects has been recently reported by Kataoka and Stawarz (2016) and Madejski et al. (2016) for Mrk 421 and PKS2155-304, respectively. In the X-ray band, the high energy part of the spectrum (between 10 and 50 keV) shows a concave shape. The concave and variable hard X-rays are also observed in case of LBLs (Giommi et al., 1999; Tagliaferri et al., 2000). The excess in Mrk 421 has been observed during two of four observations within a few days. It indicates that this excess is characterized by the relatively fast variability time scale,  $t_{var} \sim 1$  week. In this section, I propose that the observed excess in Mrk 421 is caused by the synchrotron radiation emitted by the  $e^\pm$  pairs from IC  $e^\pm$  cascades in the jet. These cascades are initiated by the VHE  $\gamma$ -rays from the vicinity of the SMBH. In the modeling, I assume that the primary  $\gamma$ -rays are described by power-law spectrum with a single spectral index. I adopt the spectral index recently measured in the case of the of the TeV flare of misaligned blazar IC 310 which is equal to 1.8 (Aleksić et al., 2014b). The flare observed in this source is expected to originate close to the SMBH.

In the first step, I model the broad-band spectrum of Mrk 421 using the non-local inhomogeneous model described in Chapter 4. The calculated spectrum fits very well to

Parameter	Symbol	56302 MJD	Unit
Mass of the black hole	$M_{BH}$	$3 \times 10^8$	$M_{\odot}$
Bulk Lorentz factor of the jet	$\Gamma_j$	6	–
Radius of the jet at the base	$R_0$	10	$R_{Sch}$
Transverse expansion coefficient	$\rho$	0.2	–
Magnetic field at the jet base	$B_0$	3.5	G
Index of magnetic field profile	$b$	1	–
Power injected in electrons	$L'_{inj}$	$1.1 \times 10^{42}$	erg/s
Index of injection profile	$q$	0.8	–
Spectral index of electrons	$s$	1.5	–
Acceleration coefficient	$\eta$	$1.5 \times 10^{-7}$	–
Minimum energy of electrons	$\gamma_{min}$	$2 \times 10^3$	$m_e c^2$
End point of electron acceleration	$z_{end}$	$10^6$	$R_{Sch}$
Observation angle	$\theta_{obs}$	0.033	rad

Table 6.1: The parameters of the non-local inhomogeneous model of the stationary jet which describe the observed SED of Mrk 421.

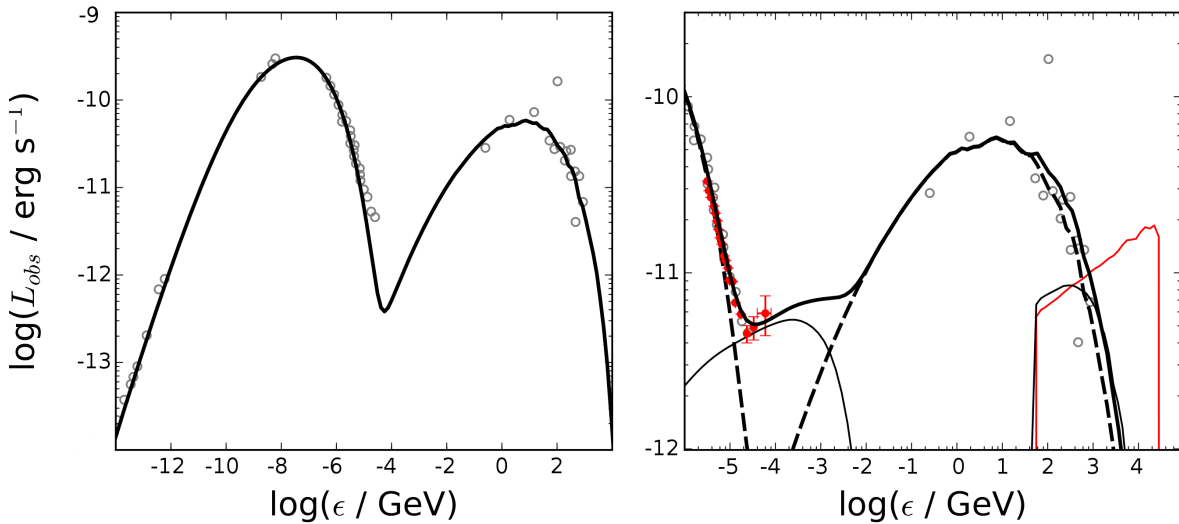


Figure 6.8: (Left) The SED of Mrk 421 during observations at 56302 MJD (data from Baloković et al. (2016)). The black solid line is obtained with the non-local inhomogeneous jet model described in Chapter 4. The parameters of the model are listed in Table 6.1. (Right) X-ray and  $\gamma$ -ray spectrum of Mrk 421 with the visible excess at hard X-rays (red circles, data from Kataoka and Stawarz, 2016). The primary  $\gamma$ -rays are injected into the jet (thin solid red line) with the spectrum observed during the flare in misaligned blazar IC 310 (Eisenacher Glawion et al., 2015). The secondary emission from the cascades is shown with the thin black lines. The emission from the extended jet is presented with the dashed line. The thick black line represents the total emission from the jet.

the spectrum observed in the campaign in 2013 dedicated to Mrk 421 (Baloković et al., 2016). During this campaign, Mrk 421 was in a low activity state and the hard X-ray excess was observed. The data has been well fitted by the non-local inhomogeneous jet model with the parameters described in Table 6.1. The calculated SED is presented in Fig. 6.8 (on the left). The opacity threshold, i.e.  $\tau_{\gamma\gamma} = 1$ , occurs for the primary  $\gamma$ -ray photons with energies equal to  $\epsilon_{tr} \simeq 2$  TeV. If the  $\gamma$ -rays with higher energies are injected into the jet, then the  $e^\pm$  pairs from the IC cascades have to appear in the volume of the jet.

The quiescent spectrum of the jet, modified by the radiation from the  $e^\pm$  cascades, is shown in Fig. 6.8 (on the right). The additional component associated with the synchrotron radiation produced in the IC  $e^\pm$  cascades appears at the keV-MeV energy range. The level of the secondary  $\gamma$ -ray flux from the cascades is much smaller than the flux of the IC radiation from the inhomogeneous jet due to smaller losses on the Compton process in the Klein-Nishina regime. The spectrum of the primary VHE  $\gamma$ -rays is described by the power law with the spectral index,  $s = 1.8$ . The lower and the upper cutoffs of the spectrum is equal to  $\epsilon_{min} = 100$  GeV and  $\epsilon_{max} = 30$  TeV, respectively. Such spectral index and cutoffs in the spectrum agree with the spectrum observed from IC 310 (Eisenacher Glawion et al., 2015). The total power injected in the primary VHE photons is  $P_\gamma = 4.1 \times 10^{42}$  erg/s. The primary  $\gamma$ -ray photons are injected into the jet during the injection period equal to  $\Delta t_{inj} = 3 \times 10^4$  s.



# Chapter 7

## Summary and Conclusions

In this thesis, I discussed the non-thermal emission from jets in AGNs. In the first part, I described the phenomenon of AGNs. The description of an AGN has been confronted with a typical galaxy. I presented the main facts about the history of AGN studies. Further, the main components of AGN were characterized, with special attention to the jets in AGNs. All of this was described in Chapter 1. Chapter 2 focused on the parsec-scale jets in AGNs. I summarized the information about the geometry and motion of the plasma in the parsec-scale jets. I also introduced the acceleration processes and the main leptonic radiative processes which may occur in jets. In Chapter 3, I reviewed the models of emission from AGNs. The models are divided into two groups depending on particles responsible for the emission. I also describe the general estimations of the conditions in the emission region of the parsec-scale jet. In further part of the thesis, I present the results of the jet modeling with inhomogeneous models.

### **The stationary non-local inhomogeneous jet model**

In Chapter 4, I developed the non-local inhomogeneous emission model of the jet. In this model, the majority of radiation is produced in the extended part of the parsec-scale jet. The local photon field, at a specific distance from the jet base, contains photons from different parts of the jet (see Fig. 4.2.) Due to the elongated shape of the emission region, the photons in the jet has anisotropic distribution. This anisotropy of radiation, due to its non-local production, is taken into account in the model during the calculation of IC process. For this reason, different regions of the jet are interpreted. I include this interdependency in the model by using the generation method (see Fig. 4.4). Every generation of calculations takes into account the jet conditions from the previous generation. In this way, the stationary states of the distributions of electrons and low-energy photons are obtained.

The parameters in the jet change with the distance from the jet base. I assumed that the basic parameters of the jet, such as the cross-section of the jet, the strength of the magnetic field and the power injected in relativistic electrons, are described by a power-

law functions dependent on the distance from the jet base,  $z$ . They change substantially along the jet. However, the conditions inside the jet, such as the local distribution of the electrons, the local density of photons and the efficiency of the cooling processes, are calculated self-consistently. The photon spectra obtained in terms of this model has been examined for the wide range of the parameters in Chapter 4.4.

The necessity of using the stationary inhomogeneous model arises from the observations of persistent, low-activity states of jets in AGNs. Note that for the time scale of the order of a month, the emission region moves by a few parsecs. Then, the parameters in the emission region should change significantly. I applied the model to the nearby BL Lac object Mrk 421 (see Chapter 4.5). This object has been observed in the low-activity state by the long-term campaign in 2009 (Abdo et al., 2011b). I reproduced the SED measured during this observation with two sets of the model parameters. In one case (see Model B, Table 4.2), the model was characterized by a large value of the Lorentz factor ( $\Gamma_j = 30$ ) and small value of the strength of the magnetic field ( $B_0 = 0.27$  G). Such values of these parameters are commonly used in modeling of Mrk 421. Alternatively, I modeled the jet with the second set of parameters in which the bulk Lorentz factor is small,  $\Gamma_j = 5$  (see Model A, Table 4.2). Such small value of the Lorentz factor is consistent with radio observations of jets in TeV BL Lacs.

## Stationary stratified jet model

Based on the model considered in Chapter 4, I developed the two-component synchrotron self-Compton model of the jet. In this model, fast-moving plasma located close to the jet axis (the spine) is surrounded by slower moving plasma at the edge of the jet (sheath). Such a model of the jet, called the spine-sheath jet model, is motivated by a number of theoretical and observational indications, such as, for example, the limb-brightening of AGN jets. The model was described in detail in Chapter 5.

The radiation from one of the jet components is relativistically enhanced in the reference frame of the second jet component. Then, the IC processes occurring in the specific jet component depends on the conditions in the second component. Due to the strong interrelations between both jet components, I used the generation method in order to obtain the steady-state conditions in the jet. In the first generation, I independently calculate the jet components, i.e. the inner spine and the outer layer. In the further generations, I included the impact of another component on the IC process in the specific jet component. In this way, I obtain self-consistently the electron and photon spectra (see Fig. 5.4).

I applied the model to the observed SED from the misaligned blazar IC 310 (see Fig. 5.10). I have shown that the spectra calculated for different angles to the jet axis yields the typical SED features of blazars. When the observation angle is small, the calculated spectra are consistent with observations of HBLs e.g. Mrk 501, Mrk 421. On the other hand, the spectra calculated for a large observation angle are compatible

with SEDs from radio galaxies, e.g. 3C 78. Such a result agrees with the unification model of the jetted AGNs, in which blazars are the counterparts of FR I radio galaxies observed at small angles.

## **Electromagnetic cascades in extended inhomogeneous jet**

Some models of the  $\gamma$ -ray production in AGNs predict that the radiation is produced close to the jet base. They are motivated by extremely fast flares observed in blazars and radio galaxies. However, in the case of blazars, which are aligned towards the observer, the  $\gamma$ -ray radiation, before reaching the observer, should pass by the jet volume. Such  $\gamma$ -rays may be absorbed in the low-energy radiation produced in the jet. Absorbed photons can produce the high energy  $e^\pm$  pairs. In this way, the IC  $e^\pm$  pair cascades can be initiated in the volume of the jet. Such a scenario was considered in Chapter 6.

To calculate the photon density and the absorption coefficient for  $\gamma + \gamma \rightarrow e^- + e^+$  process, I used the model described in Chapter 4. I showed that for specific parameters, the jet is optically thick for photons with energy  $\sim 1$  TeV. Then, the high energy  $\gamma$ -ray photons, passing the jet volume, can be absorbed initiating the IC  $e^\pm$  cascades. I examined the secondary radiation produced by the cascades for different forms of injected primary  $\gamma$ -rays (see Chapter 6.3).

The model has been successfully applied to the nearby BL Lac object, Mrk 421. The multiwavelength SED of Mrk 421 has been obtained with the model of the stationary jet from Chapter 4. The observed excess in the hard X-rays, difficult to explain with one-component models, has been modeled with the IC  $e^\pm$  cascades developed in the jet (see Fig. 6.8). For the injection spectrum of primary  $\gamma$ -rays, I used the spectrum observed in the misaligned blazar IC 310, which is interpreted in terms of the model of  $\gamma$ -ray production close to the SMBH. Such a scenario can explain the observed excess in the hard X-rays in blazars.



# Bibliography

- A. A. Abdo, M. Ackermann, M. Ajello, et al. Fermi Discovery of Gamma-ray Emission from NGC 1275. *ApJ*, 699:31–39, July 2009a.
- A. A. Abdo, M. Ackermann, M. Ajello, et al. Fermi Large Area Telescope Gamma-Ray Detection of the Radio Galaxy M87. *ApJ*, 707:55–60, December 2009b.
- A. A. Abdo, M. Ackermann, M. Ajello, et al. Insights into the High-energy  $\gamma$ -ray Emission of Markarian 501 from Extensive Multifrequency Observations in the Fermi Era. *ApJ*, 727:129, February 2011a.
- A. A. Abdo, M. Ackermann, M. Ajello, et al. Fermi Large Area Telescope Observations of Markarian 421: The Missing Piece of its Spectral Energy Distribution. *ApJ*, 736:131, August 2011b.
- M. A. Abramowicz and P. C. Fragile. Foundations of Black Hole Accretion Disk Theory. *Living Reviews in Relativity*, 16:1, January 2013.
- A. Abramowski, F. Acero, F. Aharonian, et al. Measurement of the extragalactic background light imprint on the spectra of the brightest blazars observed with H.E.S.S. *A&A*, 550:A4, February 2013.
- M. Ackermann, M. Ajello, W. B. Atwood, et al. The Third Catalog of Active Galactic Nuclei Detected by the Fermi Large Area Telescope. *ApJ*, 810:14, September 2015.
- F. Aharonian, A. G. Akhperjanian, A. R. Bazer-Bachi, et al. An Exceptional Very High Energy Gamma-Ray Flare of PKS 2155-304. *ApJL*, 664:L71–L74, August 2007.
- F. A. Aharonian. TeV gamma rays from BL Lac objects due to synchrotron radiation of extremely high energy protons. *New Astronomy*, 5:377–395, November 2000.
- F. A. Aharonian and A. M. Atoyan. Compton scattering of relativistic electrons in compact X-ray sources. *Ap&SS*, 79:321–336, October 1981.
- F. A. Aharonian, S. R. Kelner, and A. Y. Prosekin. Angular, spectral, and time distributions of highest energy protons and associated secondary gamma rays and neutrinos propagating through extragalactic magnetic and radiation fields. *Phys. Rev. D*, 82(4):043002, August 2010.
- M. L. Ahnen, S. Ansoldi, L. A. Antonelli, et al. First multi-wavelength campaign on the gamma-ray-loud active galaxy IC 310. *A&A*, 603:A25, July 2017.
- A. Albert, R. Alfaro, C. Alvarez, et al. Daily monitoring of TeV gamma-ray emission from Mrk 421, Mrk 501, and the Crab Nebula with HAWC. *ArXiv e-prints*, March 2017.
- J. Albert, E. Aliu, H. Anderhub, et al. Variable Very High Energy  $\gamma$ -Ray Emission from Markarian 501. *ApJ*, 669:862–883, November 2007.
- J. Aleksić, S. Ansoldi, L. A. Antonelli, et al. MAGIC gamma-ray and multi-frequency observations of flat spectrum radio quasar PKS 1510-089 in early 2012. *A&A*, 569:A46, September 2014a.
- J. Aleksić, S. Ansoldi, L. A. Antonelli, et al. Black hole lightning due to particle acceleration at sub-horizon scales. *Science*, 346:1080–1084, November 2014b.
- J. Aleksić, L. A. Antonelli, P. Antoranz, et al. Rapid and multiband variability of the TeV bright active nucleus of the galaxy IC 310. *A&A*, 563:A91, March 2014c.
- J. Aleksić, S. Ansoldi, L. A. Antonelli, et al. The 2009 multiwavelength campaign on Mrk 421: Variability and correlation studies. *A&A*, 576:A126, April 2015a.

- J. Aleksić, S. Ansoldi, L. A. Antonelli, et al. Multi-wavelength observations of Mrk 501 in 2008. *A&A*, 573:A50, January 2015b.
- J. C. Algaba, M. Nakamura, K. Asada, and S. S. Lee. Resolving the Geometry of the Innermost Relativistic Jets in Active Galactic Nuclei. *ApJ*, 834: 65, January 2017.
- R. Antonucci. Unified models for active galactic nuclei and quasars. *ARA&A*, 31:473–521, 1993.
- A. T. Araudo, V. Bosch-Ramon, and G. E. Romero. Gamma rays from cloud penetration at the base of AGN jets. *A&A*, 522:A97, November 2010.
- A. T. Araudo, V. Bosch-Ramon, and G. E. Romero. Gamma-ray emission from massive stars interacting with active galactic nuclei jets. *MNRAS*, 436: 3626–3639, December 2013.
- K. Asada and M. Nakamura. The Structure of the M87 Jet: A Transition from Parabolic to Conical Streamlines. *ApJL*, 745:L28, February 2012.
- K. Asada, M. Nakamura, A. Doi, H. Nagai, and M. Inoue. Discovery of Sub- to Superluminal Motions in the M87 Jet: An Implication of Acceleration from Sub-relativistic to Relativistic Speeds. *ApJL*, 781: L2, January 2014.
- K. Asano, F. Takahara, M. Kusunose, K. Toma, and J. Kakuwa. Time-dependent Models for Blazar Emission with the Second-order Fermi Acceleration. *ApJ*, 780:64, January 2014.
- A. M. Atoyan and C. D. Dermer. Neutral Beams from Blazar Jets. *ApJ*, 586:79–96, March 2003.
- W. I. Axford, E. Leer, and G. Skadron. The acceleration of cosmic rays by shock waves. *International Cosmic Ray Conference*, 11:132–137, 1977.
- W. Baade and R. Minkowski. Identification of the Radio Sources in Cassiopeia, Cygnus A, and Puppis A. *ApJ*, 119:206, January 1954.
- R. Bachiller. Bipolar Molecular Outflows from Young Stars and Protostars. *ARA&A*, 34:111–154, 1996.
- M. Baloković, D. Paneque, G. Madejski, et al. Multi-wavelength Study of Quiescent States of Mrk 421 with Unprecedented Hard X-Ray Coverage Provided by NuSTAR in 2013. *ApJ*, 819:156, March 2016.
- P. Banasiński and W. Bednarek. The Optically Thick Homogeneous SSC Model: Application to Radio Galaxy NGC 1275. In *International Journal of Modern Physics Conference Series*, volume 28 of *International Journal of Modern Physics Conference Series*, page 1460205, March 2014.
- P. Banasiński, W. Bednarek, and J. Sitarek. Orphan  $\gamma$ -ray flares from relativistic blobs encountering luminous stars. *MNRAS*, 463:L26–L30, November 2016.
- M. V. Barkov, F. A. Aharonian, and V. Bosch-Ramon. Gamma-ray Flares from Red Giant/Jet Interactions in Active Galactic Nuclei. *ApJ*, 724: 1517–1523, December 2010.
- M. V. Barkov, F. A. Aharonian, S. V. Bogovalov, S. R. Kelner, and D. Khangulyan. Rapid TeV Variability in Blazars as a Result of Jet-Star Interaction. *ApJ*, 749:119, April 2012.
- U. Barres de Almeida, F. Tavecchio, and N. Mankuzhiyil. Polarimetric tomography of blazar jets. *MNRAS*, 441:2885–2890, July 2014.
- A. J. Barth, L. C. Ho, and W. L. W. Sargent. The Black Hole Masses and Host Galaxies of BL Lacertae Objects. *ApJ*, 583:134–144, January 2003.
- J. H. Beall and W. Bednarek. On the Hadronic Beam Model for Gamma-Ray Production in Blazars. *ApJ*, 510:188–196, January 1999.
- V. Beckmann and C. Shrader. The AGN phenomenon: open issues. In *Proceedings of “An INTEGRAL view of the high-energy sky (the first 10 years)” - 9th INTEGRAL Workshop and celebration of the 10th anniversary of the launch (INTEGRAL 2012). 15-19 October 2012. Bibliothèque Nationale de France, Paris, France. Published online at jA href=“http://pos.sissa.it/cgi-bin/reader/conf.cgi?confid=176”&http://pos.sissa.it/cgi-bin/reader/conf.cgi?confid=176j/A&, id.69, page 69, 2012.*
- W. Bednarek. On the gamma-ray emission from 3C 279. *ApJL*, 402:L29–L32, January 1993.
- W. Bednarek. Gamma-rays from synchrotron pair cascades in blazars? *MNRAS*, 285:69–81, February 1997.
- W. Bednarek. On the application of the mirror model for gamma-ray flare in 3C 279. *A&A*, 336:123–129, August 1998.

- W. Bednarek and P. Banasiński. Non-thermal Radiation from Collisions of Compact Objects with Intermediate-scale Jets in Active Galaxies. *ApJ*, 807:168, July 2015.
- W. Bednarek and R. J. Protheroe. Gamma-rays from interactions of stars with active galactic nucleus jets. *MNRAS*, 287:L9–L13, May 1997a.
- W. Bednarek and R. J. Protheroe. Testing the homogeneous synchrotron self-Compton model for gamma-ray production in MRK 421. *MNRAS*, 292:646, December 1997b.
- W. Bednarek and R. J. Protheroe. The physical parameters of Markarian 501 during flaring activity. *MNRAS*, 310:577–584, December 1999a.
- W. Bednarek and R. J. Protheroe. Gamma-ray and neutrino flares produced by protons accelerated on an accretion disc surface in active galactic nuclei. *MNRAS*, 302:373–380, January 1999b.
- W. Bednarek, J. G. Kirk, and A. Mastichiadis. On the production of very high energy beamed gamma-rays in blazars. *A&A*, 307:L17, March 1996.
- J. Bednarz and M. Ostrowski. Energy Spectra of Cosmic Rays Accelerated at Ultrarelativistic Shock Waves. *Physical Review Letters*, 80:3911–3914, May 1998.
- M. C. Begelman, R. D. Blandford, and M. J. Rees. Theory of extragalactic radio sources. *Reviews of Modern Physics*, 56:255–351, April 1984.
- M. C. Begelman, A. C. Fabian, and M. J. Rees. Implications of very rapid TeV variability in blazars. *MNRAS*, 384:L19–L23, February 2008.
- A. R. Bell. The acceleration of cosmic rays in shock fronts. I. *MNRAS*, 182:147–156, January 1978.
- M. Bernardi, M. V. Alonso, L. N. da Costa, et al. Redshift-Distance Survey of Early-Type Galaxies. I. The ENEARc Cluster Sample. *AJ*, 123:2990–3017, June 2002.
- D. Bettoni, R. Falomo, G. Fasano, and F. Govoni. The black hole mass of low redshift radiogalaxies. *A&A*, 399:869–878, March 2003.
- J. A. Biretta, W. B. Sparks, and F. Macchetto. Hubble Space Telescope Observations of Superluminal Motion in the M87 Jet. *ApJ*, 520:621–626, August 1999.
- R. D. Blandford. Accretion disc electrodynamics - A model for double radio sources. *MNRAS*, 176:465–481, September 1976.
- R. D. Blandford and A. Königl. Relativistic jets as compact radio sources. *ApJ*, 232:34–48, August 1979.
- R. D. Blandford and J. P. Ostriker. Particle acceleration by astrophysical shocks. *ApJL*, 221:L29–L32, April 1978.
- R. D. Blandford and D. G. Payne. Hydromagnetic flows from accretion discs and the production of radio jets. *MNRAS*, 199:883–903, June 1982.
- R. D. Blandford and R. L. Znajek. Electromagnetic extraction of energy from Kerr black holes. *MNRAS*, 179:433–456, May 1977.
- M. Błażejowski, M. Sikora, R. Moderski, and G. M. Madejski. Comptonization of Infrared Radiation from Hot Dust by Relativistic Jets in Quasars. *ApJ*, 545:107–116, December 2000.
- G. R. Blumenthal and R. J. Gould. Bremsstrahlung, Synchrotron Radiation, and Compton Scattering of High-Energy Electrons Traversing Dilute Gases. *Reviews of Modern Physics*, 42:237–271, 1970.
- B. Boccardi, T. P. Krichbaum, U. Bach, M. Bremer, and J. A. Zensus. First 3 mm-VLBI imaging of the two-sided jet in Cygnus A. Zooming into the launching region. *A&A*, 588:L9, April 2016a.
- B. Boccardi, T. P. Krichbaum, U. Bach, et al. The stratified two-sided jet of JASTROBJ<sub>2</sub>Cygnus A<sub>1</sub>/ASTROBJ<sub>2</sub>. Acceleration and collimation. *A&A*, 585:A33, January 2016b.
- M. Boettcher and R. Schlickeiser. The pair production spectrum from photon-photon annihilation. *A&A*, 325:866–870, September 1997.
- M. Boettcher, D. E. Harris, and H. Krawczynski. *Relativistic Jets from Active Galactic Nuclei*. January 2012.
- J. G. Bolton, G. J. Stanley, and O. B. Slee. Positions of Three Discrete Sources of Galactic Radio-Frequency Radiation. *Nature*, 164:101–102, July 1949.
- V. Bosch-Ramon, M. Perucho, and M. V. Barkov. Clouds and red giants interacting with the base of AGN jets. *A&A*, 539:A69, March 2012.

- M. Böttcher. A Hadronic Synchrotron Mirror Model for the “Orphan” TeV Flare in 1ES 1959+650. *ApJ*, 621:176–180, March 2005.
- T. Boutelier, G. Henri, and P.-O. Petrucci. An inhomogeneous jet model for the rapid variability of TeV blazars. *MNRAS*, 390:L73–L77, October 2008.
- A. H. Bridle and R. A. Perley. Extragalactic Radio Jets. *ARA&A*, 22:319–358, 1984.
- A. Celotti and G. Ghisellini. The power of blazar jets. *MNRAS*, 385:283–300, March 2008.
- J. S. Chang and G. Cooper. A Practical Difference Scheme for Fokker-Planck Equations. *Journal of Computational Physics*, 6:1–16, August 1970.
- A. Chhotray, F. Nappo, G. Ghisellini, et al. On radiative acceleration in spine-sheath structured blazar jets. *ArXiv e-prints*, October 2016.
- M. Chiaberge and G. Ghisellini. Rapid variability in the synchrotron self-Compton model for blazars. *MNRAS*, 306:551–560, July 1999.
- M. Chiaberge, A. Celotti, A. Capetti, and G. Ghisellini. Does the unification of BL Lac and FR I radio galaxies require jet velocity structures? *A&A*, 358:104–112, June 2000.
- E. Clausen-Brown, T. Savolainen, A. B. Pushkarev, Y. Y. Kovalev, and J. A. Zensus. Causal connection in parsec-scale relativistic jets: results from the MOJAVE VLBI survey. *A&A*, 558:A144, October 2013.
- M. H. Cohen and A. C. S. Readhead. Misalignment in the radio jets of NGC 6251. *ApJL*, 233:L101–L104, November 1979.
- M. H. Cohen, M. L. Lister, D. C. Homan, et al. Relativistic Beaming and the Intrinsic Properties of Extragalactic Radio Jets. *ApJ*, 658:232–244, March 2007.
- J. J. Condon. Radio emission from normal galaxies. *ARA&A*, 30:575–611, 1992.
- L. Costamante, G. Bonnoli, F. Tavecchio, et al. The NuSTAR view on hard-TeV BL Lacs. *MNRAS*, 477:4257–4268, July 2018.
- F. D’Ammando, M. Orienti, F. Tavecchio, et al. Unveiling the nature of the  $\gamma$ -ray emitting active galactic nucleus PKS 0521-36. *MNRAS*, 450:3975–3990, July 2015.
- A. Dar and A. Laor. Hadronic Production of TeV Gamma-Ray Flares from Blazars. *ApJL*, 478:L5–L8, March 1997.
- C. D. Dermer and B. Giebels. Active galactic nuclei at gamma-ray energies. *Comptes Rendus Physique*, 17:594–616, June 2016.
- C. D. Dermer and R. Schlickeiser. Model for the High-Energy Emission from Blazars. *ApJ*, 416:458, October 1993.
- A. Domínguez, J. D. Finke, F. Prada, et al. Detection of the Cosmic  $\gamma$ -Ray Horizon from Multiwavelength Observations of Blazars. *ApJ*, 770:77, June 2013.
- E. Dwek and F. Krennrich. The extragalactic background light and the gamma-ray opacity of the universe. *Astroparticle Physics*, 43:112–133, March 2013.
- D. Eisenacher Glawion, J. Sitarek, K. Mannheim, et al. Black Hole Lightning from the Peculiar Gamma-Ray Loud Active Galactic Nucleus IC 310. *ArXiv e-prints*, August 2015.
- G. Fabbiano. X rays from normal galaxies. *ARA&A*, 27:87–138, 1989.
- B. L. Fanaroff and J. M. Riley. The morphology of extragalactic radio sources of high and low luminosity. *MNRAS*, 167:31P–36P, May 1974.
- E. A. Fath. The spectra of some spiral nebulae and globular star clusters. *Lick Observatory Bulletin*, 5:71–77, 1909.
- E. Fermi. On the Origin of the Cosmic Radiation. *Physical Review*, 75:1169–1174, April 1949.
- L. Ferrarese and H. Ford. Supermassive Black Holes in Galactic Nuclei: Past, Present and Future Research. *Space Science Reviews*, 116:523–624, February 2005.
- L. Ferrarese and D. Merritt. A Fundamental Relation between Supermassive Black Holes and Their Host Galaxies. *ApJL*, 539:L9–L12, August 2000.
- G. Fossati, L. Maraschi, A. Celotti, A. Comastri, and G. Ghisellini. A unifying view of the spectral energy distributions of blazars. *MNRAS*, 299:433–448, September 1998.

- P. J. Francis, P. C. Hewett, C. B. Foltz, et al. A high signal-to-noise ratio composite quasar spectrum. *ApJ*, 373:465–470, June 1991.
- J. Frank, A. King, and D. J. Raine. *Accretion Power in Astrophysics: Third Edition*. January 2002.
- Y. Fukazawa, J. Finke, Ł. Stawarz, et al. Suzaku Observations of  $\gamma$ -Ray Bright Radio Galaxies: Origin of the X-Ray Emission and Broadband Modeling. *ApJ*, 798:74, January 2015.
- K. Gebhardt and J. Thomas. The Black Hole Mass, Stellar Mass-to-Light Ratio, and Dark Halo in M87. *ApJ*, 700:1690–1701, August 2009.
- K. Gebhardt, R. Bender, G. Bower, et al. A Relationship between Nuclear Black Hole Mass and Galaxy Velocity Dispersion. *ApJL*, 539:L13–L16, August 2000.
- G. Ghisellini, editor. *Radiative Processes in High Energy Astrophysics*, volume 873 of *Lecture Notes in Physics*, Berlin Springer Verlag, 2013.
- G. Ghisellini. The Blazar Sequence 2.0. *Galaxies*, 4: 36, September 2016.
- G. Ghisellini and P. Madau. On the origin of the gamma-ray emission in blazars. *MNRAS*, 280:67–76, May 1996.
- G. Ghisellini and R. Svensson. The synchrotron and cyclo-synchrotron absorption cross-section. *MNRAS*, 252:313–318, October 1991.
- G. Ghisellini, L. Maraschi, and A. Treves. Inhomogeneous synchrotron-self-Compton models and the problem of relativistic beaming of BL Lac objects. *A&A*, 146:204–212, May 1985.
- G. Ghisellini, F. Tavecchio, and M. Chiaberge. Structured jets in TeV BL Lac objects and radiogalaxies. Implications for the observed properties. *A&A*, 432:401–410, March 2005.
- G. Ghisellini, F. Tavecchio, L. Foschini, et al. General physical properties of bright Fermi blazars. *MNRAS*, 402:497–518, February 2010.
- G. Ghisellini, C. Righi, L. Costamante, and F. Tavecchio. The Fermi blazar sequence. *MNRAS*, 469: 255–266, July 2017.
- D. Giannios, D. A. Uzdensky, and M. C. Begelman. Fast TeV variability in blazars: jets in a jet. *MNRAS*, 395:L29–L33, May 2009.
- R. C. Gilmore, R. S. Somerville, J. R. Primack, and A. Domínguez. Semi-analytic modelling of the extragalactic background light and consequences for extragalactic gamma-ray spectra. *MNRAS*, 422: 3189–3207, June 2012.
- P. Giommi, E. Massaro, L. Chiappetti, et al. Synchrotron and inverse Compton variability in the BL Lacertae object S5 0716+714. *A&A*, 351:59–64, November 1999.
- Robert J. Gould and Gérard P. Schréder. Pair production in photon-photon collisions. *Phys. Rev.*, 155:1404–1407, Mar 1967. URL <https://link.aps.org/doi/10.1103/PhysRev.155.1404>.
- J. L. Greenstein and T. A. Matthews. Redshift of the Radio Source 3C 48. *AJ*, 68:279, 1963.
- J. L. Greenstein and M. Schmidt. The Quasi-Stellar Radio Sources 3C 48 and 3C 273. *ApJ*, 140:1, July 1964.
- F. Guo, H. Li, W. Daughton, and Y.-H. Liu. Formation of Hard Power Laws in the Energetic Particle Spectra Resulting from Relativistic Magnetic Reconnection. *Physical Review Letters*, 113(15): 155005, October 2014.
- K. Hada, M. Kino, A. Doi, et al. The Innermost Collimation Structure of the M87 Jet Down to  $\sim 10$  Schwarzschild Radii. *ApJ*, 775:70, September 2013.
- R. C. Hartman, D. L. Bertsch, C. E. Fichtel, et al. Detection of high-energy gamma radiation from quasar 3C 279 by the EGRET telescope on the Compton Gamma Ray Observatory. *ApJL*, 385: L1–L4, January 1992.
- M. Hayashida, K. Nalewajko, G. M. Madejski, et al. Rapid Variability of Blazar 3C 279 during Flaring States in 2013-2014 with Joint Fermi-LAT, NuSTAR, Swift, and Ground-Based Multiwavelength Observations. *ApJ*, 807:79, July 2015.
- G. Henri and G. Pelletier. Relativistic electron-positron beam formation in the framework of the two-flow model for active galactic nuclei. *ApJL*, 383:L7–L10, December 1991.
- O. Hervet, C. Boisson, and H. Sol. Linking radio and gamma-ray emission in Ap Librae. *A&A*, 578:A69, June 2015.

- K. Hirotani, H.-Y. Pu, L. C.-C. Lin, et al. Lepton Acceleration in the Vicinity of the Event Horizon: High-energy and Very-high-energy Emissions from Rotating Black Holes with Various Masses. *ApJ*, 833:142, December 2016.
- M. Janiak, M. Sikora, and R. Moderski. Application of the spine-layer jet radiation model to outbursts in the broad-line radio galaxy 3C 120. *MNRAS*, 458:2360–2370, May 2016.
- S. G. Jorstad, A. P. Marscher, D. A. Morozova, et al. Kinematics of Parsec-scale Jets of Gamma-Ray Blazars at 43 GHz within the VLBA-BU-BLAZAR Program. *ApJ*, 846:98, September 2017.
- M. Kadler, D. Eisenacher, E. Ros, et al. The blazar-like radio structure of the TeV source IC 310. *A&A*, 538:L1, February 2012.
- N. S. Kardashev. Nonstationarity of Spectra of Young Sources of Nonthermal Radio Emission. *Soviet Astronomy*, 6:317, December 1962.
- J. Kataoka and Ł. Stawarz. Inverse Compton X-Ray Emission from TeV Blazar Mrk 421 During a Historical Low-flux State Observed with NuSTAR. *ApJ*, 827:55, August 2016.
- J. Kataoka, Ł. Stawarz, F. Aharonian, et al. The X-Ray Jet in Centaurus A: Clues to the Jet Structure and Particle Acceleration. *ApJ*, 641:158–168, April 2006.
- K. Katarzyński, H. Sol, and A. Kus. The multifrequency emission of Mrk 501. From radio to TeV gamma-rays. *A&A*, 367:809–825, March 2001.
- K. Katarzyński, G. Ghisellini, A. Mastichiadis, F. Tavecchio, and L. Maraschi. Stochastic particle acceleration and synchrotron self-Compton radiation in TeV blazars. *A&A*, 453:47–56, July 2006.
- W. C. Keel. Spectroscopic evidence for activity in the nuclei of normal spiral galaxies. *ApJ*, 269:466–486, June 1983.
- K. I. Kellermann and I. I. K. Pauliny-Toth. The Spectra of Opaque Radio Sources. *ApJL*, 155:L71, February 1969.
- K. I. Kellermann, R. Sramek, M. Schmidt, D. B. Shaffer, and R. Green. VLA observations of objects in the Palomar Bright Quasar Survey. *AJ*, 98:1195–1207, October 1989.
- R. C. Kennicutt, Jr. A spectrophotometric atlas of galaxies. *ApJS*, 79:255–284, April 1992.
- M. Kino, F. Takahara, and M. Kusunose. Energetics of TeV Blazars and Physical Constraints on Their Emission Regions. *ApJ*, 564:97–107, January 2002.
- J. G. Kirk and P. Schneider. On the acceleration of charged particles at relativistic shock fronts. *ApJ*, 315:425–433, April 1987.
- S. S. Komissarov. Direct numerical simulations of the Blandford-Znajek effect. *MNRAS*, 326:L41–L44, September 2001.
- J. Kormendy and D. Richstone. Inward Bound—The Search For Supermassive Black Holes In Galactic Nuclei. *ARA&A*, 33:581, 1995.
- H. Krawczynski, S. B. Hughes, D. Horan, et al. Multiwavelength Observations of Strong Flares from the TeV Blazar 1ES 1959+650. *ApJ*, 601:151–164, January 2004.
- T. P. Krichbaum, W. Alef, A. Witzel, et al. VLBI observations of Cygnus A with sub-milliarcsecond resolution. *A&A*, 329:873–894, January 1998.
- G. F. Krymskii. A regular mechanism for the acceleration of charged particles on the front of a shock wave. *Akademiia Nauk SSSR Doklady*, 234:1306–1308, June 1977.
- P. Kumar and B. Zhang. The physics of gamma-ray bursts and relativistic jets. *Physics Reports*, 561:1–109, February 2015.
- A. Laor. On Quasar Masses and Quasar Host Galaxies. *ApJL*, 505:L83–L86, October 1998.
- C. R. Lawrence, J. R. Zucker, A. C. S. Readhead, et al. Optical Spectra of a Complete Sample of Radio Sources. I. The Spectra. *ApJS*, 107:541, December 1996.
- R. Lico, M. Giroletti, M. Orienti, et al. VLBA monitoring of Mrk 421 at 15 GHz and 24 GHz during 2011. *A&A*, 545:A117, September 2012.
- M. L. Lister, M. H. Cohen, D. C. Homan, et al. MOJAVE: Monitoring of Jets in Active Galactic Nuclei with VLBA Experiments. VI. Kinematics Analysis of a Complete Sample of Blazar Jets. *AJ*, 138:1874–1892, December 2009.

- M. L. Lister, M. F. Aller, H. D. Aller, et al. MOJAVE. X. Parsec-scale Jet Orientation Variations and Superluminal Motion in Active Galactic Nuclei. *AJ*, 146:120, November 2013.
- M. S. Longair. *High Energy Astrophysics*. February 2011.
- R. V. E. Lovelace. Dynamo model of double radio sources. *Nature*, 262:649–652, August 1976.
- N. R. MacDonald, A. P. Marscher, S. G. Jorstad, and M. Joshi. Through the Ring of Fire: Gamma-Ray Variability in Blazars by a Moving Plasmoid Passing a Local Source of Seed Photons. *ApJ*, 804:111, May 2015.
- J. Machalski, D. Koziel-Wierzbowska, M. Jamroz, and D. J. Saikia. J1420-0545: The Radio Galaxy Larger than 3C 236. *ApJ*, 679:149-155, May 2008.
- G. M. Madejski, K. Nalewajko, K. K. Madsen, et al. First NuSTAR Observations of the BL Lac-type Blazar PKS 2155-304: Constraints on the Jet Content and Distribution of Radiating Particles. *ApJ*, 831:142, November 2016.
- J. Malzac. Internal shocks at the origin of the flat spectral energy distribution of compact jets. *MNRAS*, 429:L20–L24, February 2013.
- K. Mannheim. The proton blazar. *A&A*, 269:67–76, March 1993.
- K. Mannheim and P. L. Biermann. Gamma-ray flaring of 3C 279 - A proton-initiated cascade in the jet? *A&A*, 253:L21–L24, January 1992.
- K. Mannheim, P. L. Biermann, and W. M. Kruells. A novel mechanism for nonthermal X-ray emission. *A&A*, 251:723–731, November 1991.
- L. Maraschi, G. Ghisellini, and A. Celotti. A jet model for the gamma-ray emitting blazar 3C 279. *ApJL*, 397:L5–L9, September 1992.
- F. Mertens, A. P. Lobanov, R. C. Walker, and P. E. Hardee. Kinematics of the jet in M 87 on scales of 100-1000 Schwarzschild radii. *A&A*, 595:A54, October 2016.
- I. F. Mirabel and L. F. Rodríguez. Sources of Relativistic Jets in the Galaxy. *ARA&A*, 37:409–443, 1999.
- R. Moderski, M. Sikora, and M. Błażejowski. Numerical simulations of radiation from blazar jets. *A&A*, 406:855–865, August 2003.
- R. Moderski, M. Sikora, P. S. Coppi, and F. Aharonian. Klein-Nishina effects in the spectra of non-thermal sources immersed in external radiation fields. *MNRAS*, 363:954–966, November 2005.
- A. Mücke and R. J. Protheroe. A proton synchrotron blazar model for flaring in Markarian 501. *Astroparticle Physics*, 15:121–136, March 2001.
- H. Nagai, T. Haga, G. Giovannini, et al. Limb-brightened Jet of 3C 84 Revealed by the 43 GHz Very-Long-Baseline-Array Observation. *ApJ*, 785: 53, April 2014.
- K. Nalewajko and M. Sikora. A structure and energy dissipation efficiency of relativistic reconfinement shocks. *MNRAS*, 392:1205–1210, January 2009.
- K. Nalewajko, D. Giannios, M. C. Begelman, D. A. Uzdensky, and M. Sikora. Radiative properties of reconnection-powered minijets in blazars. *MNRAS*, 413:333–346, May 2011.
- R. Narayan and J. E. McClintock. Advection-dominated accretion and the black hole event horizon. *NAR*, 51:733–751, May 2008.
- A. Neronov and F. A. Aharonian. Production of TeV Gamma Radiation in the Vicinity of the Supermassive Black Hole in the Giant Radio Galaxy M87. *ApJ*, 671:85–96, December 2007.
- A. Neronov and I. Vovk. Evidence for Strong Extragalactic Magnetic Fields from Fermi Observations of TeV Blazars. *Science*, 328:73, April 2010.
- S. P. O’Sullivan and D. C. Gabuzda. Magnetic field strength and spectral distribution of six parsec-scale active galactic nuclei jets. *MNRAS*, 400:26–42, November 2009.
- F. N. Owen, C. P. O’Dea, and W. C. Keel. Long-slit spectroscopy of 3C 31, 3C 75, 3C 465, NGC 1265, and Cygnus A. *ApJ*, 352:44–54, March 1990.
- R. Penrose. Gravitational Collapse: the Role of General Relativity. *Nuovo Cimento Rivista Serie*, 1, 1969.
- R. A. Perley, A. H. Bridle, and A. G. Willis. High-resolution VLA observations of the radio jet in NGC 6251. *ApJS*, 54:291–334, February 1984.

- B. M. Peterson. Reverberation mapping of active galactic nuclei. *PASP*, 105:247–268, March 1993.
- B. M. Peterson. *An Introduction to Active Galactic Nuclei*. February 1997.
- B. Piner and P. Edwards. Parsec-Scale Structure and Kinematics of Faint TeV HBLs. *Galaxies*, 4:44, October 2016.
- B. G. Piner and P. G. Edwards. Multi-Epoch VLBA Imaging of Twenty New TeV Blazars: Apparent Jet Speeds. *ArXiv e-prints*, January 2018.
- B. G. Piner, N. Pant, P. G. Edwards, and K. Wiik. Significant Limb-Brightening in the Inner Parsec of Markarian 501. *ApJL*, 690:L31–L34, January 2009.
- W. J. Potter and G. Cotter. Synchrotron and inverse-Compton emission from blazar jets - I. A uniform conical jet model. *MNRAS*, 423:756–765, June 2012.
- E. Prandini. Highlights from TeV Extragalactic Sources. *ArXiv e-prints*, June 2017.
- R. J. Protheroe. High Energy Neutrinos from Blazars. In D. T. Wickramasinghe, G. V. Bicknell, and L. Ferrario, editors, *IAU Colloq. 163: Accretion Phenomena and Related Outflows*, volume 121 of *Astronomical Society of the Pacific Conference Series*, page 585, 1997.
- M. Punch, C. W. Akerlof, M. F. Cawley, et al. Detection of TeV photons from the active galaxy Markarian 421. *Nature*, 358:477, August 1992.
- A. B. Pushkarev, Y. Y. Kovalev, M. L. Lister, and T. Savolainen. Jet opening angles and gamma-ray brightness of AGN. *A&A*, 507:L33–L36, November 2009.
- A. C. S. Readhead. Equipartition brightness temperature and the inverse Compton catastrophe. *ApJ*, 426:51–59, May 1994.
- M. J. Rees. The M87 jet - Internal shocks in a plasma beam. *MNRAS*, 184:61P–65P, September 1978.
- F. M. Rieger and F. Aharonian. Probing the Central Black Hole in M87 with Gamma-Rays. *Modern Physics Letters A*, 27:1230030, September 2012.
- F. M. Rieger and P. Duffy. Shear Acceleration in Relativistic Astrophysical Jets. *ApJ*, 617:155–161, December 2004.
- G. B. Rybicki and A. P. Lightman. *Radiative Processes in Astrophysics*. June 1986.
- S. Saito, Ł. Stawarz, Y. T. Tanaka, et al. Very Rapid High-amplitude Gamma-Ray Variability in Luminous Blazar PKS 1510-089 Studied with Fermi-LAT. *ApJL*, 766:L11, March 2013.
- R. H. Sanders. The reconfinement of jets. *ApJ*, 266:73–81, March 1983.
- R. Schlickeiser. *Cosmic Ray Astrophysics*. 2002.
- R. Schlickeiser. Non-linear synchrotron self-Compton cooling of relativistic electrons. *MNRAS*, 398:1483–1494, September 2009.
- M. Schmidt. 3C 273 : A Star-Like Object with Large Red-Shift. *Nature*, 197:1040, March 1963.
- P. Schneider. *Extragalactic Astronomy and Cosmology*. 2006.
- N. I. Shakura and R. A. Sunyaev. Black holes in binary systems. Observational appearance. *A&A*, 24:337–355, 1973.
- G. A. Shields. A Brief History of Active Galactic Nuclei. *PASP*, 111:661–678, June 1999.
- A. Shukla, V. R. Chitnis, B. B. Singh, et al. Multi-frequency, Multi-epoch Study of Mrk 501: Hints for a Two-component Nature of the Emission. *ApJ*, 798:2, January 2015.
- M. Sikora. Hadronic jet models today. In G. E. Romero, R. A. Sunyaev, and T. Belloni, editors, *Jets at All Scales*, volume 275 of *IAU Symposium*, pages 59–67, February 2011.
- M. Sikora, M. C. Begelman, and M. J. Rees. Comptonization of diffuse ambient radiation by a relativistic jet: The source of gamma rays from blazars? *ApJ*, 421:153–162, January 1994.
- M. Sikora, M. C. Begelman, G. M. Madejski, and J.-P. Lasota. Are Quasar Jets Dominated by Poynting Flux? *ApJ*, 625:72–77, May 2005.
- M. Sikora, M. Janiak, K. Nalewajko, G. M. Madejski, and R. Moderski. On the Origin of X-Ray Spectra in Luminous Blazars. *ApJ*, 779:68, December 2013.
- M. Sikora, M. Rutkowski, and M. C. Begelman. A spine-sheath model for strong-line blazars. *MNRAS*, 457:1352–1358, April 2016.

- L. Sironi and A. Spitkovsky. Relativistic Reconnection: An Efficient Source of Non-thermal Particles. *ApJL*, 783:L21, March 2014.
- L. Sironi, M. Petropoulou, and D. Giannios. Relativistic jets shine through shocks or magnetic reconnection? *MNRAS*, 450:183–191, June 2015.
- E. Sobacchi, M. C. Sormani, and A. Stamerra. A model for periodic blazars. *ArXiv e-prints*, October 2016.
- H. Sol, G. Pelletier, and E. Asseo. Two-flow model for extragalactic radio jets. *MNRAS*, 237:411–429, March 1989.
- M. Spada, D. Lazzati, G. Ghisellini, and A. Celotti. Internal shocks in the jets of blazars. *Mem. Soc. Astron. Italiana*, 72:157–159, 2001.
- Ł. Stawarz and M. Ostrowski. Radiation from the Relativistic Jet: A Role of the Shear Boundary Layer. *ApJ*, 578:763–774, October 2002.
- Ł. Stawarz and V. Petrosian. On the Momentum Diffusion of Radiating Ultrarelativistic Electrons in a Turbulent Magnetic Field. *ApJ*, 681:1725–1744, July 2008.
- J. W. Sulentic, P. Marziani, and D. Dultzin-Hacyan. Phenomenology of Broad Emission Lines in Active Galactic Nuclei. *ARA&A*, 38:521–571, 2000.
- B. N. Swanenburg, K. Bennett, G. F. Bignami, et al. COS B observation of high-energy gamma radiation from 3C273. *Nature*, 275:298, September 1978.
- C. Tadhunter. An introduction to active galactic nuclei: Classification and unification. *NAR*, 52:227–239, August 2008.
- G. Tagliaferri, G. Ghisellini, P. Giommi, et al. The concave X-ray spectrum of the blazar ON 231: the signature of intermediate BL Lacertae objects. *A&A*, 354:431–438, February 2000.
- F. Tavecchio and G. Ghisellini. Spine-sheath layer radiative interplay in subparsec-scale jets and the TeV emission from M87. *MNRAS*, 385:L98–L102, March 2008.
- F. Tavecchio and G. Ghisellini. On the spine-layer scenario for the very high-energy emission of NGC 1275. *MNRAS*, 443:1224–1230, September 2014.
- F. Tavecchio, L. Maraschi, and G. Ghisellini. Constraints on the Physical Parameters of TeV Blazars. *ApJ*, 509:608–619, December 1998.
- F. Tavecchio, J. Becerra-Gonzalez, G. Ghisellini, et al. On the origin of the  $\gamma$ -ray emission from the flaring blazar PKS 1222+216. *A&A*, 534:A86, October 2011.
- A. Tramacere, E. Massaro, and A. M. Taylor. Stochastic Acceleration and the Evolution of Spectral Distributions in Synchro-Self-Compton Sources: A Self-consistent Modeling of Blazars’ Flares. *ApJ*, 739:66, October 2011.
- M.-H. Ulrich, L. Maraschi, and C. M. Urry. Variability of Active Galactic Nuclei. *ARA&A*, 35:445–502, 1997.
- C. M. Urry and P. Padovani. Unified Schemes for Radio-Loud Active Galactic Nuclei. *PASP*, 107:803, September 1995.
- N. Vlahakis and A. Königl. Magnetic Driving of Relativistic Outflows in Active Galactic Nuclei. I. Interpretation of Parsec-Scale Accelerations. *ApJ*, 605:656–661, April 2004.
- S. J. Wagner and A. Witzel. Intraday Variability In Quasars and BL Lac Objects. *ARA&A*, 33:163–198, 1995.
- A. G. Willis, R. G. Strom, R. A. Perley, and A. H. Bridle. Recent WSRT and VLA observations of the jet radio galaxy NGC 6251. In D. S. Heeschen and C. M. Wade, editors, *Extragalactic Radio Sources*, volume 97 of *IAU Symposium*, pages 141–144, 1982.
- L. Woltjer. Emission Nuclei in Galaxies. *ApJ*, 130:38, July 1959.
- X.-B. Wu, F. K. Liu, and T. Z. Zhang. Supermassive black hole masses of AGNs with elliptical hosts. *A&A*, 389:742–751, July 2002.
- S. Wykes, M. J. Hardcastle, A. I. Karakas, and J. S. Vink. Internal entrainment and the origin of jet-related broad-band emission in Centaurus A. *MNRAS*, 447:1001–1013, February 2015.
- A. A. Zdziarski, Ł. Stawarz, P. Pjanka, and M. Sikora. Jet models for black hole binaries in the hard spectral state. *MNRAS*, 440:2238–2254, May 2014.